Nonlinear analysis of thermoacoustic modes in axisymmetric annular combustors

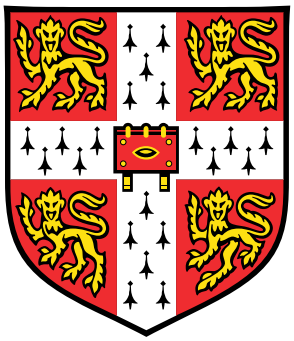

Giulio Ghirardo

University of Cambridge

This dissertation is submitted for the degree of
Doctor of Philosophy

Downing College February 2016

To my dear annular combustors. Though degenerate, you have proven rather interesting. Keep spinning but stand by me.

Declaration

I hereby declare that except where specific reference is made to the work of others, the contents of this dissertation are original and have not been submitted in whole or in part for consideration for any other degree or qualification in this, or any other university. This dissertation is my own work and contains nothing which is the outcome of work done in collaboration with others, except as specified in the text. This dissertation contains fewer than 65,000 words including appendices, bibliography, footnotes, tables and equations and has fewer than 150 figures.

Giulio Ghirardo
February 2016

Acknowledgements

I thank my supervisor Matthew Juniper for his valuable support and for giving me carte blanche on my PhD topic. I thank Nicholas Worth for being always available for discussions. My colleagues and ex-colleagues, Outi, Larry, Iain, Ubaid, Nick, Vik, Simon, Luca, Karthik, Chris, Alessandro have been great mates, not only in the office but also in life outside the office. An environment of good researchers and friends was key to foster positive energy and to orient my research in promising directions. I thank Lorenzo for the great times on the river, and Vik, my best flatmate ever. I thank Jonas Moeck for the three months spent at TU Berlin, and all the colleagues there: there was a great deal of awesomeness in pretty much every aspect of my stay. I thank Stefania for always being available as call centre when her phone was not on silent, and for finally joining me in Cambridge just in time to see me leave. I owe you there.

It was a wonderful ride.

Abstract

Thermoacoustic oscillations in annular combustors are often of azimuthal type, with two distinct thermoacoustic modes sharing the same frequency of oscillation. The two modes interact because each flame responds to the sum of the two modes and acts as a source term for both modes. In the nonlinear regime the system converge to a limit-cycle solution, which is an acoustic wave that is either spinning around the annulus, or a standing wave with pressure and velocity nodes fixed in space. This thesis answers some questions regarding these two types of solutions, and provides tools to analyse azimuthal modes.

A flame in the annular combustion chamber is subject to an axial acoustic field through the burner, and a transverse acoustic field sweeping it sideways. We show that the effect of this transverse acoustic field on the flame response can make the system prefer standing solutions instead of spinning solutions.

We present a tool to map a flame response from the frequency domain, where it is often described, to the time domain, where it is needed to discuss azimuthal instabilities.

We then carry out a weakly nonlinear analysis of the system taking into account the number of equispaced identical burners, the level of linear acoustic damping, the geometry and the nonlinear flame response to axial forcing. This leads to a low-order model of azimuthal instabilities that is ready to be used for the purpose of system identification. We provide conditions for the existence and stability of standing and spinning waves and the orientation and amplitudes of these solutions, and then discuss their physical interpretation.

We finally apply two mathematical methods, the method of averaging and the method of multiple scales, to predict the solutions of the system. This allows a validation of the methods, of which the first is used extensively in the rest of the manuscript, and a study of the effect of the delay between acoustic forcing and flame response, both in the linear and nonlinear regime.

Table of contents

Chapter 1

Introduction

Thermoacoustics studies the interaction of an acoustic field with a fluctuating heat release source. The acoustic field can respond to this fluctuating source, and excite it in turn. This can lead an initial perturbation to grow or decay in time in the closed loop formed by the fluctuating heat release and the acoustic field.

We focus on problems where the heat release is the result of the combustion of fuel and air, and the application are gas turbines, used for example to power airplanes or electric power plants. Thermoacoustic oscillations are undesired in this context, because they can lead to damage and a reduction of the operating window (Lieuwen and Yang, 2005). In many cases the combustion takes place in combustion chambers of annular shape. These chambers have typically a certain number of burners equispaced around the annulus, so that they exhibit a discrete rotational symmetry. This study regards combustion chambers that exhibit either this type of symmetry, or a full rotational symmetry, which is respected if the number of burners is so large that the flames can be a treated as a homogeneous response along the annulus. These combustion chambers present in general thermoacoustic modes that are axial, radial, or azimuthal, i.e. not homogeneous with respect to the azimuthal direction. Because of the quite large radial-to-axial aspect ratio of these combustion chambers, it often occurs that the frequencies of azimuthal modes are lower than those of axial modes, and are excited in industrial gas turbines (Seume et al. (1998), Lepers et al. (2005)) because they occur in a range of frequencies where the flames have a non-negligible response. Under the assumption of full rotational symmetry these azimuthal modes occur in degenerate pairs, i.e. share the same eigenfrequency[1]. For example, a cylindrical duct and an annular duct both present couples of azimuthal acoustic modes that are degenerate

[1] under the assumption of discrete rotational symmetry most azimuthal modes occur in degenerate pairs

(Munjal, 1987). The degeneracy of these azimuthal modes complicates the analysis of the system in the nonlinear regime: both modes of each pair take part in the oscillation, and interact between them through the combustion process. Depending on the phase difference between their oscillations, each pair can be observed as a travelling wave in either the clockwise or anti-clockwise direction in the annulus, or as a standing wave, with the nodal line of the pressure nodes fixed in time on a certain diameter of the annulus. We use the nomenclature of Crocco (1969), and refer to the two types as spinning and standing waves respectively.

Additionally, because azimuthal modes are not uniform in the azimuthal direction, the burners and the flames are exposed to pressure gradients that are not only axial, but also azimuthal, i.e. transversal to the direction of the mean flow. Chapter §2 discusses how the dynamics of the pairs of azimuthal modes change if the response of the flames is affected by the azimuthal component of the acoustic excitation. Chapter §2 shows how other studies on transverse forcing of flames are important in the study of azimuthal instabilities.

Evesque et al. (2003), Pankiewitz and Sattelmayer (2003), Schuermans et al. (2006), Stow and Dowling (2009) and Noiray et al. (2011) study low-order time domain simulations of annular chambers, and show that the system in their cases converge to a spinning solution. Each of these studies choose a different analytical expression for the nonlinear flame response, in the time-domain. However the flame response is more often available in terms of a describing function. Chapter §3 shows how to make use of a describing function in time domain simulations, to accurately predict the amplitude of oscillation and the type spinning/standing of the solution.

All previous theoretical studies fix a certain nonlinear flame response and show if standing and/or spinning modes are stable. Instead, in Chapter §4 we maintain a generic flame response, and discuss the conditions on such flame response that make standing and/or spinning solutions stable.

Finally, we carry out in Chapter §5 the analysis of the effect of the time-delay between acoustic excitation and flame response in the nonlinear regime. The chapter discusses two mathematical methods to study thermoacoustic oscillations as weakly nonlinear. It also presents the equation for the time evolution of not just the amplitudes of oscillation, but also of the frequency of oscillation.

Each chapter is independent of the others and introduces the motivations for the work. Chapter §2 was published as Ghirardo and Juniper (2013). Chapter §3 was published as Ghirardo et al. (2015a). Chapter §4 was partially published as Ghirardo

et al. (2015b), but it goes into greater detail and adds additional material when to compared to the published article. Chapter §5 has not yet been published.

Chapter 2

Transverse forcing

This chapter was published as Ghirardo and Juniper (2013).

2.1 Abstract

This theoretical study investigates spinning and standing modes in azimuthally symmetric annular combustion chambers. Both modes are observed in experiments and simulations, and an existing model predicts that spinning modes are the only stable state of the system (Noiray, Bothien & Schuermans, 2011, Comb. Theory Modelling 15(5) 585–606). We extend this model to take into account the effect that the acoustic azimuthal velocity, u, has on the flames, and propose a phenomenological model based on experiments performed on transversely forced flames. This model contains a parameter, δ, that quantifies the influence that the transversal excitation has on the fluctuating heat release. For small values of δ, spinning modes are the only stable state of the system. In an intermediate range of δ, both spinning and standing modes are stable states. For large values of δ, standing modes are the only stable state. This study shows that a flame's response to azimuthal velocity fluctuations plays an important role in determining the type of thermo-acoustic oscillations found in annular combustors.

2.2 Introduction

Combustion systems such as aeroplane engines and rocket engines are often susceptible to large amplitude self-sustained pressure oscillations, called thermo-acoustic oscillations. These lead to excessive noise and sometimes to structural damage (Lieuwen and Yang, 2005). Self-sustained oscillations occur when the phase difference between

pressure fluctuations and heat release fluctuations is less than one quarter cycle, as described by Rayleigh (1878). These heat release fluctuations arise from the flames' response to incident velocity or pressure perturbations. The flames' response therefore plays a crucial role in determining a system's thermoacoustic behaviour. In this chapter, we use a low order model of a thermo-acoustic system to determine the implications of a flame response that has been observed experimentally in annular combustors.

Annular combustion chambers are commonly used in aircraft gas turbines because they fit efficiently between the axial compressor and turbine. Their circumference is much longer than their length and width, so thermoacoustic oscillations tend to develop in the azimuthal direction. If they travel in a clockwise or anticlockwise direction, with the pressure and velocity nodes travelling at the speed of sound, they are called spinning modes. If the nodes are fixed in space and the wave modulates its amplitude without travelling, they are called standing modes. Both types of mode are found in large eddy simulations (LES), experiments, and real engines. See for example Noiray and Schuermans (2013) for spinning modes and Wolf et al. (2012); Worth and Dawson (2013a) for both spinning and standing modes.

Schuermans et al. (2006) study an annular combustor as a network of acoustic elements, using a state space representation. Their linear stability analysis predicts that standing modes are linearly unstable. In time, however, these develop into a spinning mode, which they show is the only stable limit-cycle of the system. They show that this behaviour is also seen for a thermoacoustic model containing a one-dimensional wave equation and a nonlinear saturating pressure-dependent heat release. This model is similar to that which will be used in this chapter, in equation (2.11).

Noiray et al. (2011) consider the effect of a non-uniform heat-release in the azimuthal direction. If the acoustic mode has azimuthal dependence of the form $\cos(n\theta)$, they show that a non-uniform perturbation of heat release of the form $\cos(2n\theta)$ is particularly influential. The amplitude of this non-uniformity is labelled C_{2n}. For $C_{2n} = 0$, their analysis predicts that only spinning modes are stable. For larger values of C_{2n}, a sum of standing and spinning modes can be stable. Above a critical value of C_{2n}, only standing modes are stable.

This does not explain, however, why standing modes are the preferred state of the system in some rotationally symmetric configurations with $C_{2n} = 0$, as found in Wolf et al. (2012); Worth and Dawson (2013a). Combustors are very noisy environments, and one explanation could be that noise causes the thermo-acoustic oscillations to switch between different modes Bourgouin et al. (2013); Poinsot et al. (2011). Noiray and Schuermans (2013) discuss the effect of noise on the system presented by Noiray et al.

(2011), for a symmetric configuration (by setting $C_{2n} = 0$). The only deterministic, stable states of the system remain the two spinning modes, as it is when there is no noise. However noise can make the system jump between the two modes, and, when it does so, the system passes through the vicinity of a standing mode. Theoretical results and experimental data agree in presenting a probability density function of the state of the system with two clear peaks on the two spinning modes. However this is not consistent with Wolf et al. (2012) and with certain configurations of Worth and Dawson (2013a), where the system has a statistical preference for standing modes.

In summary, current thermoacoustic models cannot explain why standing modes in symmetric annular chambers should be a preferred state of the system, despite experimental evidence that they sometimes are. In this chapter we extend the work by Noiray et al. (2011), to include the influence of transversal flame excitation and show that a phenomenological model that includes transverse excitation can exhibit stable standing modes as well as stable spinning modes.

The chapter is organized as follows: In §2.3 we present a concise derivation of the one-dimensional equation (2.11) governing the problem. In §2.4 we discuss the model for the heat-release, taking into account the transversal forcing in §2.5. In §2.6 we discuss how to simulate equation (2.11) numerically and present some introductory results. In §2.7 we reduce the problem to a system of coupled oscillators, and in §2.8 we discuss its stability. We then apply the method of averaging and study the resulting phase space, providing a graphical description of the system in 3 dimensions.

2.3 Description of the problem

The geometry under investigation is a thin annular combustion chamber. We study this problem in cylindrical coordinates and time: $(z, R, \theta, t) \in [0\ z^*] \times [R_1\ R_2] \times [0\, 2\pi) \times [0\, \infty)$. z^* is the longitudinal length of the combustor, and R_1 and R_2 are the radii of the inner and outer surfaces. For simplicity, we consider R_1 and R_2 to be uniform in z. We consider mean and fluctuating variables, neglecting the influence of viscosity on the flow field. The momentum and pressure equations for the fluctuating variables, considering only first order acoustics (Culick, 2006), are

$$\overline{\rho}\frac{\partial \boldsymbol{u}'}{\partial t} + \nabla p' = 0 \tag{2.1}$$

$$\frac{\partial p'}{\partial t} + \gamma \overline{p} \nabla \cdot \boldsymbol{u}' = \overline{\rho}(\gamma - 1) q' \tag{2.2}$$

In this expression, the prime indicates fluctuating components, $\overline{\rho}$ and $\overline{p}$ are the mean density of the gas mixture and the mean pressure, $\gamma = c_p/c_v$ is the ratio of specific heat capacities, and q' is the fluctuating heat released by the combustion. Spatial averaging has already been applied, and the effects of a non-uniform speed of sound have been neglected (Culick, 2006). This is common to many other studies modelling this problem (Noiray et al., 2011; Sensiau et al., 2009). Terms of order $\mathcal{O}(\overline{\boldsymbol{u}})$ are neglected by assuming a low Mach number flow[1]. We study the problem in polar coordinates and drop the dependence on the radial coordinate because this is weak, even if the gap between the two cylinders is non-negligible (Lieuwen, 2012):

$$\overline{\rho}\frac{\partial u'}{\partial t} + \frac{1}{R}\frac{\partial p'}{\partial \theta} = 0 \tag{2.3}$$

$$\frac{\partial p'}{\partial t} + \frac{\gamma \overline{p}}{R}\frac{\partial u'}{\partial \theta} = \overline{\rho}(\gamma - 1)q' \tag{2.4}$$

Here, u' is the component of the velocity in the azimuthal direction and $R \approx (R_1 + R_2)/2$. We proceed by nondimensionalizing the equations, picking a new time scale:

$$t' = \frac{\overline{c}}{R}t \qquad \rightarrow \qquad \frac{\partial}{\partial t} = \frac{\overline{c}}{R}\frac{\partial}{\partial t'} \tag{2.5}$$

where $\overline{c}$ is the spatially averaged speed of sound. We introduce the nondimensional variables p^*, q^* and u^*, defined as

$$p' = \overline{\rho}\overline{c}^2 p^* \tag{2.6}$$

$$q' = \frac{\overline{c}^3}{R(\gamma - 1)}q^* \tag{2.7}$$

$$u' = \overline{c}u^* \tag{2.8}$$

The nondimensional system of equations, dropping the asterisks and the prime on the time variable, becomes:

$$\frac{\partial u}{\partial t} + \frac{\partial p}{\partial \theta} = 0 \tag{2.9}$$

$$\frac{\partial p}{\partial t} + \frac{\partial u}{\partial \theta} = q - \alpha p \tag{2.10}$$

[1] the azimuthal component of the mean field is induced only by the injectors' swirlers, and is negligible

In this expression we have included a damping term, with a coefficient $\alpha > 0$. Equations (2.9) and (2.10) are equivalent to the wave equation, with $\partial q/\partial t$ as a source term:

$$\frac{\partial^2 p}{\partial t^2} + \alpha \frac{\partial p}{\partial t} - \frac{\partial^2 p}{\partial \theta^2} = \frac{\partial q}{\partial t} \tag{2.11}$$

This model has been the common starting point of Noiray et al. (2011); Noiray and Schuermans (2013). It is the one dimensional counterpart of the model studied by Sensiau et al. (2009), where the whole three dimensional field is considered. This simplification is not appropriate for the study of radial and longitudinal instabilities, but allows an analytical treatment of azimuthal instabilities.

2.4 Heat release constitutive equation

The heat release fluctuations, q, are often assumed to depend either on velocity, pressure, or both, with the inclusion of one or more time delays. However, we start from the analysis of Noiray et al. (2011), where q is a function of p only:

$$q = f(p) \tag{2.12}$$

$$f(p) = \beta p - \kappa p^3 \tag{2.13}$$

The first term depicts linear growth governed by β for small fluctuating pressures. The second term in (2.13) is a nonlinear cubic saturation, governed by a coefficient κ. For any given $\kappa > 0$, the study of equation (2.11) in terms of a new pressure variable $\tilde{p} \equiv p\sqrt{\kappa}$ leads to a new problem independent of κ. It follows that the coefficient κ induces simply a rescaling of the problem, and will be set to 1 in the following analysis. By assuming $q = f(p)$ to be an odd function of p, (2.13) is a 4^{th}order-accurate Taylor expansion of f. The analysis carried out in this chapter could easily be extended to higher-order terms.

The theory developed in Noiray et al. (2011) based on (2.12) does not predict stable standing modes for symmetric configurations, which are observed as preferred state of the system in Wolf et al. (2012); Worth and Dawson (2013a). The universal validity of (2.12) is then called into question, particularly the assumptions of (2.12), which are (i) the absence of a time delay in p and (ii) the independence of q on anything else except p.

Regarding the first point, q has been found to be reasonably in phase with p in a LES simulation of a specific, symmetric rig (Wolf et al., 2012). In that rig, both

standing and spinning modes are observed, suggesting that standing modes are possible in the absence of a time delay. Since the aim of this chapter is to explain how standing modes are possible in symmetric systems, we do not consider a time delay and assume that p and q are in phase, leaving this investigation for further research. Some results based on linear stability, applied to an $n-\tau$ model, discussing the importance of the time delay can be found in Sensiau et al. (2009).

Regarding the second point, one possibility is to assume that the heat release depends on the azimuthal coordinate, since combustion happens mainly near the injectors. This can be done by introducing a shape function $\psi(\theta)$, which is large near the flames and small far from the flames:

$$q = \psi(\theta) f(p) \tag{2.14}$$

$$\psi(\theta) = \frac{1+\cos(M\theta)}{2}, \qquad \text{where } M \text{ is the number of injectors} \tag{2.15}$$

The expression (2.15) is one of the many possibilities for such a shape function. The adoption of the constitutive equation (2.14) instead of (2.12) in the analysis we will develop next does not lead to any qualitative differences in the stability analysis of the standing and spinning modes, and will therefore not be discussed further. This means that a spatially accurate description of the heat-release does not explain standing modes in symmetric annular chambers, and therefore suggests that it is sufficient to consider spatially averaged models for the heat release q. We stress that this statement does not apply to non-symmetric annular combustors, in which the shape function ψ is no longer $M-$periodic in the azimuthal direction, and in the very specific case where $M = 2n$ in (2.15), where n is the unstable acoustic mode. This latter case is covered by the stability analysis of Noiray et al. (2011), and shows that mixed modes and standing modes are possible. In this case, the shape function has peaks at the pressure antinodes, and troughs at the pressure nodes of the standing mode.

One other possibility is to assume, in addition to the dependence of p, a dependence of q on the azimuthal velocity u, which excites transversally the flames. This possibility is investigated in this chapter.

2.5 Model of transversal forcing

The effect of transverse excitation on swirling premixed flames is a current topic of research. Hauser et al. (2011) report that an asymmetric perturbation of higher OH intensity is generated by the transversal velocity. This asymmetric region of stronger

combustion spirals around the injector at the forcing frequency. This asymmetry persists also in addition to longitudinal forcing, suggesting that the two phenomena are superposable.

We report in Figure 2.1 two phase-averaged chemiluminescence images of flames at a pressure antinode (velocity node) and at a pressure node (velocity antinode), kindly provided by James Dawson and Nicholas Worth.

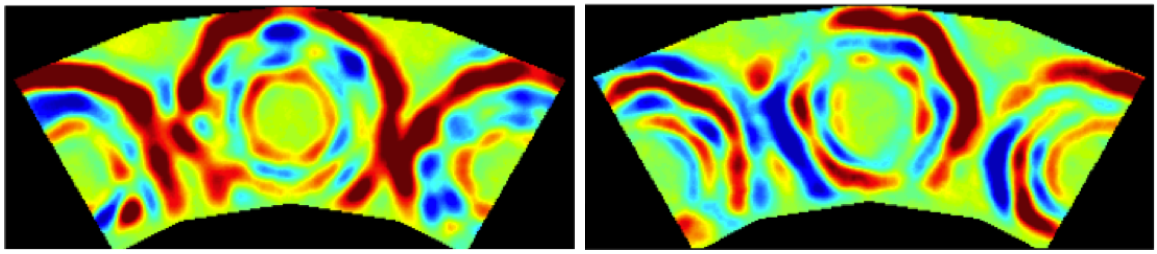

(a) pressure antinode (b) velocity antinode

Fig. 2.1 Phase-averaged chemiluminescence images of a standing mode limit cycle in an annular combustor. The images were taken, looking upstream, at two different azimuthal locations. In (a) the flame at the centre is at a pressure antinode, where there are no azimuthal velocity fluctuations; the chemilumnescence is approximately axisymmetric. In (b) the flame at the centre is at a velocity antinode, where the azimuthal velocity fluctuations are maximal; the chemiluminescence is approximately anti-symmetric. The experimental configuration is described in Worth and Dawson (2013a,b).

In figure 2.1, at pressure antinodes there is no transverse velocity excitation. Circles of positive/negative heat release are shed from the injector and propagate outwards. The fluctuating heat release is found to be approximately axisymmetric around the injector: at every instant in time of a limit-cycle, the phase of the perturbation is approximately axisymmetric. This is consistent with O'Connor and Lieuwen (2012), where the vorticity disturbance is symmetric around the injector at pressure antinodes. At velocity antinodes the symmetry of the perturbation breaks: the heat release is found to be approximately in anti-phase on the two sides of the flame, in the direction of the transverse velocity. In O'Connor and Lieuwen (2012) the same break of symmetry happens for vorticity disturbances, which are asymmetric at velocity antinodes. This means that the spatially averaged heat release fluctuation of an injector is smaller at velocity antinodes. This happens because, in the averaging, the zones in anti-phase cancel out in Figure 2.1.b. Since the flame diameter is small compared to the wavelength of the unstable acoustic mode, we can assume that the flame is acoustically compact,

and spatially average the heat release on each burner[2]. Based on this observation, we assume that the fluctuating heat release of an injector is smaller if a transverse excitation is present, introducing a dependence on the velocity u:

$$q(p,u) = f(p)\mu(u) \tag{2.16}$$

In this expression, f is the same function introduced in (2.13), and all the previous considerations apply to it. The function μ is the degree of symmetry of q around a burner, and must be unity for zero transverse excitation, and smaller than 1 for $u \neq 0$, in the range of velocities investigated:

$$0 \leq \mu(u) \leq 1 \ \wedge \ u\frac{\partial \mu}{\partial u}(u) \leq 0 \tag{2.17}$$

We study two possibilities for μ:

$$\mu(u) = 1 - \delta|u| \qquad \text{Case A} \tag{2.18}$$

$$\mu(u) = 1 - \delta u^2 \qquad \text{Case B} \tag{2.19}$$

where δ is a positive coefficient that expresses how strongly the transverse forcing influences the heat release. Both models must respect (2.17) at every instant of time. The structure (2.16) and the choice of μ in (2.18,2.19) are not intended to be an accurate representation of the flame's behaviour, because they are based on qualitative observations. The model is phenomenological, and the aim is to discuss the effect of transverse forcing on the stability of standing and spinning modes on a qualitative level.

2.6 Numerical setup

Because it is not straightforward to evaluate the time derivative of q in equation (2.11), we opt to study the system of equations (2.9) and (2.10), where such a derivative is not required. We project the equations into Fourier space, obtaining a system of ordinary differential equations. The generic n^{th} complex Fourier mode is governed by

[2]See also the comment on the use of spatially averaged models for q in the previous section.

the equations

$$\begin{cases} u'_n &= -inp_n \\ p'_n &= -inu_n - \alpha p_n + q_n \end{cases} \qquad \forall n = 1, 2, ..., N_f. \tag{2.20}$$

Since q is a nonlinear function of u and p, at each timestep the two functions $u(\theta)$ and $p(\theta)$ are evaluated from the Fourier coefficients $\{u_n\}$ and $\{p_n\}$, and then $q(\theta)$ is calculated as $f(p(\theta))\mu(u(\theta))$. Finally the $\{q_n\}$ coefficients are evaluated as a Fourier transform of $q(\theta)$. The system (2.20) can then be numerically integrated with a numerical scheme.

The damping of this problem has to be adjusted to avoid excessive growth of higher order harmonics.

Specifically, we consider only the dissipation due to the boundary layers, which scales as the square root of the frequency (Culick, 2006; Landau and Lifshitz, 1978). We take this into account fixing $\alpha_n = \alpha\sqrt{n}$ in (2.20).

Two examples of two simulations showing a spinning and a standing mode are reported in Figure 2.2, truncating the number of Fourier modes to $N_f = 161$. The two pictures do not imply that the two modes are stable, and only time marching for a long time allows us to check this at this stage[3]. We present here both cases A and B only to show what the two different μ functions defined in (2.18) and (2.19) look like. Both cases present spinning modes for small values of δ and standing modes for large values of δ.

The existence of a standing mode at one value of δ and a spinning mode at another is a key result of this chapter. In the next sections we conduct a stability analysis of these modes to confirm that they are indeed both stable limit cycles of the nonlinear governing equations.

2.7 Reduction to a system of coupled oscillators

In this section we carry out spatial averaging in the azimuthal direction, in the same way carried out by Noiray et al. (2011). When annular combustors are subject to azimuthal instabilities, there is usually only one strong Fourier component, which corresponds to the n^{th} lowest acoustic mode of the chamber. This is apparent from the power spectral density (PSD) of the Fourier transform of pressure signals from experiments (see for example Worth and Dawson (2013b)), and is also observed in the

[3]The two modes in the two cases will be proved to be stable later with rigour.

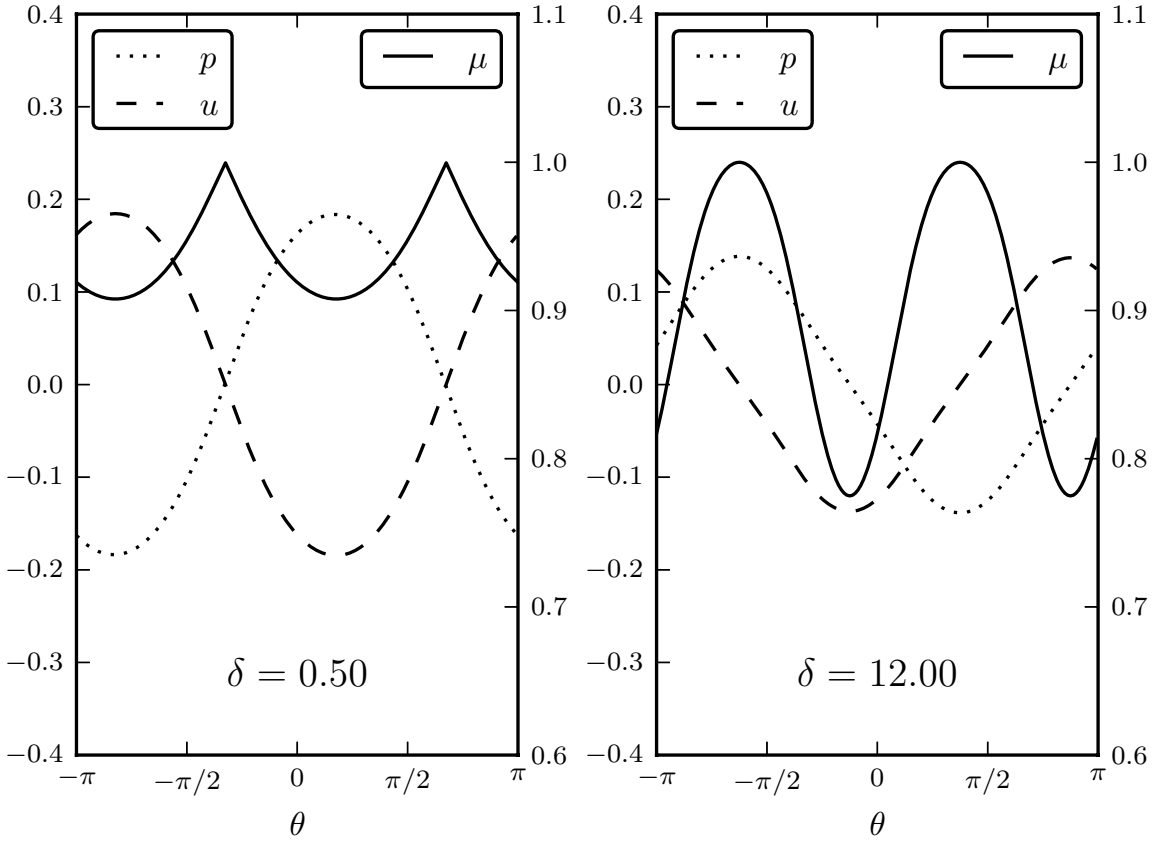

(a) Stable spinning mode

(b) Stable standing mode

Fig. 2.2 Instantaneous snapshots of two simulations, for $\alpha = 0.08, \beta = 0.10$. Pressure and velocity values are reported on the left scale, while $\mu(u(\theta))$ values are reported on the right scale. *a)* μ from case A, $\delta = 0.5$. The pressure and velocity waves travel either to the left (if in antiphase, as in this case) or to the right (if in phase). δ is small, so the influence of the transverse velocity forcing is small, and the spinning mode is stable. The curve $\mu(\theta)$ also travels left, following the two waves. *b)* μ from case B, $\delta = 12$. The velocity and pressure are standing waves, and their nodes are fixed in space; pressure nodes corresponds to troughs of μ, and velocity nodes correspond to peaks of μ. At the instant in time when the velocity is zero in all the domain, the function μ is unitary in all the domain.

numerical solutions of (2.20). We truncate the modal expansion and consider only the n^{th} mode:

$$u(t,\theta) = n\eta_1(t)\sin(n\theta) - n\eta_2(t)\cos(n\theta) \tag{2.21}$$

$$p(t,\theta) = \eta_1'(t)\cos(n\theta) + \eta_2'(t)\sin(n\theta) \tag{2.22}$$

where the second expression was obtained substituting (2.21) into (2.9). We now apply spatial averaging (Culick, 2006) to this system: we substitute (2.21) and (2.22) into (2.10), multiply the expression by $2\cos(n\theta)$, and then average over 2π in the azimuthal coordinate, obtaining (2.23):

$$\eta_1'' + \alpha\eta_1' + n^2\eta_1 = F_1 \tag{2.23}$$

$$\eta_2'' + \alpha\eta_2' + n^2\eta_2 = F_2 \tag{2.24}$$

Here, (2.24) has been obtained similarly by multiplying by $2\sin(n\theta)$. Notice that these expressions are exact, and the assumption that higher order modes are negligible is applied assuming that the two source terms F_i on the RHS depend only on the Fourier modes η_1 and η_2. They are:

$$F_1 = \frac{1}{\pi}\int_0^{2\pi} q\Big(\eta_1'\cos(n\theta) + \eta_2'\sin(n\theta), n\eta_1\sin(n\theta) - n\eta_2\cos(n\theta)\Big)\cos(n\theta)d\theta \tag{2.25}$$

$$F_2 = \frac{1}{\pi}\int_0^{2\pi} q\Big(\eta_1'\cos(n\theta) + \eta_2'\sin(n\theta), n\eta_1\sin(n\theta) - n\eta_2\cos(n\theta)\Big)\sin(n\theta)d\theta \tag{2.26}$$

We can study the system in the new timescale $t' = nt$, and obtain:

$$\eta_1'' + \alpha\eta_1' + \eta_1 = f_1(\eta_1, \eta_2, \eta_1', \eta_2') \tag{2.27}$$

$$\eta_2'' + \alpha\eta_2' + \eta_2 = f_2(\eta_1, \eta_2, \eta_1', \eta_2') \tag{2.28}$$

where $\alpha \shortmid\longrightarrow \alpha/n$, and the expressions of $f_i \equiv F_i/n^2$ and how to evaluate them are reported in the appendix §2.11.2.11.1. This is a system of coupled oscillators, which can be numerically integrated in time in a 4-dimensional phase space, as opposed to the phase space with N_f dimensions introduced in (2.20).

Amplitudes and phase representation

Instead of studying the system in terms of displacements, η_i, and velocities, η_i', it is more useful to study it in terms of amplitudes and phases,

$$\eta_1(t) = A(t)\cos(\omega t + \varphi_1(t)) \tag{2.29}$$

$$\eta_1'(t) = -A(t)\omega\sin(\omega t + \varphi_1(t)) \tag{2.30}$$

$$\eta_2(t) = B(t)\cos(\omega t + \varphi_2(t)) \tag{2.31}$$

$$\eta_2'(t) = -B(t)\omega\sin(\omega t + \varphi_2(t)) \tag{2.32}$$

mode	Amplitudes and phase	Trajectory in the plane (η_1, η_2)
spinning	$\phi = \pm\pi/2, \quad A = B$	circle
standing	$\phi = \pm\pi$, arbitrary A, B	line with arbitrary slope

Table 2.1 Characterization of spinning and standing modes

In these expressions, the frequency ω can in principle be perturbed by the parameters of the problem from the the natural frequency of the two oscillators, which is 1. Equations (2.27) and (2.28) are symmetric in η_1, η_2. It is useful to introduce the phase difference between the two oscillators, $\phi(t) \equiv \varphi_1(t) - \varphi_2(t)$. If ϕ settles to $\pm\pi/2$ and $A = B$, then the substitution of (2.30) and (2.32) into (2.22) shows that the pressure distribution corresponds to a spinning mode in the counterclockwise/clockwise direction respectively:

$$p(t, \theta) = -A\omega \sin(\omega t + \varphi_1 \mp n\theta) \tag{2.33}$$

This solution spins in the azimuthal direction as in Figure (2.2.a). On the other hand, if ϕ settles to π or 0, there is a standing mode, for any value of A, B:

$$p(t, \theta) = \omega \sin(\omega t + \varphi_1)(-A\cos(n\theta) \pm B\sin(n\theta)) \tag{2.34}$$

The pressure nodes can be found by studying the zeros of the θ-term in (2.34). They are fixed in space, as shown in Figure (2.2.b). It is convenient to examine the two cases in the (η_1, η_2) plane as a function of time. With reference to equations (2.29-2.32), the two modes give rise to limit-cycles which are either circles or lines. The situation is summarized in table 2.1. Figure 2.3 shows two simulations of trajectories in the (η_1, η_2) plane for case B. This is similar to Figure 11 in Schuermans et al. (2006). It is worth noting that the complex number $C(t) = 2(\eta_1(t) + i\,\eta_2(t))$ is the indicator proposed by Poinsot et al. (2011) to study the nature of these modes. The two cases have different values of δ, and lead to either spinning or standing limit-cycles. The simulations have been started with nearly the same initial condition for ϕ, and from two random values for A, B.

The main objective of this section has been to reduce the original partial differential equation to a system of coupled oscillators, and to present a simpler way to look at standing and spinning modes in terms of amplitudes and phase in the (η_1, η_2) plane. In the next section we will perform a stability analysis of these modes, and in the last section we will present a phase space realization of the system in terms of the two amplitudes and of the phase here introduced.

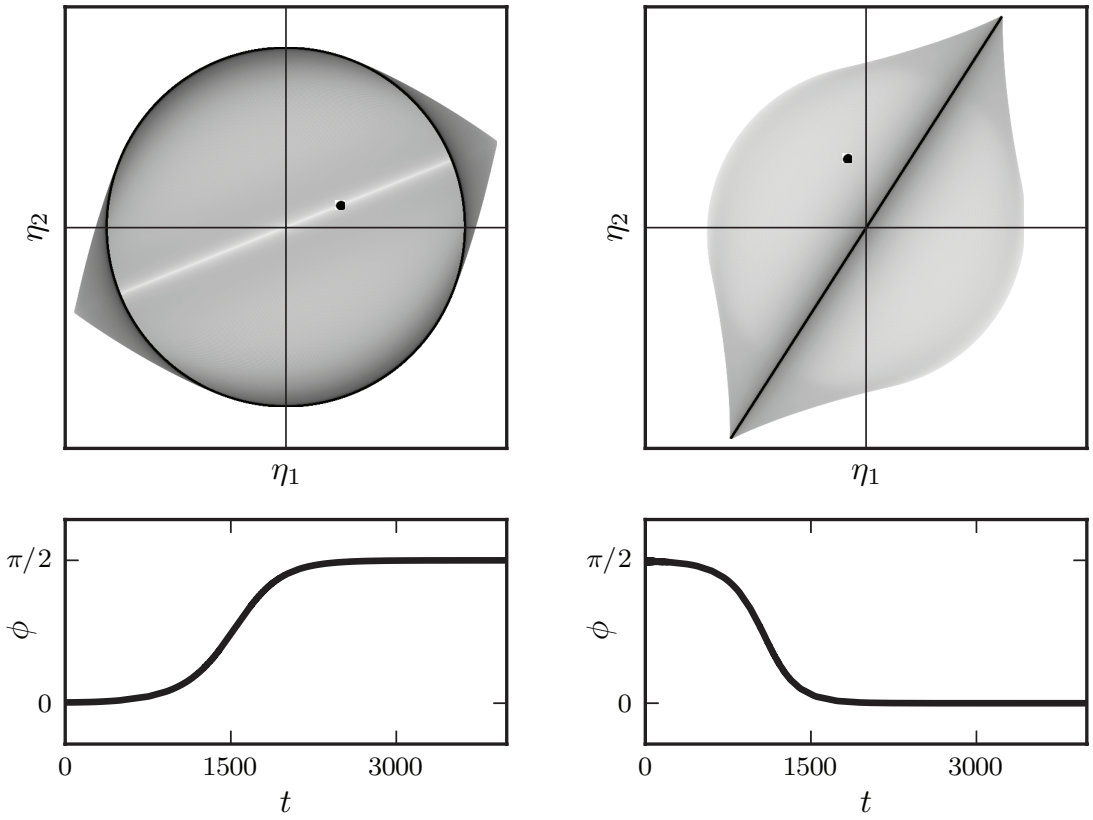

(a) $\delta = 3$. Transition to a spinning mode (b) $\delta = 12$. Transition to a standing mode

Fig. 2.3 Temporal evolution to stable limit cycles, for two different values of δ. In both simulations, $\alpha = 0.08, \beta = 0.10$, and μ is from case B. The top plots show the trajectory of the system in the (η_1, η_2) plane; The black dot is the initial position and the darkness of the line is proportional to the simulation time t. In this plane, spinning modes are circles around the origin, and standing modes are lines centred on the origin, at an arbitrary angle that depends only on the initial conditions. In the left frames, the spinning mode is stable. In the right frames, the standing mode is stable. The bottom plots show the temporal evolution of the phase ϕ between the two oscillators. The values of ϕ can be compared with those in table 2.1.

2.8 Stability of the coupled oscillator system

We first report some results from the linear analysis of the fixed point $p(t, \theta) = u(t, \theta) = 0$ of the system (2.27,2.28). This fixed point is stable for $\beta < \alpha$. A double Hopf bifurcation occurs at $\beta = \alpha$, where two complex eigenvalues cross the imaginary axis at the same time. Similarly, Sensiau et al. (2009) perform a linear stability analysis

of an azimuthally symmetric chamber and find two linearly unstable spinning modes with exactly the same growth rate. They conclude that, in perfectly symmetric systems, the sum of the two identical spinning modes would lead to a stable standing mode. This is not the case, however, as shown by the fact that, for $\delta = 0$, and $\beta > \alpha$, this system converges to a stable spinning mode, in accordance with Schuermans et al. (2006).

We proceed by analysing the case of the oscillating system, fixing $\alpha = 0.08$ and $\beta = 0.10$, and focusing on case A. Figure 2.3 shows that two different values of δ lead to two different limit cycles: a spinning mode and a standing mode. We now study the system over a range of δ. To do this, we numerically integrate the system until it converges to a limit cycle, and then track the limit cycle as we vary δ using MatCont, a numerical continuation package (Dhooge et al., 2003). Figure 2.4 shows the stability of the spinning and standing modes.

For $\delta = 0$, the spinning mode is stable, because all its Floquet multipliers are smaller than 1 in Figure 2.4.a. At $\delta_{c2} \approx 1.027$, the modulus of two Floquet multipliers crosses 1, which corresponds to a subcritical[4] Neimark-Sacker bifurcation at which the spinning mode becomes unstable. The argument of these two Floquet multipliers, shown in Figure 2.4.c, is small. Notice that, for $\delta > \delta_{c2}$, there is one multiplier with modulus smaller than 1 and two multipliers with modulus greater than 1. This means that the system is attracting from an invariant manifold[5] with dimension 1, and repelling to another invariant manifold with dimension 2. This is consistent with Figure 2.3.b, where the point is first attracted to the spinning mode (circular line) before being repelled towards a standing mode (straight line).

For the standing mode, for every value of δ, two multipliers are exactly equal to 1. One of these is due to the fact that the system is at a limit-cycle and any movement in the direction of the limit cycle remains on the limit cycle (the spinning mode has one too, under the horizontal black line in Figure 2.4.a). The other is due to the fact that the nodes of the standing mode can rotate arbitrarily around the annulus - i.e. the black line in Figure 2.3.b can take any angle with the axes. A fold bifurcation occurs at $\delta_{c1} = 0.949$, making the mode stable for $\delta > \delta_{c1}$. Notice that, for $\delta < \delta_{c1}$, there is one multiplier with modulus smaller than 1 and one multiplier larger than 1. This means that the system is attracting from a 1-dimensional invariant manifold and repelling from another 1-dimensional invariant manifold. This can be seen in Figure

[4]based on the first Lyapunov exponent, which is positive

[5]for the purposes of this chapter, an invariant manifold can be thought of as a particular surface in the phase space such that all points on it are either attracted to or repelled from the same limit-cycle or fixed point. Refer to Guckenheimer and Holmes (1983) for a rigorous definition.

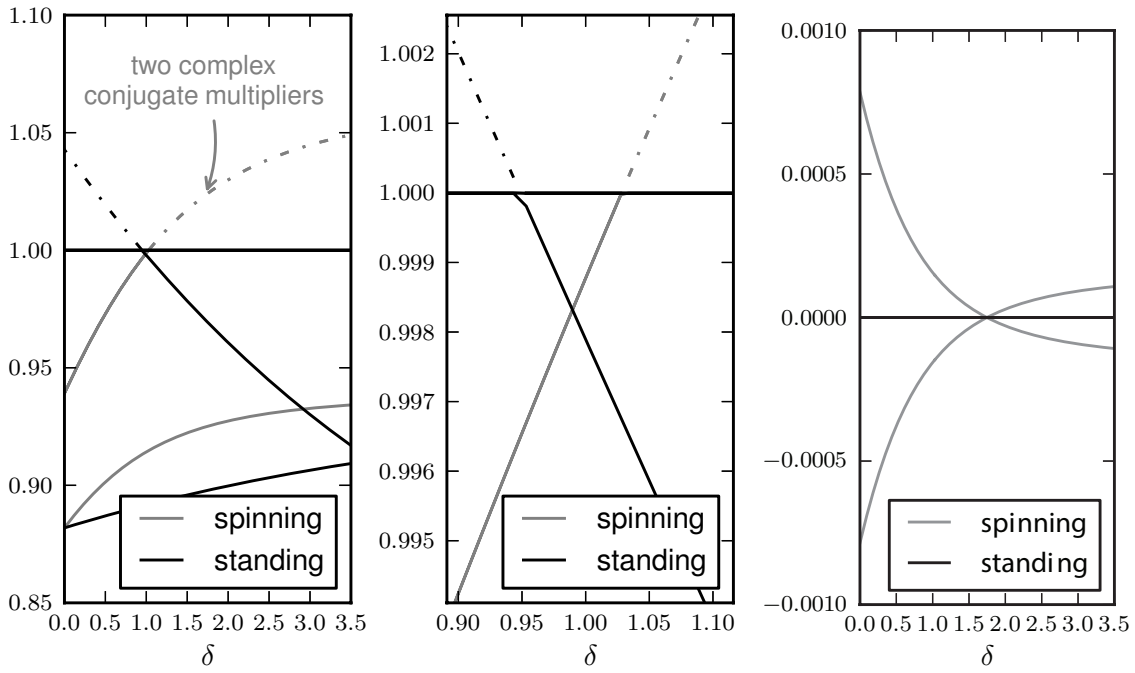

(a) Modulus of the Floquet multipliers

(b) Zoom of Figure (a)

(c) Argument of the Floquet multipliers

Fig. 2.4 Stability of standing and spinning limit-cycles with respect to the transversal forcing parameter δ. (a) Modulus of the Floquet multipliers of both modes. To each multiplier corresponds an invariant manifold on which the system is attracted towards the limit-cycle if the modulus is smaller than 1 (continuous lines) or repelled from the limit-cycle if the modulus is larger than 1 (dashed lines). One limit-cycle is unstable if there is at least one multiplier larger than 1. From (a), for small values of δ only the spinning mode is stable, and for large values of δ only the standing mode is stable. The standing limit cycle has two coincident multipliers equal to 1, while the spinning limit cycle has only one multiplier equal to 1 (not visible, covered by the black line) and a couple of complex conjugate multipliers (indicated with the arrow). From the zoom in (b), we observe there is a range of δ where both modes are stable. (c) Argument of the Floquet multipliers, which is needed to discuss the type of bifurcation at criticality. The two non-zero arguments of the spinning mode belong to the complex conjugate pair presented in (a).

2.3.a, where for a while the solution lingers as a standing mode (straight line) before being repelled towards the spinning mode (circle line).

The angular frequency of the limit cycles is not changed by the nonlinearities of the problem: in the range of parameters investigated, the period of oscillations was found to be constant and equal to 2π. In summary:

- for $\delta < \delta_{c1} \approx 0.949$ only the spinning mode is stable;

- for $\delta > \delta_{c2} \approx 1.027$ only the standing mode is stable;

- for $\delta_{c1} < \delta < \delta_{c2}$, the system is multistable, with both standing and spinning modes stable.

Moreover, for $\delta < \delta_{c1}$ and $\delta > \delta_{c2}$ the unstable mode attracts the solution on a 1-dimensional invariant manifold, before repelling it towards the stable mode.

We checked that these stability results, obtained for the system (2.27,2.28), apply also to the original system (2.11) by performing numerical simulations of (2.20) for different values of δ. For each value of δ, we started the simulation with both standing and spinning modes as initial conditions, and evaluated their stability by time-marching. The same qualitative picture was found, with the two critical values of δ confined in these intervals: $0.9 < \delta_{c1} < 1.0$, and $1.1 < \delta_{c2} < 1.2$, in good agreement with the values just presented. This shows that the reduction to a system of coupled oscillators by considering only the fundamental unstable harmonic, as presented in section §2.7, is a powerful tool to study the stability of the original wave equation (2.11), at least for the values of α, β investigated here.

We do not report here the analysis for case B, because the overall behaviour is the same as that of case A.

2.9 Slow flow

In this section we apply the method of averaging to the system of coupled oscillators (2.27,2.28) for case B. We will obtain a new system of differential equations in terms of the amplitudes of oscillation A, B and of the phase difference ϕ, introduced from equation (2.29) onwards. This will reduce the dimensions of the problem from 4 to 3, allowing us to visualize the complete dynamics of the problem. The method of averaging (Sanders and Verhulst, 2007) gives the following formulation of the slow flow:

$$\begin{cases} A' = & -\frac{\alpha}{2}A - \langle s_1 f_1 \rangle \\ B' = & -\frac{\alpha}{2}B - \langle s_2 f_2 \rangle \\ \phi' = & \frac{1}{B}\langle c_2 f_2 \rangle - \frac{1}{A}\langle c_1 f_1 \rangle \end{cases} \tag{2.35}$$

where $s_i \equiv \sin(\omega t + \varphi_i)$ and $c_i \equiv \cos(\omega t + \varphi_i)$, and the averaging operator of a generic function h is introduced as

$$\langle h(\eta_1, \eta_1', \eta_2, \eta_2') \rangle \equiv \frac{\omega}{2\pi} \int_t^{t+\frac{2\pi}{\omega}} h\Big(A\cos(\omega t + \varphi_1), \\ -A\omega \sin(\omega t + \varphi_1), \\ B\cos(\omega t + \varphi_2), \\ -B\omega \sin(\omega t + \varphi_2) \Big) dt \tag{2.36}$$

Notice that, while in the definitions (2.29-2.32) the amplitudes and the phases are functions of time, they are constants in the RHS of (2.36). We fix $\omega = 1$, consistent with the period being 2π as reported earlier. Some details on how to tackle the four integrals can be found in appendix §2.11.2, together with the full equations of the system (2.35).

From now on we fix, as previously, $\kappa = 1, \alpha = 0.08, \beta = 0.1$. The two critical values of δ for standing and spinning modes are respectively $\delta_{c1} \approx 6.2076$ and $\delta_{c2} \approx 6.2165$. We can then visualize this phase space in terms of A, B, and ϕ, as a function of δ. The amplitudes A, B are non-negative numbers, and $\phi \in [0\,,\, 2\pi]$. Since the phase space is symmetric with respect to the planes $\phi = k\pi/2$ with $k = 0, 1, 2$, we restrict the visualization to $\phi \in [\pi/2\,,\, \pi]$. The system is also symmetric with respect to the plane defined by $A = B$.

Because of the difficulty of drawing a 3 dimensional phase space, we report the flow on a few invariant manifolds. These completely describe the stability of the problem[6]. Figure 2.5 shows two convenient slices of the same phase space for $\delta = 3$. In the picture, every shaded surface is an invariant manifold, and all invariant manifolds are reported, with the exception of the two planes $A = 0$ and $B = 0$, and the plane $A = B$, which is reported in Figure 2.7. In Figure 2.5, only the spinning mode is stable, because $\delta < \delta_{c1}$. We then fix $\delta = 12 > \delta_{c2}$ and present the same slices of the phase space in Figure 2.6, in which only the standing mode is stable.

In this representation, the addition of a non-zero asymmetry parameter, C_{2n}, as proposed in Noiray et al. (2011), shifts the red point of Figure 2.5 towards one of the A, B axes, maintaining it on the same plane $\phi \pm \pi/2$. Doing so, the system exhibits a superposition of standing and spinning modes. As discussed by Noiray et al. (2011), above a certain threshold the red point hits and gets stuck on one of the A, B axes, becoming a pure standing mode. The current analysis shows that, with the addition of transverse forcing introduced in (2.16), with $\mu(u)$ from case B as defined in

[6]The flow perpendicular to an invariant manifold is zero

(2.19), the standing mode becomes stable in a different way, without passing through a superposition of standing and spinning modes. It is worth noting that this analysis could easily be extended to include the parameter C_{2n} in order to discuss the stability of transverse forcing in non-symmetric annular chambers.

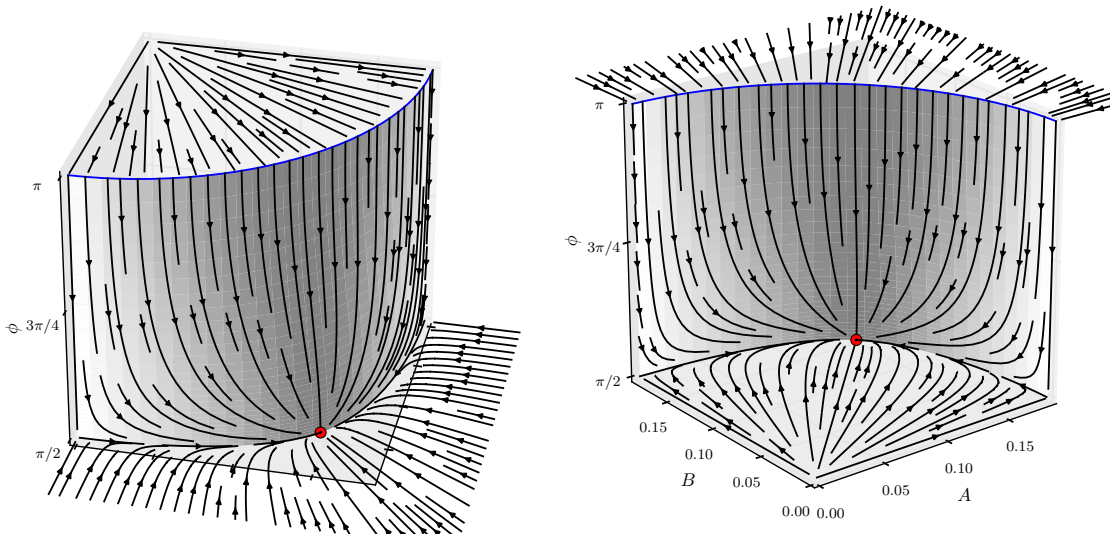

(a) Front view

(b) Back view

Fig. 2.5 Two views of the 3D phase space, in terms of the amplitudes A and B of the two modes and of the phase ϕ between them. $\delta = 3 < \delta_{c1}$. The line $A = B = 0$ corresponds to the trivial solution with zero pressure and velocity in the whole domain. The three surfaces are invariant manifolds and the direction of the local vector field, which is tangential to them, is described by the arrows. The spinning mode is reported as a red dot, and the standing mode as a blue arc. For this value of δ, the spinning mode is stable and the standing mode is unstable. The phase space is symmetric with respect to the plane $\phi = \pi$, with the image of the red dot under symmetry indicating a spinning mode with the opposite azimuthal direction. There is one more invariant manifold, which is a vertical plane defined by the condition $A = B$, which is also a second plane of symmetry of the phase space. It is reported in Figure 2.7.

2.10 Conclusions

This study improves the current understanding of standing and spinning modes in symmetric annular combustion chambers, which is the subject of current research Noiray and Schuermans (2013); Schuermans et al. (2006); Sensiau et al. (2009); Wolf et al. (2012); Worth and Dawson (2013b). The starting point of this study is the model

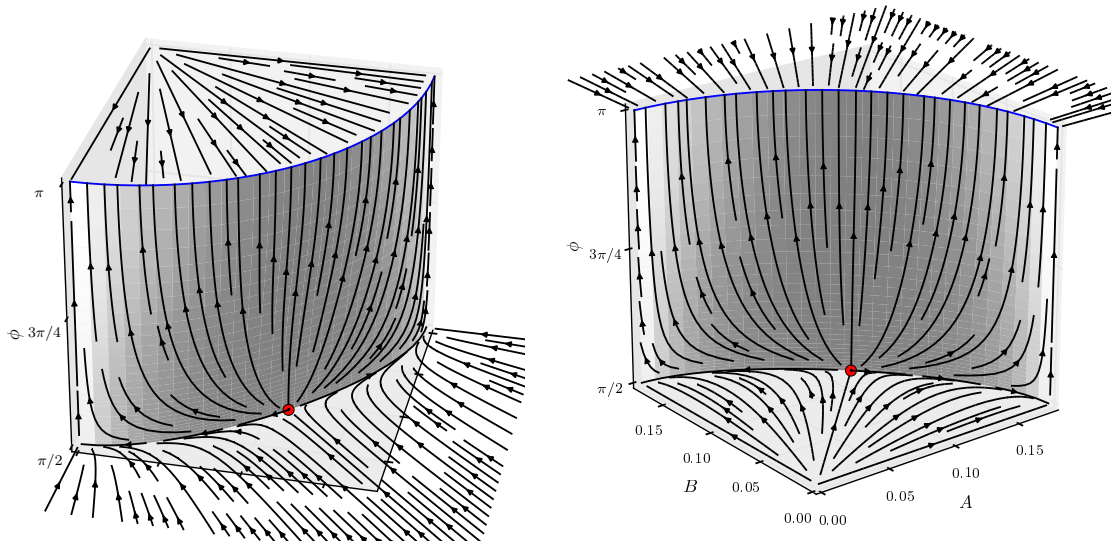

(a) Front view (b) Back view

Fig. 2.6 Two views of the same 3D phase space with $\delta = 12 > \delta_{c2}$. In comparison with Figure 2.5, there is now a change of direction of the arrows on the nonplanar surface. For this value of δ the standing modes (blue arc) are now stable, and the spinning mode (red dot) is unstable.

proposed in Noiray et al. (2011): the fluctuating heat release q is assumed to grow linearly and saturate nonlinearly as the pressure increases, as $q = f(p) = \beta - \kappa p^3$. In our analysis, we add an extra dependence, which reflects experimental observations Hauser et al. (2011); Worth and Dawson (2013b): the fluctuating heat release fluctuates axisymmetrically at velocity nodes (pressure antinodes), while it fluctuates from side to side at velocity antinodes (pressure nodes), as in Figure 2.1. When integrated over a sector of the chamber, the q fluctuations are larger in the first case. We then assume that $q = f(p)\mu(u)$, and we study two ways in which q can depend on u. We consider a case A with $\mu(u) = 1 - \delta|u|$, and a case B with $\mu(u) = 1 - \delta u^2$.

For both cases, we find that: (i) for small δ, only spinning modes are stable; (ii) for intermediate δ, both standing and spinning modes are stable, and the system is multistable; (iii) for large δ, only standing modes are stable. We show that this standing mode is fundamentally different from the one found in Noiray et al. (2011) in non-symmetric chambers, and it affects the phase space in a different way, as described in §2.9 for case B.

Another result is that, when the system has only one stable limit-cycle, the other unstable limit-cycle is not a repellor: it attracts the solution on one invariant manifold, and repels it on another. Figure 12 in Schuermans et al. (2006) suggests that the same

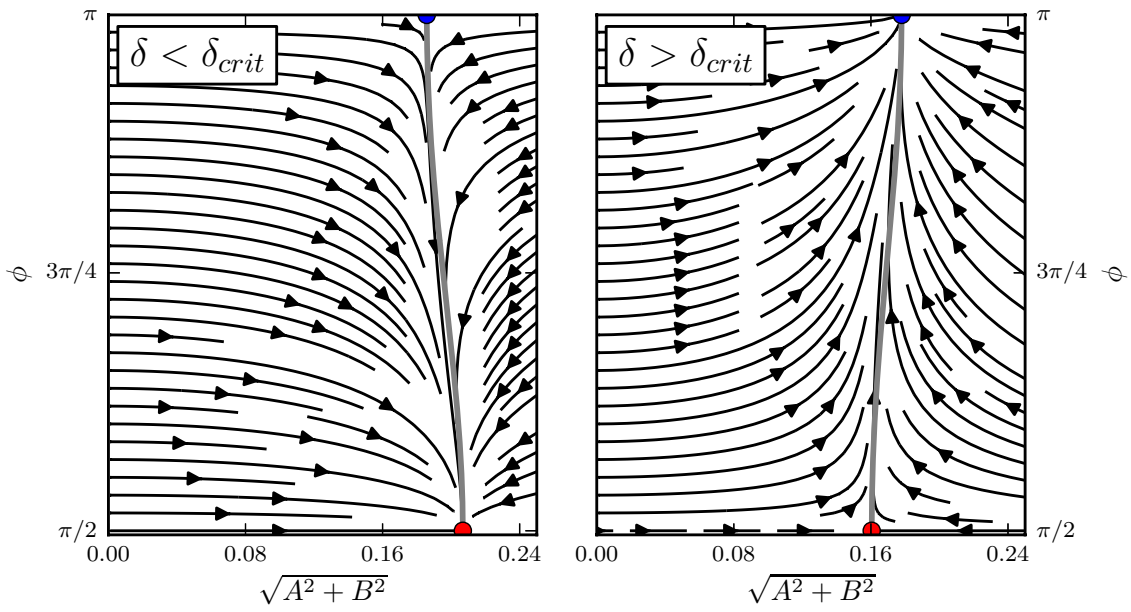

Fig. 2.7 Dependence of the slice $A = B$ of the phase space on the transversal forcing parameter δ. This slice is an invariant manifold, since the normal component of the field is constantly zero. On the left $\delta = 3 < \delta_{c1}$ and the spinning mode (red dot) is stable; on the right $\delta = 12 > \delta_{c2}$ and the standing mode (blue dot) is stable. Notice that the parameter δ changes qualitatively only the vertical component of the vector field, as could be inferred from the previous 3D pictures. Along the ϕ axis, i.e. for $A = B = 0$, the ϕ component of the vector field is zero in both cases. (Online version in colour.)

property applies also to their system. If this property holds in industrial combustors, noise could randomly shift the point in the phase space also to the attracting manifold of the unstable mode, and the system could linger for longer close to the unstable mode before decaying to the stable one. We give an example of this transient behaviour in Figure 2.3, and we comment on it based on the stability results in §2.8.

The analysis can be extended by adding higher order terms in u and p to the model for q in order to match the model to results from experiments on a single injector. The analysis can be extended to complex geometries, as long as the flame is acoustically compact.

We mention that the oscillators formulation (2.27) and (2.28), and the slow flow equations (2.35) can both be used as a physically-based model of the combustion process for purposes of control.

This work suggests that transversal forcing plays an important role in annular combustion instabilities, and should be taken into account to accurately predict

instabilities in annular configurations. The experimental characterization of a single injector to longitudinal forcing seems to not be sufficient to predict the final state of the combustor.

2.11 Appendices

2.11.1 Spatial Averaging

This appendix includes the terms on the RHS of (2.27,2.28), evaluated with the help of a computer algebra system. For case B, they are

$$f_1(\eta_1,\dot\eta_1,\eta_2,\dot\eta_2) = \frac{1}{8}\left(2\delta\eta_1\eta_2\dot\eta_2\left(2\beta-3\dot\eta_1^2\kappa\right)-2\beta\dot\eta_1\left(\delta\eta_1^2+3\delta\eta_2^2-4\right)+\dot\eta_1^3\kappa\left(\delta\eta_1^2+5\delta\eta_2^2-6\right)\right. \tag{2.37}$$
$$\left.+3\dot\eta_2^2\dot\eta_1\kappa\left(\delta\left(\eta_1^2+\eta_2^2\right)-2\right)-2\delta\eta_1\eta_2\dot\eta_2^3\kappa\right)$$

$$f_2(\eta_1,\dot\eta_1,\eta_2,\dot\eta_2) = \frac{1}{8}\left(\delta\dot\eta_2\eta_2^2\left(-2\beta+3{\dot\eta_1}^2\kappa+{\dot\eta_2}^2\kappa\right)-2\delta\dot\eta_1\eta_1\eta_2\left(-2\beta+{\dot\eta_1}^2\kappa+3{\dot\eta_2}^2\kappa\right)\right. \tag{2.38}$$
$$\left.+\dot\eta_2\left(\delta\eta_1^2\left(-6\beta+3{\dot\eta_1}^2\kappa+5{\dot\eta_2}^2\kappa\right)+8\beta-6\left({\dot\eta_1}^2+{\dot\eta_2}^2\right)\kappa\right)\right)$$

For case A, the evaluation of the integrals (2.25,2.26) is difficult. It is necessary to split the integrals into two domains, in which the argument of the absolute value is either positive or negative, and then put together the results afterwards. The boundaries of these domains depend on the argument φ of the complex number $\eta_1 + i\eta_2$. The final result is therefore in terms of φ, and it is too long to be written here. It depends on cosine and sine functions of ϕ and its multiples. It is possible to eliminate the dependence on φ by trigonometrically expanding the terms, and substituting these relations for the sine and cosine of φ:

$$\sin\varphi = \frac{\eta_2}{\sqrt{\eta_1^2+\eta_2^2}} \tag{2.39}$$

$$\cos\varphi = \frac{\eta_1}{\sqrt{\eta_1^2+\eta_2^2}} \tag{2.40}$$

Both cases A and B contain forcing terms that are the same as the ones obtained in Noiray et al. (2011) for $\delta = 0$.

2.11.2 Method of averaging

This appendix shows how to evaluate the terms of (2.35) for case B. It is possible to prove that

$$\langle c_1 f_1 \rangle + i\langle s_1 f_1 \rangle = \frac{1}{2\pi}\int_0^{2\pi} e^{i(t+\varphi_1)} f_1(t)dt \equiv F_1 \tag{2.41}$$

where we did not indicate the explicit dependence of f_1 on A, B, θ as in the definition (2.36) of the averaging operator for conciseness, and we set $\omega = 1$. Then, from F_1 we can evaluate the two terms on the left as real and imaginary parts. We can set $z = e^{it}$, and operate these substitution in F_1:

$$\begin{cases} 2c_1 = \overline{\varphi}_1 z + \frac{1}{\overline{\varphi}_1 z} & 2s_1 = -i(\overline{\varphi}_1 z - \frac{1}{\overline{\varphi}_1 z}) \quad \text{with } \overline{\varphi}_1 \equiv e^{i\varphi_1} \\ 2c_2 = \overline{\varphi}_2 z + \frac{1}{\overline{\varphi}_2 z} & 2s_2 = -i(\overline{\varphi}_2 z - \frac{1}{\overline{\varphi}_2 z}) \quad \text{with } \overline{\varphi}_2 \equiv e^{i\varphi_2} \end{cases} \tag{2.42}$$

We can then change the line integral in F_1 to a contour integral on the unit circle of the complex plane:

$$F_1 = \frac{1}{2\pi}\int_0^{2\pi} e^{i(t+\varphi_1)} f_1(t)dt = \frac{\overline{\varphi}_1}{2\pi}\oint z f_1(z)\frac{dz}{iz} = \frac{\overline{\varphi}_1}{2\pi i}\oint f_1(z)dz \tag{2.43}$$

It can be shown that this function presents a single pole at the origin with no branch cuts, so that

$$F_1 = \frac{\overline{\varphi}_1}{2\pi i} 2\pi i \sum_{|z|<=1} \text{Res}[f_1] = \overline{\varphi}_1 \text{Res}_{z=0}[f_1] \tag{2.44}$$

Notice that the expression for f_1 is long, and the evaluation of the residue requires the use of a computer algebra system. The system of equations of the slow flow are:

$$\begin{aligned} A' =& \frac{1}{128} A\Big[64(\beta-\alpha) - 2B^2\cos(2\phi)\Big(\kappa\left(8A^2\delta + B^2\delta + 6\right) - 10\beta\delta\Big) \\ & - 4\beta\delta\left(A^2 + 6B^2\right) + \kappa\Big(A^4\delta + 18A^2\left(B^2\delta - 2\right) + 3B^2\left(B^2\delta - 8\right)\Big)\Big] \end{aligned} \tag{2.45}$$

$$\begin{aligned} B' =& \frac{1}{128} B\Big[64(\beta-\alpha) - 2A^2\cos(2\phi)\Big(\kappa\left(8B^2\delta + A^2\delta + 6\right) - 10\beta\delta\Big) \\ & - 4\beta\delta\left(B^2 + 6A^2\right) + \kappa\Big(B^4\delta + 18B^2\left(A^2\delta - 2\right) + 3A^2\left(A^2\delta - 8\right)\Big)\Big] \end{aligned} \tag{2.46}$$

$$\phi' = \frac{1}{64}\left(A^2 + B^2\right)\sin(2\phi)\Big[\kappa\Big(\delta\left(A^2 + B^2\right) + 6\Big) - 10\beta\delta\Big] \tag{2.47}$$

Chapter 3

State-space realization of a describing function

This chapter was published as Ghirardo et al. (2015a).

3.1 Abstract

The describing function is a powerful tool for characterising nonlinear dynamical systems in the frequency domain. In some cases, it is the only available description of a nonlinear operator characterising a certain subcomponent of the system. This chapter presents a methodology to provide a state-space realization of one given describing function, in order to allow the study of the system in the time domain as well. The realization is based on Hammerstein models and Fourier–Bessel series. It can be embedded in time domain simulations of complex configurations with many nonlinear elements interacting, accurately describing the nonlinear saturation of the system. The technique is applied to an example application in the field of combustion instability, featuring self-excited thermoacoustic oscillations. We benchmark the performance of the tool comparing the results with a frequency domain analysis of the same system, obtaining good agreement between the two formulations.

3.2 Introduction

Combustion systems are subject to acoustic fluctuations of pressure and velocity, called thermoacoustic oscillations Lieuwen (2012); Lieuwen and Yang (2005). These arise from the interaction between acoustic waves and the unsteady heat release rate from

the flame, which locally induces a gas expansion. Often these systems are not globally stable, and can nonlinearly saturate to a dynamic attractor, which in most cases is a time-periodic acoustic field.

An increasingly large number of experiments (Ćosić et al., 2014; Dowling, 1997; Noiray et al., 2008; Palies et al., 2011; Schimek et al., 2011) and numerical simulations (Armitage et al., 2006; Hemchandra, 2012; Krediet et al., 2012; Tay-Wo-Chong et al., 2012) investigate the nonlinear response of the unsteady heat release rate to sinusoidal acoustic forcing. The same can be done for Helmholtz resonators (Bellucci et al., 2004; Ćosić et al., 2012; Zinn, 1970), which are acoustic damping devices. In particular, both elements (flame and Helmholtz resonator) can be isolated to an open-loop configuration, and forced by a harmonic input at a fixed frequency and amplitude: for the flame, the input is an acoustic longitudinal velocity fluctuation just upstream of the flame; for the resonator, the input is an acoustic pressure fluctuation at the interface between the neck of the resonator and the encasing geometry. Both elements are assumed to be stable, time-invariant operators, so that the output signal has the same period of the input. The response is measured in terms of the gain and as the phase difference between output and input. This is the sinusoidal-input describing function Gelb and Vander Velde (1968) of the element, from here onwards referred to simply as the describing function.

One can then study the element in a closed-loop configuration, which in the case of thermoacoustics corresponds to placing it in an enclosing geometry, which feeds back the output of the element as the input (reflection of acoustic waves). If the system undergoes a Hopf bifurcation, one can then track the stability of the whole system as a function of the amplitude of the limit cycle, by applying harmonic balance truncated at the first harmonic. The technique is succinctly described in Basso et al. (1997), and works quite well as long as the system acts as a low-pass filter on the higher-order harmonics, commonly known as the filtering hypothesis.

Difficulties arise if, for certain parameters, more than one mode of self-sustained oscillation is possible, because the knowledge of the describing function to multiple inputs is then required, as discussed for thermoacoustic systems in Boudy et al. (2013); Moeck and Paschereit (2012).

A second difficulty regards the onset of a secondary bifurcation, often of the Neimark-Sacker type, where two distinct frequencies emerge, as found in experiments by Kabiraj et al. (2012) and in numerical simulations Kashinath et al. (2014). This can still be discussed within the describing function framework Basso et al. (1997); Lanza et al. (2007), but is not considered in this chapter.

A third difficulty arises in the low-order modelling of thermoacoustic oscillations in annular combustors, where the geometric discrete rotational symmetry makes the system's linearised dynamics degenerate: a 2-dimensional eigenspace becomes linearly unstable at a double Hopf bifurcation[1], i.e. two complex conjugate pairs of eigenvalues sharing the same frequency and growth-rate cross the imaginary axis at the same time. To tackle this third difficulty, a state-space formulation of the problem is proposed for annular geometries by Schuermans et al. (2006). One can then study the dynamical system, either with time-integration, numerical-continuation, or analytically with the method of averaging Sanders and Verhulst (2007) or of multiple scales Kevorkian and Cole (1996). The major drawback of these state-space investigations (see also Ghirardo and Juniper (2013); Noiray et al. (2011); Noiray and Schuermans (2013)) is that the description of the flame response in state-space has so far been phenomenological and not quantitative.

Section §3.3 of this chapter presents a quantitative state-space realization of one given describing function, so that it can be used in time domain models of thermoacoustic systems. This modelling tool can improve the industrial design process, by predicting the nonlinear frequency shift of a mode when compared to a linear analysis, and correctly modelling the softening Ćosić et al. (2012) of Helmholtz resonators in the nonlinear regime.

Note that the focus here is not on system identification, because the system is fully described in the frequency domain[2], and time domain input/output data are often not available. Reference Taylor (1983) describes qualitatively the inversion of a describing function, for the purpose of controlling a nonlinear system. Reference Nassirharand (2009) describes an iterative, numerical algorithm to calculate a nonlinear saturation function for a given real-valued describing function. We propose here instead a Fourier–Bessel series decomposition, which allows the calculation of a good fit without requiring iterations. This is based on the analytic evaluation of the describing function of a Fourier–Bessel term, discussed in appendix §3.6.1. This procedure is of general applicability and has good convergence properties in all cases studied (see for example Fig. 3.5). The nonlinear saturation is then used as part of a modified Hammerstein model (Eskinat et al., 1991), pictured in Fig. 3.2.b. This allows us to model the dependence of the phase response on the input amplitude, so that also a

[1] many annular combustors are also slightly not-axisymmetric, perturbing this double-Hopf bifurcation

[2] To be precise the response is defined at discrete values of frequency and amplitude, and then interpolated in between.

complex-valued describing function can be fitted. Section §3.3 discusses how to fit accurately first the linear part of the model and then the nonlinear part.

To show the applicability of this nonlinear state-space realization, we study in section §3.4 an example problem modelling a self-excited thermoacoustic experiment Ćosić et al. (2014), which depends on a geometric parameter L of the configuration (the length of the combustion chamber). We then study the system parametrically in L with two methods.

The first method consists of a first-order harmonic balance method, often described in thermoacoustics as the flame describing function framework Noiray et al. (2008). It predicts the amplitudes and the frequencies of the limit cycles as function of L, as presented in Fig. 3.9.

The second method is the time domain realization of the system, using the state-space realization of the describing function described in section §3.3. We run time domain simulations of the problem and extract the amplitude and the frequency of the dominant harmonic of the signal. One example of simulation is presented in Fig. 3.11.

We then compare the results of the two methods in section §3.4.3, obtaining a good match, and discuss the accuracy of the time domain model.

We finally discuss the applications of this methodology and possible improvements in section §3.5.

3.3 The state-space realization

The describing function represents the response of a nonlinear operator $\mathcal{Q}[u(t)]$ to a sinusoidal input $u(t) = A\cos(\omega t)$. In our application u is the fluctuating velocity measured upstream of the flame, just downstream of the burner, with amplitude A and forcing frequency ω, and the quantity $\mathcal{Q}$ describes the fluctuating heat release rate measured at the flame. This section is, however, general, and applies to a generic single-input single-output (SISO) system. The describing function of the operator $\mathcal{Q}$ is defined Gelb and Vander Velde (1968) as

$$Q(A,\omega) = \frac{1}{A}\frac{1}{\pi/\omega}\int_0^{2\pi/\omega} \mathcal{Q}\left[A\cos(\omega t)\right] \left(\cos(\omega t) + i\sin(\omega t)\right) dt \tag{3.1}$$

As a matter of nomenclature, we will use capital letters to indicate the describing or transfer function of an operator, such as $Q(A,\omega)$, and we will use capital calligraphic letters to describe the corresponding time domain operator, such as $\mathcal{Q}[u(t)]$. The

quantity $Q(A,\omega)$ is a complex number, with its real and imaginary parts expressing the amplitudes of the components of $\mathcal{Q}$ respectively in phase and in quadrature with the sinusoidal input. One can then define the gain G and the phase φ of the flame response as the polar coordinates of the complex number $Q(A,\omega)$:

$$Q(A,\omega) = G(A,\omega)e^{i\varphi(A,\omega)},\ G,\varphi : \mathbb{R}^+ \times \mathbb{R}^+ \mapsto \mathbb{R} \tag{3.2}$$

$$\begin{cases} G(A,\omega) &= |Q(A,\omega)| \\ \varphi(A,\omega) &= \arg[Q(A,\omega)] \end{cases} \tag{3.3}$$

We assume that the function $Q(A,\omega)$ is provided over the range of frequencies and amplitudes of interest, from data coming from experiments, numerical simulations or analytical models. To provide an example of the application of this technique, we apply it to an experiment carried out by Ćosić et al. (2013, 2014). The describing function of the heat release rate response is shown in Fig. 3.1. It has been gently smoothed from experimental data using B-splines Dierckx (1993). In addition, the phase is unwrapped by 2π to present a continuous function $\varphi(A,\omega)$ in the domain.

We want to provide a state space model that is equivalent to the given describing function. Notice that the describing function provides information on how the system behaves if only one fundamental harmonic is present. In the same way, the state space model will be accurate as long as the system presents a strong fundamental harmonic. This restricts the applicability to the describing function framework, and will accurately describe the state of the system if, after the Hopf bifurcation, secondary bifurcations do not occur. The model will be tuned at a design frequency ω_d, at which it will be most accurate. For example, one can choose as design frequency the frequency of the least stable mode of the whole system, obtained from a linear stability analysis. One can then run the time simulation, and let the system evolve to a saturated limit cycle, with a nonlinear saturated frequency $\omega_{d,1} = \omega_d + \Delta\omega$. If $\Delta\omega$ is large, one can tune the flame model to the frequency $\omega_{d,1}$ and either run a second time simulation or continue from the first limit cycle.

Fig. 3.2 shows a sketch in the complex plane of the input and of the output phasors[3] of the describing function, at a fixed design frequency ω_d. The sinusoidal inputs $Ae^{i\omega_d t}$ rotate in time in the anticlockwise direction, for three different amplitudes A, in the top-left quadrant (the other features of the figure are discussed in the next section). The input is operated on by $\mathcal{Q}$ and the subsequent output is shown in the top-right

[3] a phasor is a representation of a sinusoidal function with a certain amplitude, frequency and phase in the complex plane

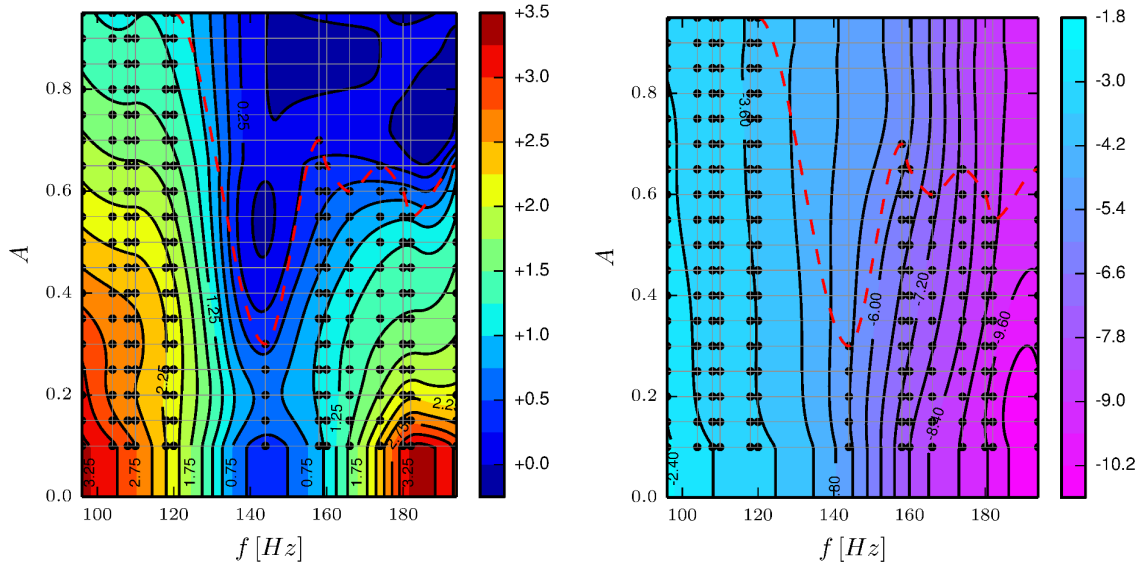

(a) Gain response

(b) Phase response

Fig. 3.1 Smoothed, interpolated experimental data from Ćosić et al. (2013, 2014). The black dots are individual experiments, carried out at a fixed frequency (horizontal axis, in Hz) and forcing velocity amplitude (vertical axis, normalised with respect to the mean upstream velocity). The red dashed line is the curve below which the interpolation is valid, because above it no experimental data is available. At velocity amplitudes below the minimum tested velocity the corresponding value was used (at the bottom of both plots).

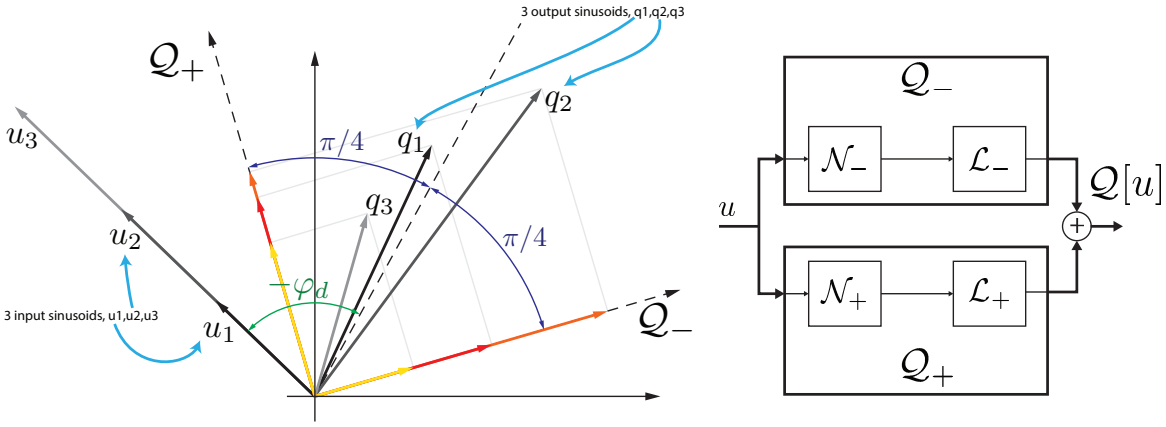

(a) phasor space representation (b) flowchart representation

Fig. 3.2 a) Representation of the input and output phasor of the nonlinear operator in the complex plane at the design frequency ω_d at one instant in time. The three black, grey and light grey arrows in the top-left quadrant represent three input phasors with increasing amplitude. These phasors rotate around the origin in time, with direction $e^{i\omega_d t}$. The output phasors are represented with the three grayscale thick arrows in the top-right quadrant. The gain and the phase of the output depend on the input amplitude, e.g. the three thick phasors in the top-right quadrant are not parallel. The mean phase response $\overline{\varphi}_d$ of the outputs subtends the arc. The two nonlinear operators $Q_\pm$ are designed so that their phase response is $\pm\pi/4$ the mean phase response $\overline{\varphi}_d$. The two dashed black arrows are the directions of the two operators. The output phasor is then calculated as the sum of its projections onto the two operators. The projections at the 3 amplitudes are the red, orange and yellow arrows. b) block diagram of the model. The internal structure of each of the operators $\mathcal{Q}_\pm$ is a Hammerstein model, discussed in section §3.3.1

quadrant. Since $\mathcal{Q}$ is a fully nonlinear operator, the phase and the gain responses depend on the amplitude A, and the three output phasors are not parallel, nor is the ratio of their moduli with the respective input moduli constant.

In subsection §3.3.1 and §3.3.2 we choose the structure of the state-space realization. The following subsections §3.3.3 and §3.3.4 carry out the fitting of respectively the linear and nonlinear elements that define the realization. Subsection §3.3.5 briefly summarises this section.

3.3.1 Operator splitting

We decompose the heat release rate response as the sum of two nonlinear operators, as represented in Fig. 3.2.b

$$\mathcal{Q}[u(t)] = \mathcal{Q}_-[u(t)] + \mathcal{Q}_+[u(t)] \tag{3.4}$$

$$\begin{cases} Q_-(A,\omega) = & G_-(A,\omega)e^{i\varphi_-(A,\omega_d)} \\ Q_+(A,\omega) = & G_+(A,\omega)e^{i\varphi_+(A,\omega_d)} \end{cases} \tag{3.5}$$

The reasoning behind this choice is that the two operators $\mathcal{Q}_-$ and $\mathcal{Q}_+$ will be designed to have a constant phase response with amplitude. This feature will allow us to model each of them as a Hammerstein block in section §3.3.2. The frequency ω_d in (3.5) is the frequency at which the time domain realization will be most accurate. We design the two operators to have phase responses that differ by $\pi/2$, as can be observed in Fig. 3.2.a where their phase responses (dashed black arrows) are orthogonal. Their phase response is defined as:

$$\begin{cases} \varphi_-(A,\omega) & \equiv \varphi(A,\omega) - \varphi(A,\omega_d) + \overline{\varphi}_d - \pi/4 \\ \varphi_+(A,\omega) & \equiv \varphi(A,\omega) - \varphi(A,\omega_d) + \overline{\varphi}_d + \pi/4 \end{cases} \tag{3.6}$$

From the definition (3.6) the output signals of the 2 operators are always in quadrature, and they are defined so that at the design frequency ω_d they present the phases

$$\varphi_-(A,\omega_d) = \overline{\varphi}_d - \pi/4 \tag{3.7a}$$

$$\varphi_+(A,\omega_d) = \overline{\varphi}_d + \pi/4 \tag{3.7b}$$

The design phase $\overline{\varphi}_d$ is the green (negative) angle between the input (vectors in the top-left quadrant) and the dashed line in the top-right quadrant in Fig. 3.2. The value of $\overline{\varphi}_d$ is quite arbitrary, though in most cases it is chosen as the mean phase response with amplitude of the operator $\mathcal{Q}$ at the design frequency ω_d; secondary considerations on the limitations of this choice are discussed at the end of section §3.3.3. The two operators have then a phase response that is shifted by $\pm\pi/4$ with respect to that dashed line, as defined in (3.6). Once $\overline{\varphi}_d$ is fixed, the phase response of the two operators is also fixed by (3.6), and the two gains $G_\mp(A,\omega)$ can be calculated from (3.4). In other words, the original operator $\mathcal{Q}$ is rewritten as the sum of its two projections on these two directions. The projections are shown in Fig. 3.2 with red, orange, yellow colours.

3.3.2 Nonlinear saturation

This subsection applies in the same way to each of the operators $\mathcal{Q}_-$ and $\mathcal{Q}_+$. For ease of notation, we drop the subscript $\pm$ here. We express each of the operators $\mathcal{Q}$ as the composition of a linear operator $\mathcal{L}$ and a nonlinear operator $\mathcal{N}$, as presented in Fig. 3.2.b. We choose as linear operator the linearisation of $\mathcal{Q}$:

$$L(\omega) \equiv Q(0, \omega) \tag{3.8}$$

In (3.8), L is a transfer function, since it does not depend on the amplitude by definition. The composition of $\mathcal{L}$ and $\mathcal{N}$ can happen in two ways Gómez and Baeyens (2004):

$$\text{Wiener model} \qquad \mathcal{Q} = \mathcal{N}\Big[\mathcal{L}[u(t)]\Big] \tag{3.9a}$$

$$\text{Hammerstein model} \qquad \mathcal{Q} = \mathcal{L}\Big[\mathcal{N}[u(t)]\Big] \tag{3.9b}$$

We now briefly discuss which model is best suited for the problem at hand. The two options lead to a different expression for the describing function N:

$$\text{Wiener} \qquad N_{NL}(A, \omega) = Q\Big(\frac{A}{|Q(0, \omega)|}, \omega\Big)/Q(0, \omega)$$

$$\text{Hammerstein} \qquad N_{LN}(A, \omega) = Q(A, \omega)/Q(0, \omega)$$

We present in Fig. 3.3 the gains of N_{NL} and N_{LN} applied to the full operator Q introduced in (3.1) (the same considerations apply when considering Q_- and Q_+). Because of (3.8), the gains are unity at zero amplitude A, as discussed in Eskinat et al. (1991). Each curve represents the nonlinear saturation with the amplitude A of the input at a fixed frequency, with the colour of the line indicating the frequency value. We observe that in the case 3.3.b the nonlinear saturation curves have a weak dependence on the frequency, and tend to overlap better, especially at large amplitudes. This happens because the dominant factor of the nonlinear saturation is the amplitude of forcing, and not the amplitude of the linear response. This is a feature of forced flames, where one leading nondimensional number governing the saturation is the ratio $A/\overline{U}$, with $\overline{U}$ the bulk velocity at the burner inlet.

We must also take into account that the nonlinear operator $\mathcal{N}$ produces, as output, spurious odd harmonics of the input frequency. These harmonics do not hold any meaning, and can be filtered out with the structure (3.9b) if $\mathcal{L}$ behaves like a low-pass filter outside the range of frequencies studied. This is a feature of flames (Schuller et al., 2003) and a necessity for the model to work, as we want to comply with the

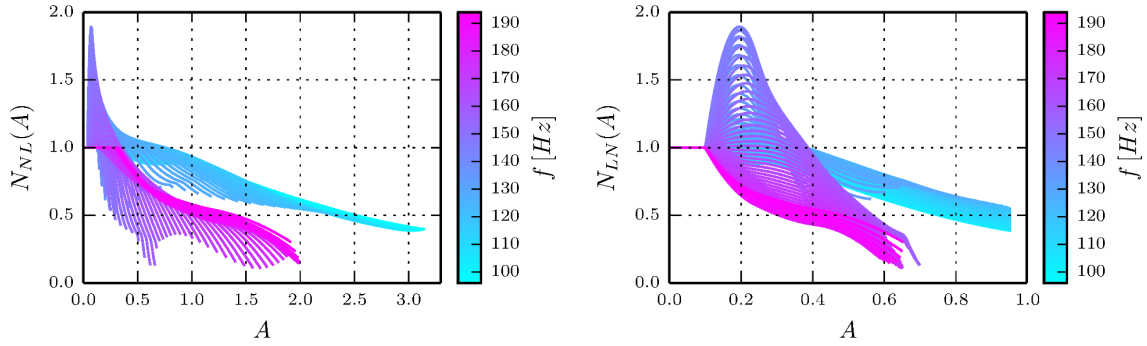

(a) Nonlin. sat. of the Wiener model (b) Nonlin. sat. of the Hammerstein model

Fig. 3.3 Slices of the nonlinear gain $G(A, \omega)$ at 100 frequencies, equispaced from 96 Hz to 194 Hz. Each line corresponds to a different frequency, associated to a different colour on the colour bar on the right. In (a) the gain of the operator $\mathcal{N}$ is applied after the operator $\mathcal{L}$ as in (3.9a), and this results in larger amplitudes A. In (b) the operator $\mathcal{N}$ is applied before the operator $\mathcal{L}$ as in (3.9b). Two main behaviours are found around two distinct frequencies, corresponding to the two hills in the describing function of Fig. 3.1 around 100 Hz and around 190 Hz. The saturation curves are closer in (b).

hypothesis of strong attenuation of higher harmonics that characterizes the describing function framework. We therefore opt for the Hammerstein model described by (3.9b).

We now exploit the weak dependence of the gain of N on the frequency, and choose for N a static, i.e. memory-less, nonlinearity. By operating in this way, the linear operator $\mathcal{L}$ depends only on the frequency, and the nonlinear operator $\mathcal{N}$ depends only on the amplitude:

$$\mathcal{Q} = \mathcal{L}\Big[\mathcal{N}[u(t)]\Big] \qquad Q(A, \omega) = N(A)L(\omega) \tag{3.10}$$

In the frequency domain, we are then approximating

$$Q(A, \omega) \approx N_-(A)L_-(\omega) + N_+(A)L_+(\omega) \tag{3.11}$$

and we will make this approximation accurate at the design frequency ω_d. Section §3.3.3 discusses how to calculate the linear operators $\mathcal{L}_\pm$, and section §3.3.4 discusses how to calculate the nonlinear operators $\mathcal{N}_\pm$.

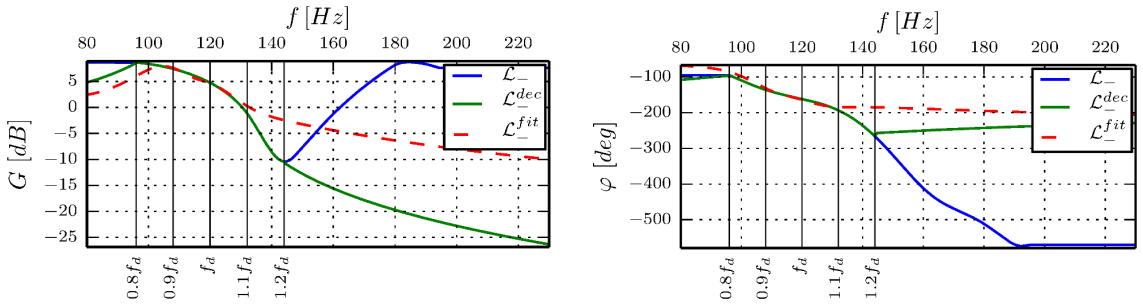

(a) Gain response

(b) Phase response

Fig. 3.4 Fitting at f_d =120 Hz of the linear operator $\mathcal{L}_-$. The gain is decreased outside the range $[0.8\omega_d, 1.2\omega_d]$. The fit is then weighted higher in the range $[0.9\omega_d, 1.1\omega_d]$, where the fit is more accurate.

3.3.3 Linear operator fitting

We want to calculate a fit for the linear operator $\mathcal{L}$, whose frequency response along the imaginary axis $s = i\omega$ is defined by equation (3.8). We choose to fit this curve with rational function approximations, as discussed by Gustavsen (2006); Gustavsen and Semlyen (1999). In particular, the transfer function of the operator is fitted to

$$\mathcal{L}^{\text{fit}}(s) = \sum_{n=1}^{N} \frac{c_n}{s - a_n} + d \ , \qquad s = \sigma + i\omega \tag{3.12}$$

where $\{c_n, a_n\}$ and d are the coefficients of the fit, which were calculated using the package VFIT3 written by Gustavsen (2006). This is quite an established technique, used for example in Kurokawa et al. (2009) to run time domain simulation of a linear system, and in Bothien et al. (2007) to identify and simulate components of acoustic and thermoacoustic systems. In this case, we enforce the stability of the linear operator, but do not enforce a passivity constraint Gustavsen (2008).

The tool VFIT3 also calculates the matrices A, B, C, D that describe the state-space realization of (3.12):

$$\dot{x} = Ax + Bu \tag{3.13a}$$

$$y = Cx + Du \tag{3.13b}$$

where x is a vector variable describing the internal state, and u and y are respectively the scalar input and output of the linear operator.

An important parameter of the fitting is the number N of poles in (3.12). A large number N usually leads to smaller errors within the range of frequencies $[\omega_1, \omega_2]$ at which data is available. On the other hand, a large N usually results in a fit with many poles a_n outside the range $[\omega_1, \omega_2]$. These in turn lead to large, unphysical gains outside of the range of frequencies $[\omega_1, \omega_2]$ studied, violating our requirement of a low-pass filter behaviour at the higher frequencies. This is often referred to as overfitting (Gustavsen and Heitz, 2008), and if overlooked can lead to strongly oscillating time domain simulations at very high frequencies.

Because of these considerations and after some testing, we choose a number of $N = 8$ poles to do the fitting. We observe that we need: *1)* a low-pass filter behaviour at the frequencies of the higher order harmonics, i.e. at $(2k+1)\omega_d$, $k \in \mathbb{N}_{>0}$, as discussed in section §3.3.2; *2)* an accurate fit only in the vicinity of the design frequency ω_d;

To satisfy the first constraint, we extend the fit to a broader range of frequencies, from 30 Hz to 776 Hz. Moreover, outside the range $[0.8\omega_d, 1.2\omega_d]$ we make the gain decrease towards zero. This guarantees that the fit will be well behaved outside the range of frequencies of interest, i.e. it will not exhibit unexpected large gains due to overfitting.

To satisfy the second constraint, we provide to the fitting tool VFIT3 a vector of weights, which we choose larger in the range $[0.9\omega_d, 1.1\omega_d]$ to improve the accuracy in a neighbourhood of ω_d.

We present an example of the fitting in Fig. 3.4, where the original response $\mathcal{L}$, the decreased response $\mathcal{L}^{\text{dec}}$ and the fitted operator $\mathcal{L}^{\text{fit}}$ are reported. Notice that the fit is accurate only in the vicinity of the design frequency f_d.

The two linear operators $\mathcal{L}_\pm$ are fitted to the linearisation (3.8) of $Q_\pm$, which are defined in (3.5). Since this is a fitting algorithm, the fitted operators $\mathcal{L}_\pm^{\text{fit}}$ are affected by error, and the equation (3.8) holds only in an approximate sense. In particular, also the phase responses $\varphi_\pm^{\text{fit}}$ are not exactly in quadrature, with equations (3.7) valid only in an approximate sense. We can however take this into account and calculate the nonlinear saturations $\mathcal{N}_\pm$ as the projections of the original operator Q on these slightly non-orthonormal operators, as discussed in section §3.3.4.

The design phase

This paragraph discusses a technicality regarding the choice of the design phase $\overline{\varphi}_d$. We observe that the value of $L_\pm(\omega_d)$ depends both on the linear gain $G(0, \omega)$ and on the phase response $\overline{\varphi}_d$ of $Q_\pm$. A geometric interpretation is immediate in Fig. 3.2. For

example, if the linear response (black vector, top-right quadrant) is very close to the direction of Q_-, then its projection on Q_+ will be small, and the gain of L_+ will be small as well from (3.8). This situation can lead to a very small linear gain and a very steep nonlinear response; in the worst case, if $L_+(\omega) = 0$ the model would be flawed, as the nonlinear response $N[L[u]]$ would be zero not just in the linear regime but at all amplitudes. We can avoid these situations by choosing an appropriate value for $\overline{\varphi}_d$. Among the many possibilities, we choose to first calculate the design phase as $\overline{\varphi}_d = \overline{\varphi(\omega_d, A)}$, averaged over the possible forcing amplitudes A at the design frequency. Geometrically, it represents the orientation of the dashed line that best represents the average orientation of the output vectors in the top-right quadrant of Fig. 3.2. If such a line is then too close to the direction of one of the operators $Q_\pm$, i.e. if $|\overline{\varphi}_d \pm \pi/4 - \varphi(\omega_d, 0)| < \pi/8$, we suitably add or subtract to it an angle $\pi/8$.

3.3.4 Nonlinear operator fitting

We fitted in the previous section the linear operators $\mathcal{L}_\pm^{\text{fit}}$ of the two Hammerstein models $Q_\pm$. In this section we fit the nonlinear operators $\mathcal{N}_\pm$, which are defined in the frequency domain by the approximation (3.11). We now treat it as an equality at the design frequency ω_d:

$$Q(A, \omega_d) = N_-(A)L_-^{\text{fit}}(\omega_d) + N_+(A)L_+^{\text{fit}}(\omega_d) \tag{3.14}$$

Both sides of (3.14) are complex valued, and $L_+^{\text{fit}}(\omega_d)$ and $L_-^{\text{fit}}(\omega_d)$ are linearly independent phasors[4]. We then operate a vector projection in the complex plane of $Q(A, \omega_d)$ on the base composed of the two phasors, $\{L_+^{\text{fit}}(\omega_d)\ , L_-^{\text{fit}}(\omega_d)\}$. To do so, we use the scalar product

$$\langle a, b\rangle \equiv \Big[\text{Re}(a)\text{Re}(b) + \text{Im}(a)\text{Im}(b)\Big]\Big|_{\omega=\omega_d} \tag{3.15}$$

and the norm as $|a|^2 \equiv \langle a, a\rangle$. With this structure, for each value of A, the quantities $N_\pm(A)$ are the projections of $Q(A, \omega_d)$ on the two phasors:

$$\begin{bmatrix} N_+(A) \\ N_-(A) \end{bmatrix} = \frac{1}{|L_-^{\text{fit}}|^2|L_+^{\text{fit}}|^2 - \langle L_-^{\text{fit}}, L_+^{\text{fit}}\rangle^2} \cdot \\ \cdot \begin{bmatrix} |L_-^{\text{fit}}|^2, & -\langle L_-^{\text{fit}}, L_+^{\text{fit}}\rangle \\ -\langle L_-^{\text{fit}}, L_+^{\text{fit}}\rangle, & |L_+^{\text{fit}}|^2 \end{bmatrix} \begin{bmatrix} \langle Q(A, \omega_d), L_+^{\text{fit}}\rangle \\ \langle Q(A, \omega_d), L_-^{\text{fit}}\rangle \end{bmatrix} \tag{3.16}$$

[4] because they are approximately in quadrature

Equation (3.16) can be obtained by applying the scalar product (3.15) between both sides of (3.14) and the two phasors one at a time, and inverting the resulting system of equations. Now the two nonlinear operators $\mathcal{N}_\pm$ are defined in the frequency domain by the two real-valued describing functions $N_\pm(A)$ evaluated in (3.16). In this section we show how to calculate the memory-less state-space realization $\mathcal{N}[u(t)]$ of a sinusoidal input, real-valued describing function $N(A)$. The novelty proposed here is in using a Fourier–Bessel expansion, which leads to good convergence properties, without the use of iterative algorithms as proposed in Nassirharand (2009). We want to choose a convenient analytical structure for $\mathcal{N}$ that is able to survive the evaluation of temporal averaging that defines the describing function in equation (3.1). We propose the following analytical structure for $\mathcal{N}(u)$:

$$\mathcal{N}(u) \approx q^{erf}_{\mu,\kappa}(u) + \sum_{n=1}^{N_b} c_n J_1(\hat{u}_n u) \tag{3.17}$$

for a suitable choice of the parameters μ, κ and of the coefficients c_n. The first term in (3.17) is a modified error function, defined as:

$$q^{erf}_{\mu,\kappa}(u) \equiv \kappa \mathrm{erf}\left[\frac{\sqrt{\pi}\mu u}{2\kappa}\right] \ , \ \mathrm{erf}(x) \equiv \frac{2}{\sqrt{\pi}}\int_0^x e^{-t^2} dt \tag{3.18}$$

The function (3.18) is constructed in a way that the linear gain is μ and the output saturates at κ:

$$\frac{\partial q^{erf}_{\mu,\kappa}(u)}{\partial u}\Big|_{u=0} = \mu \qquad \lim_{u\to\pm\infty} q^{erf}_{\mu,\kappa}(u) = \pm\kappa \tag{3.19}$$

The second term in (3.17) is a Fourier–Bessel series. The function $J_k(x)$ is the Bessel function of the first kind of order k, and

$$\hat{u}_n = \frac{\tilde{u}_n}{W}, \tag{3.20}$$

where $\tilde{u}_n$ is the n-th root of $J_1(x) = 0$, with $\tilde{u}_1$ being the smallest non-zero root, and W is a scaling factor. The first derivative of (3.17) at the origin is

$$\beta \equiv \mu + \lim_{u\to 0} \frac{\partial}{\partial u}\left[\sum_{j=1}^{N_b} c_n J_1(\hat{u}_n u)\right] = \mu + \frac{1}{2}\sum_{n=1}^{N_b} c_n \hat{u}_n \tag{3.21}$$

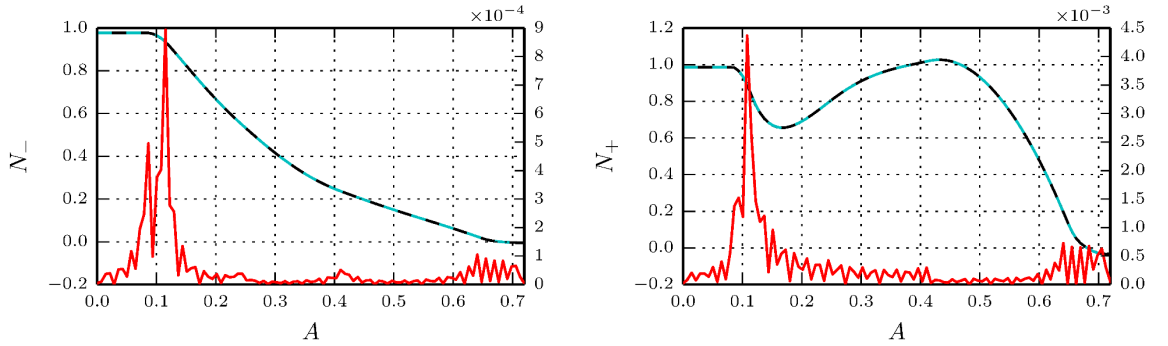

(a) Operator N_-, saturating the input for L_- (b) Operator N_+, saturating the input for L_+

Fig. 3.5 Fitting of the two real-valued describing functions $N_-(A)$ and $N_+(A)$ at $f_l = 180\,\text{Hz}$, with $N = 40$ terms in the Fourier–Bessel series. The original functions and their fit are reported respectively with a continuous black line and a dashed cyan line. They are barely distinguishable by eye, and their value is reported on the left vertical axis of each figure. The absolute value of their difference is reported in red, and refers to the vertical axis on the right.

The expansion (3.17) admits an analytical solution of the integral (3.1):

$$N(A) = \mu e^{-k^2A^2}\left[I_0(k^2A^2) + I_1(k^2A^2)\right] + 2\sum_{n=1}^{N_b}\frac{c_n}{A}J_0\left(\frac{\hat{u}_nA}{2}\right)J_1\left(\frac{\hat{u}_nA}{2}\right) \tag{3.22}$$

where $k \equiv \sqrt{\frac{\pi}{8}}\frac{\mu}{\kappa}$ and $I_k(x)$ is the modified Bessel function of the first kind of order k. Compared with a polynomial, this this series expansion has the advantage that it converges better far from the origin. The proof of the identity (3.22) is reported in the appendix §3.6.1. One can then fit the coefficients $\mu, \kappa, W, \{c_n\}$ to best approximate the known function on the LHS. First we choose to fit the modified error function term to minimise its distance to $N(A)$, obtaining the value of k and μ. Then the remaining terms are non-orthogonal functions. For a fixed value of W, the fitting of a function on a non-orthonormal base is explained in Klink and Payne (1976). We then look for the optimal value of the scaling factor W leading to the best fit. One fitting with 40 terms of the Fourier–Bessel series is presented in Fig. 3.5, with the error reported in red on the right vertical axis. Since at small amplitudes no experimental data is available (as discussed in Fig. 3.1) the operator has a plateau close to the origin. To reduce the fitting error at the the end of the plateau where the first derivative is discontinuous, we locally apply a moving average filter around the kink before proceeding with the fitting.

The proposed analytical structure (3.17) has proved effective at fitting all the describing functions of the example application, with an accuracy as good as the one presented in Fig. 3.5, with usually 20 terms being sufficient to provide a good fit. The fitting presented in this subsection can be successfully used whenever one needs to accurately represent in state-space a real-valued smooth sinusoidal describing function.

3.3.5 The final state-space realization

This section collects the results of the previous subsections. The two linear operators $\mathcal{L}_\pm$ admit the state-space realization (3.13):

$$\begin{cases} \dot{x}_\pm(t) &= A_\pm x_\pm(t) + B_\pm u_{L\pm}(t) \\ \mathcal{Q}_\pm(t) &= C_\pm x_\pm(t) + D_\pm u_{L\pm}(t) \end{cases} \tag{3.23}$$

where $u_{L\pm}$ are the inputs of the two linear operators. The matrices describing this linear system were calculated in subsection §3.3.3. From equation (3.9b), these inputs are saturated by the nonlinear memory-less functions $\mathcal{N}_\pm$:

$$u_{L\pm} = \mathcal{N}_\pm[u(t)] \tag{3.24}$$

where u is the input of the final operator. The two nonlinear saturations $\mathcal{N}_\pm$ have the analytical structure (3.17), and the coefficients describing them were calculated in subsection §3.3.4. We can then put the two equations (3.23) and (3.24) together and obtain

$$\begin{cases} \dot{x}_\pm(t) &= A_\pm x_\pm(t) + B_\pm \mathcal{N}_\pm[u(t)] \\ \mathcal{Q}_\pm(t) &= C_\pm x_\pm(t) + D_\pm \mathcal{N}_\pm[u(t)] \end{cases} \tag{3.25a}$$

The final output is then given by (3.4):

$$\mathcal{Q}[u(t)] = \mathcal{Q}_-[u(t)] + \mathcal{Q}_+[u(t)] \tag{3.25b}$$

Equations (3.25) fully describe the nonlinear state-space realization, and the internal state of the operator is $\{x_+, x_-\}$. This subsection concludes the description of the nonlinear state-space realization, which will be used in section §3.4.2 in the example application in the time domain.

3.4 Application

This section presents an application example of the state-space realization. The example consists of a self-excited system, schematically represented in Fig. 3.6, where only one nonlinear operator Q is present.

In section §3.4.1 we study the system in the frequency domain with the harmonic balance method. In section §3.4.2 we study it in the time domain with the state-space realization of the describing function introduced in section §3.3. We compare the results obtained with the two techniques in §3.4.3.

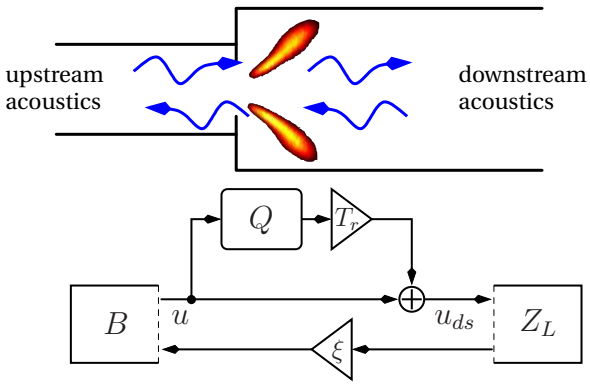

Fig. 3.6 Sketch of the experiment. B and Z_L are linear time-invariant operators, with L being the length of the downstream duct, which can be changed. $\xi \equiv (\rho c)_{ds}/(\rho c)_{us}$ and $T_r \equiv T_{ds}/T_{us}$ are multiplicative factors, and $Q(A, \omega)$ is the nonlinear operator considered in section §3.3. This image was provided by Jonas Moeck from TU Berlin for the article Ghirardo et al. (2015a).

We describe briefly the physics of the application example in the rest of this part, and later solve the problem in subsection §3.4.1 and §3.4.2.

We model the experiment of Ćosić et al. (2013, 2014) of a confined, turbulent, partially premixed swirling flame. The experiment consists schematically of three parts: *1)* the configuration upstream of the flame, which includes the burner and the swirler; *2)* the flame, assumed to be compact when compared to the length of the experiment; *3)* the exhaust gas tube of variable length L.

Since the focus of this chapter is on the nonlinear flame model, we do not describe in detail the configuration of the experiment, which can be found in Ćosić et al. (2013, 2014). The configuration upstream of the flame is fixed, and its acoustic response is governed in the frequency domain by the admittance B:

$$\hat{u} = B(\omega)\frac{\hat{p}}{(\rho c)_{us}} \tag{3.26}$$

where (ρc) is the characteristic impedance of the gas, i.e. the product of density and speed of sound, the latter being a function of temperature. Here and in the following, we indicate with a hat variables that depend on frequency, e.g. $\hat{u} = \hat{u}(\omega)$, and we will drop the hat to discuss time domain variables, such as $u = u(t)$. The variables $\hat{p}$ and $\hat{u}$ in (3.26) are measured just upstream of the flame surface and refer to acoustic pressure and velocity. We avoid adding the subscript us to both quantities so as not to burden the notation in the previous sections, where u can be interpreted more generally as the input of a generic nonlinear operator $\mathcal{Q}$, in contexts different from this application. We also assume that the flame is compact in space, i.e. it is an interface between the upstream and downstream geometry. In a similar manner, the acoustics downstream of the flame are described by the impedance Z_L:

$$\frac{\hat{p}_{ds}}{(\rho c)_{ds}} = Z_L(\omega)\hat{u}_{ds} \tag{3.27}$$

This impedance depends parametrically on the length L of the downstream duct, which can be varied. At the flame interface, under the assumption of a low Mach number flow, the pressure is continuous across the flame interface Lieuwen (2003), i.e. $\hat{p} = \hat{p}_{ds}$, which we rewrite as:

$$\frac{\hat{p}}{(\rho c)_{us}} = \frac{(\rho c)_{ds}}{(\rho c)_{us}} \frac{\hat{p}_{ds}}{(\rho c)_{ds}} \quad , \quad \frac{(\rho c)_{ds}}{(\rho c)_{us}} \approx 0.48 \tag{3.28a}$$

At the flame interface the fluctuating heat release rate induces a sudden expansion of the gas:

$$\hat{u}_{ds} = \left[1 + \left(T_{ds}/T_{us} - 1\right) Q\left(A, \omega\right)\right] \hat{u} \tag{3.28b}$$

The degree of this expansion depends on the ratio $T_{ds}/T_{us} \approx 4.27$ of the temperatures in Kelvin degrees downstream and upstream of the flame, and on the sensitivity of the fluctuating heat release rate on acoustic forcing, described by the describing function Q, which depends on the amplitude A of the upstream velocity fluctuation, with $u(t) = A\cos(\omega t)$. Equation (3.28b) can be derived from Schuermans et al. (1999) imposing the continuity of the pressure at the surface.

All quantities describing the problem have either been directly measured or estimated in Ćosić et al. (2013, 2014).

3.4.1 Frequency domain

This section evaluates the amplitude and the frequency of the limit cycles of the example problem using the harmonic balance method. Combining the equations (3.26,3.27,3.28) we obtain this dispersion relation in ω:

$$B(\omega)\frac{(\rho c)_{ds}}{(\rho c)_{us}}Z_L(\omega)\left[1+\left(T_{ds}/T_{us}-1\right)Q\left(A,\omega\right)\right]=1$$

The relation is parametric in the length L of the combustion chamber. For the acoustic operators B and Z_L we fit a rational function approximation as described in section §3.3.3, but with a number of poles $N = 12$. The rational function can then be evaluated at arbitrary values of $s = \sigma + i\omega$. On the other hand, we assume that the flame response Q is independent of the growth-rate σ, and extrude the value from the imaginary axis, calculating it according to $Q(A, \mathrm{Im}[s] = \omega)$. This leads to the dispersion relation

$$\mathcal{H}_L[\sigma,\omega,A]=0 \tag{3.29}$$

where

$$\begin{aligned}\mathcal{H}_L[\sigma,\omega,A] =&\mathcal{H}_L[s,A]\equiv T_L^{\mathrm{fit}}(\sigma+i\omega)\cdot\\ &\cdot\left[1+\left(T_{ds}/T_{us}-1\right)Q\left(A,\omega\right)\right]-1 \qquad (3.30)\\ T_L^{\mathrm{fit}}(s)\equiv&B^{\mathrm{fit}}(s)\frac{(\rho c)_{ds}}{(\rho c)_{us}}Z_L^{\mathrm{fit}}(s) \qquad (3.31)\end{aligned}$$

Equation (3.29) is a nonlinear eigenvalue problem in the complex Laplacian variable $s = \sigma + i\omega$.

3.4.1.1 Linear stability analysis

In the linear regime, the amplitude A is zero and we study the solutions of the problem $\mathcal{H}_L[\sigma, \omega, 0] = 0$. For each length L, the absolute value of $\mathcal{H}_L$ is calculated in a regular fine grid $\{\sigma_m, \omega_n\}$ in the range of interest, as reported for $L = 0.8$ in Fig. 3.7. A numerical search of the zeros of the equation is then started from the local minima of the map. These zeros are the linear eigenvalues of the problem, reported for all lengths in Fig. 3.8 in terms of growth-rates and frequencies.

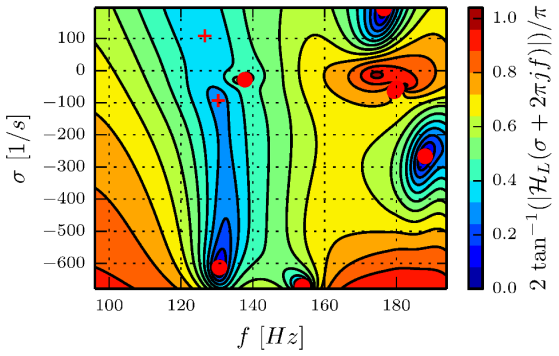

Fig. 3.7 absolute value of the LHS of the dispersion relation (3.29) describing the problem for L =0.8 m. Local minima are reported with red crosses, and solutions with red circles. Only the portion of the domain presenting solutions is shown. The value is rescaled with the arctangent function to present a finite codomain [0 , 1] for representation purposes.

3.4.1.2 Nonlinear stability analysis

In this section we discuss the existence and stability of limit cycles in the system. Limit cycles are found with $\mathcal{H}_L[0, \omega, A] = 0$ because they represent periodic oscillations with zero growth rate. We numerically search for them in a similar manner to the previous section, obtaining solutions (ω_j, A_j). We then numerically perturb the amplitude of oscillation to $A_j + \delta A$ and calculate the resulting perturbed eigenvalue $\delta\sigma + i(\omega_j + \delta\omega_j)$. We then apply Loeb's criterion Gelb and Vander Velde (1968), and infer that the solution is stable/unstable if $\delta\sigma_j/\delta A \lessgtr 0$, assuming that only one frequency of oscillation is present in the system. We carry out the same analysis for all lengths L of the downstream duct, and report the amplitude and the frequency of the stable/unstable limit cycles with filled/empty circles in Fig. 3.9. There is a region with multiple solutions, for L between 0.99 and 1.02 m, one approximately at 160 Hz and the other approximately at 130 Hz.

A first observation regards the points at $L = 0.99$, 1.00 m, where two distinct limit cycles approximately at 160 Hz and at 130 Hz coexist. In this scenario it is impossible to discuss the stability of the two modes without a dual-input describing function, which is not available. Loeb's criterion can be used only to provide sufficient conditions for instability.

We then focus on the mode around 130 Hz. We fix in particular L =1.00 m, with the other lengths in the region presenting a similar behaviour. We study the eigenvalues of the problem as a function of the amplitude of oscillation in Fig. 3.10. At a fixed length L in this region, there is one stable and one unstable limit cycles, at approximately the

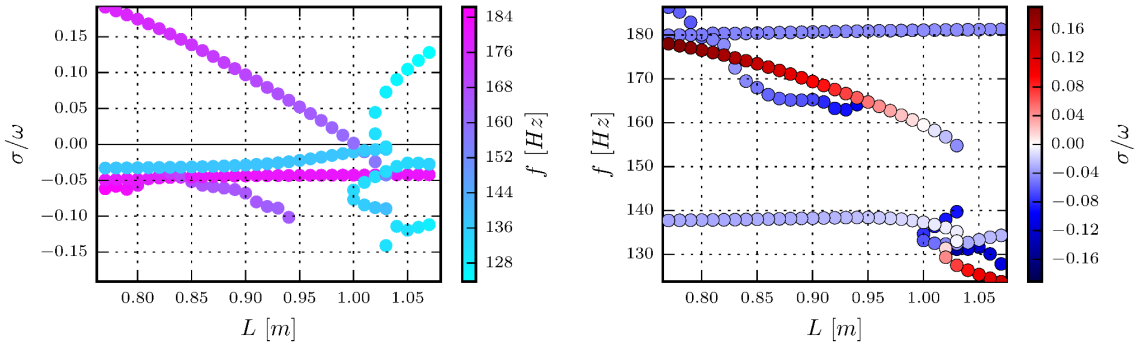

(a) Nondimensional growth-rate

(b) Frequency of oscillation

Fig. 3.8 Eigenvalues of the linear problem for all the lengths L of the downstream duct. The two plots represent the same data, using two distinct vertical axes and colormaps. In a), the height of the circles represents the growth-rate σ and the colour the frequency f of oscillation. In b), the height represents the frequency, and the colour the growth-rate. Eigenvalues with large negative growth-rate are not visible on the plot.

same frequency. This differs from a subcritical Hopf bifurcation, because the stable limit cycle has a smaller amplitude of oscillation than the unstable limit cycle. We also observe that if the system starts at the unstable limit cycle, it is attracted towards a higher amplitude of oscillation, until the eigenvalue disappears. It is then harder to make a definitive discussion of the nonlinear, saturated state of the system in this region. We however notice how the overall shape of the unstable mode in Fig. 3.10.a resembles a subcritical-Hopf bifurcation. The time domain analysis of the system will suggest the same behaviour.

The results from the frequency domain analysis are for the most part consistent with the experiments (Ćosić et al., 2014). However, not all of the features from the present analysis could be observed in the experiment, in particular for those conditions where the analysis predicts multiple limit-cycles.

3.4.2 Time domain

This section evaluates the amplitude and the frequency of the limit cycles of the example problem running time domain simulations. We first combine equations (3.26,3.27,3.28a)

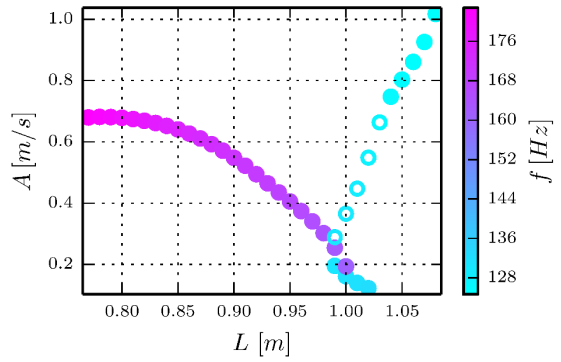

(a) limit cycle amplitude of oscillation

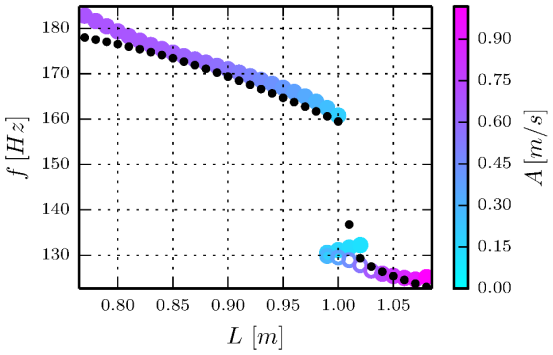

(b) Frequency of oscillation

Fig. 3.9 Nonlinear stability analysis, for all the lengths L of the downstream duct. The two plots represent the same data: in a), the height of the circles represents the limit cycle amplitude A, and the colour the frequency f of oscillation; in b), the height represents the frequency, and the colour the limit cycle amplitude A. Stable/unstable limit cycles are represented with filled/empty circles.

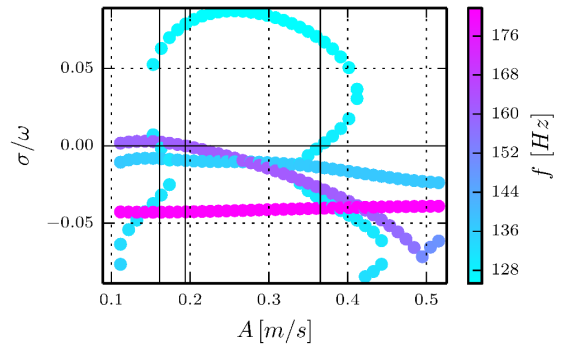

(a) Nondimensional growth-rate

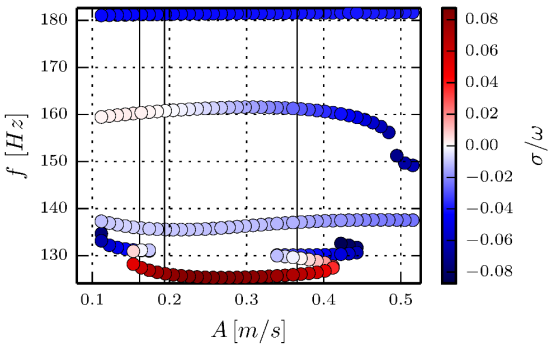

(b) Frequency of oscillation

Fig. 3.10 Eigenvalues of the nonlinear problem for a fixed length L =1 m of the downstream duct, at discrete, equispaced amplitudes of oscillation A. The two plots represent the same data, using two distinct vertical axis and colormaps. In a), the height of the circles represents the growth-rate σ and the colour the frequency f of oscillation. In b), the height represents the frequency, and the colour the growth-rate. Eigenvalues with large negative growth-rate are not visible on the plot. The vertical black lines mark the amplitudes of the limit cycles, at which one growth-rate changes sign in a).

and repeat (3.28b):

$$\hat{u} = B(\omega)\frac{(\rho c)_{ds}}{(\rho c)_{us}} Z_L(\omega)\hat{u}_{ds} \equiv T_L^{\text{fit}}(\omega)\hat{u}_{ds} \tag{3.32a}$$

$$\hat{u}_{ds} = \hat{u} + (T_{ds}/T_{us} - 1)\, Q\,(A, \omega)\, \hat{u} \tag{3.32b}$$

The operator $T_L^{\text{fit}}(\omega)$ was introduced in equation (3.31), and we use here its state-space representation

$$\begin{cases} \dot{x}_T(t) &= A_L x_T(t) + B_L u_{ds}(t) \\ u(t) &= C_L x_T(t) \end{cases} \tag{3.33a}$$

We instructed the tool VFIT3 to provide the best fit with the feedthrough matrix D_L set to 0, compare with (3.13). The state space model for (3.32b) is:

$$u_{ds}(t) = u(t) + (T_{ds}/T_{us} - 1)\, \mathcal{Q}[u(t)], \tag{3.33b}$$

where the operator $\mathcal{Q}$ is fully described by equation (3.25). These equations can be numerically integrated in time with respect to the three internal state vectors $\{x_T, x_-, x_+\}$ describing respectively the acoustic state and the states of the two linear operators, see again (3.25). At each time step, $u(t)$ can be calculated with (3.33a), and $u_{ds}(t)$ can be calculated with (3.33b). Notice that if D_T were not set to 0 in (3.33a), an algebraic loop would appear, because $u(t)$ would depend on $u_{ds}(t)$, but also $u_{ds}(t)$ would depend on $u(t)$ because of (3.33b). This would require a study of the problem in the context of differential algebraic equations, with an additional root solver operation at each time step.

As initial condition $\boldsymbol{x} = \{x_T, x_-, x_+\}$ we keep generating a new random initial condition until physical values of $u_{ds}(t)$ and $u(t)$ result from (3.33a) and (3.33b). In particular, the random initial state should predict a value for the velocity u upstream of the flame such that the flame response is defined for such an amplitude, and such that the gain of the nonlinear operator is in a limited range. The system is then time-integrated until it converges to a limit cycle. An example is reported in Fig. 3.11.

At $L = 1.01\,\text{m}$ the system is linearly stable (see Fig. 3.8.a), and we check that the system converges to the steady solution for a set of random initial conditions. Subsequently, we force the system with an external, artificial harmonic source at the frequency of the least stable linear mode, which we stop after $\Delta t = 0.2\,\text{s}$. In this second

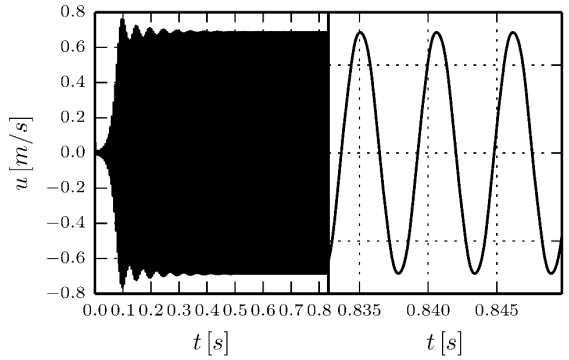

(a) velocity $u(t)$ just upstream of the flame surface

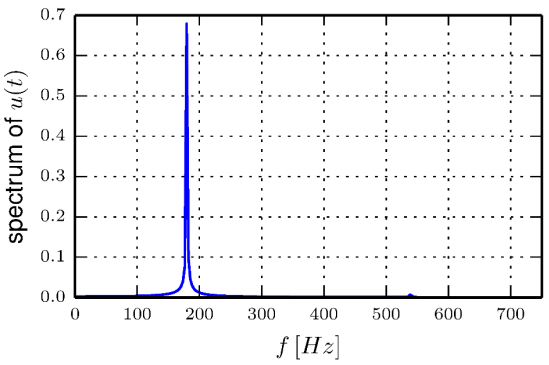

(b) Estimated power spectral density of $u(t)$.

Fig. 3.11 Time simulation of the system of equations (3.33) for a fixed value of the length L =0.8 m of the downstream duct. a) represents the time domain signal, and b) the spectrum of the signal. The system converges to a limit cycle. The third harmonic is visible in b). Analogous simulations are carried out for all lengths L.

case, the system converges to a stable limit cycle. This scenario describes a subcritical Hopf bifurcation.

3.4.3 Comparison

To compare the time domain simulations with the frequency domain simulations, we extract (Choi, 1997) the amplitude and the frequency of the dominant harmonic from the saturated limit cycle of $u(t)$ of each simulation, run for each value of the length L. In the first round of simulations, the design frequency ω_d is set to the frequency of the least stable mode of the linear stability analysis. These results are reported with a continuous green line in Fig. 3.12. We observe a general qualitative agreement with the frequency domain results (coloured dots, the same as Fig. 3.9).

We also run a second round of simulations, setting ω_d to the frequency of the saturated limit cycle of the first round of simulations. We then run a third round of simulations in the same way, reported with the continuous red line in Fig. 3.12. The agreement with the frequency domain results is now much better.

We finally report the normalised difference between the two sets of results, as a percentage, in Fig. 3.13. The error diminishes with the number of the iteration at most points. It is larger in the transition zone discussed at the end of section §3.4.1.2, reported in the figure between the two vertical dashed lines, where the analysis in the frequency domain is harder. In particular, the error is largest at $L = 0.98$,0.99 m, where it is fundamentally not correct to compare the two approaches because the analysis in

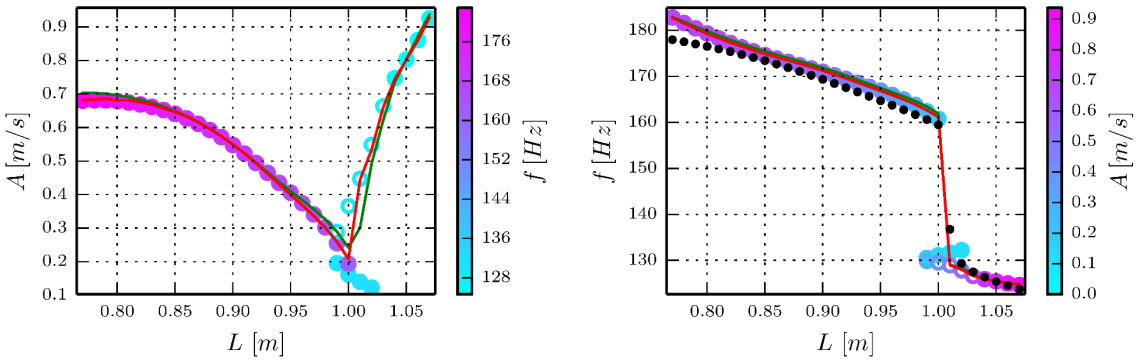

(a) Amplitude of oscillation A (b) Frequency of oscillation f

Fig. 3.12 Comparison of the results of the time domain (continuous lines) and the frequency domain (the same circles as Fig. 3.9) approaches, in terms of amplitude (in a)) and frequency of oscillation (in b)) of the saturated limit cycle. The green line is obtained with a first time simulation by setting the flame model design frequency ω_d to the frequency of the least stable linear mode (reported as black dots in b)). The red line is obtained by iterating the process two times.

the frequency domain is not complete: the stability of the reported solutions cannot be fully ascertained and more solutions may exist.

3.5 Conclusions

We present a state-space realization $\mathcal{Q}$ of a describing function Q, combining two Hammerstein models. For the linear part of the operators we use a rational function approximation, while for the nonlinear part of the model we propose the use of Fourier–Bessel series. The evaluation of the realization is fully automated and not iterative, and allows the study in the time domain of the behaviour of a system in a range of frequencies centred around a design frequency f_d.

We apply the tool to a thermoacoustic system, comparing the results of a time domain analysis using the state-space realization $\mathcal{Q}$ with the results of a nonlinear frequency-domain analysis using the original describing function Q.

In all the cases where the frequency-domain analysis is simple there is very good agreement between the results, validating the accuracy of the state-space realization proposed here.

In the other cases, the nonlinear frequency-domain analysis is difficult or not possible without further information about the system. In these latter cases the state-space

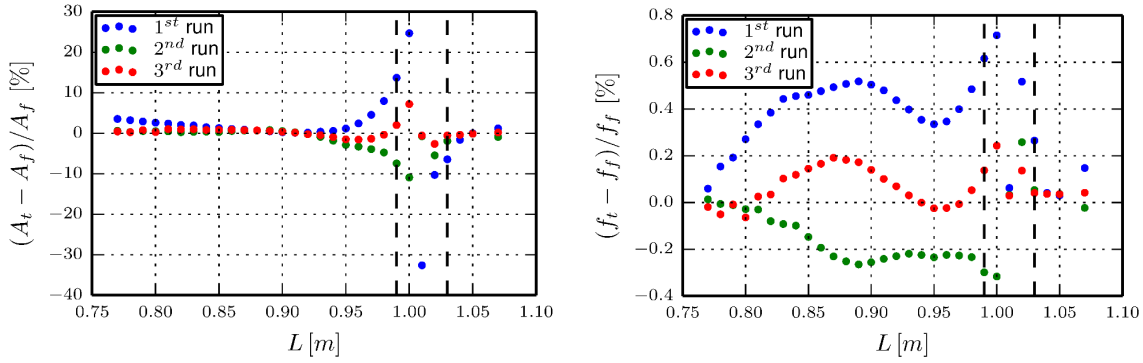

(a) Relative error for the predicted amplitude A

(b) Relative error for the predicted frequency f

Fig. 3.13 Error between the results obtained in the frequency domain (subscript f) and in time domain (subscript t), in percentage. The agreement is very good, except in the region where the frequency-domain stability analysis is not conclusive, delimited by the two vertical dashed lines.

realization can be used as a rough tool to isolate one mode at a time, and provide quick results.

This tool will be particularly useful in the study of thermoacoustic oscillations in annular combustion chambers, where a time domain approach to the problem has so far been more successful than a frequency domain approach. It allows an accurate description of the nonlinear saturation of the problem, improving on existing time domain solvers Pankiewitz and Sattelmayer (2003); Schuermans et al. (2003); Stow and Dowling (2009).

We observe that it may be possible to change the design frequency f_d of $\mathcal{Q}$ during the time domain simulation, by extracting in real-time the instantaneous frequency of oscillation of the system and incrementally retuning the model. The extraction could be done with a nonlinear Kalman filter Hajimolahoseini et al. (2012).

3.6 Appendices

3.6.1 Describing function calculation

In this appendix we evaluate the describing function (defined by (3.1)) of the saturation function $\mathcal{N}$. We will prove here the more general result for an input with structure

$$u(t) = A_1 \cos(\omega t + \varphi_1) + A_2 \cos(\omega t + \varphi_2) \tag{3.34}$$

to the function $\mathcal{N}$, as opposed to the case under consideration in this chapter introduced in (3.1) where $u(t) = A\cos(\omega t)$. In particular, the input described by (3.34) describes the contribution of two modes, oscillating at the same frequency, instead of a single sinusoidal input $A\cos(\omega t + \varphi)$. The motivation to cover this more general case is to make this framework usable in rotationally symmetric annular combustors featuring azimuthal modes. In that case, each burner is subject to the combined input of two thermoacoustic modes, depending on the amplitudes A_1 and A_2 of the two modes at that location, and on their phases φ_1, φ_2. Once the result for the input (3.34) is obtained, it will be sufficient to set $A_1 = A$, $\varphi_1 = \varphi_2 = A_2 = 0$ to obtain the special case of the single input response used in this chapter, as presented at the end of the appendix.

We proceed by rewriting u as

$$u = a\cos(\omega t) + b\sin(\omega t) \tag{3.35}$$

by introducing the costants

$$\begin{cases} a & \equiv A_1\cos\varphi_1 + A_2\cos\varphi_2 \\ b & \equiv -A_1\sin\varphi_1 - A_2\sin\varphi_2 \end{cases} \tag{3.36}$$

Notice that a, b do not depend on the time variable t. We study the averaging integral in the definition (3.1) of describing function for the operator $\mathcal{N}$, and we will later divide by the amplitude A to recover the full expression. In other words, for the time being we study the product $N(A,\omega)A$. We substitute in the product the equation (3.35) and change the time variable:

$$\frac{1}{\pi}\int_0^{2\pi} \mathcal{N}\left(a\cos t + b\sin t\right)\left(\cos t + i\sin t\right) dt = f_c + i f_s \tag{3.37}$$

We substitute the expression for $\mathcal{N}$ from (3.17):

$$\begin{aligned} f_c =& \frac{1}{\pi}\int_0^{2\pi} q^{erf}_{\mu,\kappa}(a\cos t + b\sin t)\cos t dt + \\ & \sum_{n=1}^{N}\frac{c_n}{\pi}\int_0^{2\pi} J_1(\hat{u}_n(a\cos t + b\sin t))\cos t dt \\ \equiv & f_c^{erf} + \sum_{n=1}^{N} c_n f_c^{b,n} \end{aligned} \tag{3.38a}$$

$$\begin{aligned} f_s =& \frac{1}{\pi}\int_0^{2\pi} q^{erf}_{\mu,\kappa}(a\cos t + b\sin t)\sin t dt + \\ & \sum_{n=1}^{N}\frac{c_n}{\pi}\int_0^{2\pi} J_1(\hat{u}_n(a\cos t + b\sin t))\sin t dt \\ \equiv & f_s^{erf} + \sum_{n=1}^{N} c_n f_s^{b,n} \end{aligned} \tag{3.38b}$$

We study first the integrals f_c^{erf} and f_s^{erf} due to the error function in section §3.6.1.1, and then each of the N integrals $f_c^{b,n}$ and $f_s^{b,n}$ of the Fourier–Bessel series in section §3.6.1.2. We put together the expressions and discuss them in section §3.6.1.3.

3.6.1.1 Averaging the error function

We substitute the definition of $q^{erf}_{\mu,\kappa}$ from (3.18) into the expression of f_c^{erf} and f_s^{erf} in (3.38). We obtain

$$f_c^{erf} = \frac{\kappa}{\pi}\int_0^{2\pi} \operatorname{erf}\left(\frac{\sqrt{\pi}\mu}{2\kappa}(a\cos t + b\sin t)\right)\cos t dt \tag{3.39a}$$

$$f_s^{erf} = \frac{\kappa}{\pi}\int_0^{2\pi} \operatorname{erf}\left(\frac{\sqrt{\pi}\mu}{2\kappa}(a\cos t + b\sin t)\right)\sin t dt \tag{3.39b}$$

For conciseness, we introduce the constant

$$k = \sqrt{\frac{\pi}{8}}\frac{\mu}{\kappa}, \tag{3.40}$$

so that the argument of the erf function is $\sqrt{2}k(a\cos t + b\sin t)$. This leads to neater expressions in the following. We proceed by expressing the argument of the exponential function as

$$a\cos t + b\sin t = R\sin(t+\psi), \tag{3.41}$$

where R and ψ are defined as

$$R \equiv \sqrt{a^2 + b^2} \tag{3.42a}$$

$$\psi \equiv \arg(b + ia) \tag{3.42b}$$

The two integrals (3.39) become

$$f_c^{erf} = \frac{\kappa}{\pi} \int_0^{2\pi} \operatorname{erf}\left(\sqrt{2}kR\sin(t+\psi)\right)\cos t dt \tag{3.43a}$$

$$f_s^{erf} = \frac{\kappa}{\pi} \int_0^{2\pi} \operatorname{erf}\left(\sqrt{2}kR\sin(t+\psi)\right)\sin t dt \tag{3.43b}$$

We exploit the fact that the erf function is defined as an integral itself, and apply integration by parts to (3.43a):

$$\begin{aligned} f_c{}^{erf} = \frac{\kappa}{\pi}\left[\operatorname{erf}\left(\sqrt{2}kR\sin(t+\psi)\right)\sin t\right]_0^{2\pi} - \\ \frac{\kappa}{\pi}\frac{2}{\sqrt{\pi}}\sqrt{2}k\int_0^{2\pi} e^{-2k^2R^2\sin^2(t+\psi)} R\cos(t+\psi)\sin t dt \end{aligned} \tag{3.44}$$

The first term trivially vanishes. In the second, $2/\sqrt{\pi}$ is the factor present in the definition (3.18) of the erf function, and $\sqrt{2}k$ comes from the chain rule of the derivative of erf with respect to t, together with the term $R\cos(t+\psi)$ inside the integral. Substituting the definition of k from (3.40) only at its first occurrence into the second term, we can simplify:

$$\frac{\kappa}{\pi}\frac{2}{\sqrt{\pi}}\sqrt{2}k = \frac{\mu}{\pi} \tag{3.45}$$

We now apply a change of integration variable $t \to \chi - \psi$ to the integral (3.44), and because the integrand is periodic in t and then in χ, we keep the same limits of integration in the new variable.

$$f_c^{erf} = -\frac{\mu}{\pi} R \int_0^{2\pi} e^{-2k^2R^2\sin^2\chi}\cos\chi\sin(\chi-\psi)d\chi \tag{3.46}$$

We then expand the trigonometric term $\sin(\chi-\psi)$, and take the sum out of the integral. We obtain

$$f_c^{erf} = -\mu R\left[+E_{sc}\cos\psi - E_{cc}\sin\psi\right] \tag{3.47a}$$

$$f_s^{erf} = -\mu R\left[-E_{sc}\sin\psi - E_{cc}\cos\psi\right] \tag{3.47b}$$

where we introduced the integrals

$$E_{sc} \equiv \frac{1}{\pi}\int_0^{2\pi} e^{-2k^2R^2\sin^2\chi}\cos\chi\sin\chi d\chi = 0 \tag{3.48a}$$

$$E_{cc} \equiv \frac{1}{\pi}\int_0^{2\pi} e^{-2k^2R^2\sin^2\chi}\cos^2\chi d\chi = \frac{2}{\pi}\int_0^{\pi} e^{-2k^2R^2\sin^2\chi}\cos^2\chi d\chi \tag{3.48b}$$

The first integral (3.48a) is zero since its integrand is odd. In (3.48b), we exploited the fact that the integrand has period π. We then use power reduction formulas on the terms $\sin^2\chi$ and $\cos^2\chi$:

$$E_{cc} = \frac{2}{\pi}\int_0^{\pi} e^{-k^2R^2(1-\cos 2\chi)}\frac{1+\cos 2\chi}{2}d\chi = \frac{1}{2\pi}\int_0^{2\pi} e^{-k^2R^2(1-\cos t)}(1+\cos t)dt \tag{3.49}$$

The integrand in (3.49) has period 2π and is an even function of t, so:

$$\begin{aligned} E_{cc} =& \frac{1}{\pi}\int_0^{\pi} e^{-k^2R^2+k^2R^2\cos t}(1+\cos t)dt = \\ =& e^{-k^2R^2}\left(\frac{1}{\pi}\int_0^{\pi} e^{k^2R^2\cos t}dt + \frac{1}{\pi}\int_0^{\pi} e^{k^2R^2\cos t}\cos t dt\right) \\ =& e^{-k^2R^2}\left(I_0(k^2R^2) + I_1(k^2R^2)\right) \end{aligned} \tag{3.50}$$

In (3.50), $I_0(x)$ and $I_1(x)$ are the modified Bessel functions of the first kind of the zero and first order respectively. We first substitute (3.50,3.48a) in (3.47), and then we substitute $R\sin\psi = a$ and $R\cos\psi = b$. We obtain:

$$f_c^{erf} = a f_{nl}^{erf}(kR) \tag{3.51a}$$

$$f_2^{erf} = b f_{nl}^{erf}(kR) \tag{3.51b}$$

with

$$f_{nl}^{erf}(kR) \equiv \mu e^{-k^2R^2}\left(I_0(k^2R^2) + I_1(k^2R^2)\right) \tag{3.52}$$

acting as a gain, as it multiplies the linear term in (3.51) and depends on the amplitude of oscillation. The two analytical expressions (3.51) have been compared with the numerical integration of (3.38) and its counterpart for a few values of μ, κ, a, b, and lead to relative errors of the order of machine precision, thus confirming their validity.

3.6.1.2 Averaging Bessel functions

The n-th term of $f_c^{b,n}$ and of $f_s^{b,n}$ in (3.38) are respectively

$$f_c^{b,n} \equiv \frac{1}{\pi}\int_0^{2\pi} J_1(2u_n a\cos t + 2u_n b\sin t)\cos t dt \tag{3.53a}$$

$$f_s^{b,n} \equiv \frac{1}{\pi}\int_0^{2\pi} J_1(2u_n a\cos t + 2u_n b\sin t)\sin t dt \tag{3.53b}$$

where we introduced $u_n \equiv \hat{u}_n/2$. We define $\hat{f}_j^{b,n} = f_c^{b,n} + i f_s^{b,n}$ and apply the substitution

$$z = e^{it},\ \sin t = \frac{1}{2i}\left(1 - \frac{1}{z}\right),\ \cos t = \frac{1}{2}\left(1 + \frac{1}{z}\right) \tag{3.54}$$

We obtain

$$\hat{f}_j^{b,n} = \frac{1}{\pi}\int_0^{2\pi} J_1\left(u_n(a-ib)z + u_n(a+ib)\frac{1}{z}\right) z dt \tag{3.55}$$

We now change the line integral into a contour integral in the complex plane on the circle $|z| = 1$. From (3.54) we have that $dt = dz/iz$, and

$$\hat{f}_j^{b,n} = \frac{1}{\pi i}\oint_{|z|=1} J_1\left(u_n(a-ib)z + u_n(a+ib)\frac{1}{z}\right) dz \tag{3.56}$$

The Bessel function $J_1(z)$ is an entire function, so the only singularity of $\hat{f}_j^{b,n}(z)$ is at the origin, and is of the essential type. We can then apply the residue theorem,

$$\begin{aligned}\hat{f}_j^{b,n} &= \frac{1}{\pi i}\, 2\pi i \mathrm{Res}\left[J_1\left(u_n(a-ib)z + u_n(a+ib)\frac{1}{z}\right)\right]_{z=0} = \\ &= 2\mathrm{Res}\left[G(z)\right]_{z=0}\end{aligned} \tag{3.57}$$

We expand the Bessel function in $G(z)$ with its Laurent series:

$$G(z) = \sum_{m=0} \frac{(-1)^m u_n^{1+2m}}{m!\,(m+1)!}\left(\frac{(a-ib)z + (a+ib)/z}{2}\right)^{1+2m} \tag{3.58}$$

We substitute the binomial expansion of the power of the sum

$$\begin{aligned}&\left(\frac{(a-ib)z + (a+ib)/z}{2}\right)^{1+2m} = \\ &\frac{1}{2^{1+2m}}\sum_{k=0}^{1+2m} z^{k-(2m+1-k)}\binom{1+2m}{k}(a-ib)^k(a+ib)^{1+2m-k}\end{aligned} \tag{3.59}$$

The residue in (3.58) is the sum of the coefficients of the term $1/z$. Therefore, in the sum (3.59) we retain only the term with $k-(2m+1-k)=-1$, from which follows $k=m$. This term of (3.59) is:

$$\frac{1}{2^{1+2m}}z^{-1}\binom{1+2m}{m}(a-ib)^m(a+ib)^{m+1} = \frac{a+ib}{2}\frac{1}{2^{2m}}z^{-1}\frac{(2m+1)!}{m!\,(m+1)!}(a^2+b^2)^m \tag{3.60}$$

Equation (3.57) evaluates to

$$\hat{f}_j^{b,n} = (a+ib)\sum_{m=0}^{\infty}\frac{(-1)^m(2m+1)!\,u_n^{1+2m}}{(m!\,(m+1)!\,)^2}\left(\frac{R}{2}\right)^{2m}$$

with $R=\sqrt{a^2+b^2}$. This series converges to

$$\hat{f}_j^{b,n} = (a+ib)\frac{2J_0\left(u_n\sqrt{a^2+b^2}\right)J_1\left(u_n\sqrt{a^2+b^2}\right)}{\sqrt{a^2+b^2}} \tag{3.61}$$

The two forcing terms (3.53) can be evaluated as the real and imaginary part of (3.61):

$$f_c^{b,n} = a f_{nl}^{b,n}(R) \tag{3.62a}$$
$$f_s^{b,n} = b f_{nl}^{b,n}(R) \tag{3.62b}$$

where we introduced

$$f_{nl}^{b,n}(R) \equiv 2\frac{J_0\left(u_nR\right)J_1\left(u_nR\right)}{R} \tag{3.63}$$

3.6.1.3 Final expression

The final expression of f_c and of f_s is obtained by substituting (3.51) and (3.62) into (3.38):

$$f_c(a,b) = a\left(f_{nl}^{erf}(kR)+\sum_{n=1}^{N}c_n f_{nl}^{b,n}(R)\right) = a f_{nl}(R) \tag{3.64a}$$
$$f_s(a,b) = b\left(f_{nl}^{erf}(kR)+\sum_{n=1}^{N}c_n f_{nl}^{b,n}(R)\right) = b f_{nl}(R) \tag{3.64b}$$

with $u_n = \hat{u}_n/2$, the constant $k = \mu/\kappa\sqrt{\pi/8}$ as defined in (3.40), the value of R is defined in (3.42a) and

$$f_{nl}(R) \equiv f_{nl}^{erf}(kR) + \sum_{n=1}^{N} c_n f_{nl}^{b,n}(R) \tag{3.65}$$

where f_{nl}^{erf} and $f_{nl}^{b,n}$ have been defined respectively in (3.52) and (3.63). The two terms f_c and f_s in (3.64) are symmetric with respect to a, b, since we have $f_c(a, b) = f_s(b, a)$.

By exploiting the fact that $\lim_{R\to 0} J_1(R)/R = 1/2$, and then substituting (3.21), we observe that

$$\lim_{R\to 0} f_{nl}(R) = \mu + \sum_{j=0}^{N} c_n u_n = \mu + \frac{1}{2}\sum_{j=0}^{N} c_n \hat{u}_n \equiv \beta \tag{3.66}$$

where we substituted the property (3.21) in the last passage. It can be proved that the first derivative at zero is

$$\lim_{R\to 0} \frac{\partial f_{nl}}{\partial R}(R) = 0, \tag{3.67}$$

meaning that f_{nl} is constant at first order in R.

In the case of the input described by a single sinusoid $A\cos(\omega t)$, it is sufficient to set $A_1 = A$, $\varphi_1 = \varphi_2 = A_2 = 0$. In the definitions (3.36) this leads to $a = A, b = 0$, and the substitution of these in (3.64) leads to

$$\begin{aligned} f_c(a, b) =& A\left(f_{nl}^{erf}(kA) + \sum_{n=1}^{N} c_n f_{nl}^{b,n}(A)\right) \\ =& A f_{nl}(A) && \text{(3.68a)} \\ f_s(a, b) =& 0 && \text{(3.68b)} \end{aligned}$$

The component in quadrature with the input signal u is zero, and $N(A)$ is real valued. Substituting (3.68) in (3.37), and because (3.37) is equal to $N(A, \omega)A$, we obtain

$$N(A, \omega) = f_{nl}(A) \tag{3.69}$$

with f_{nl} matching the RHS of (3.22).

Chapter 4

Weakly nonlinear analysis of annular combustors

Part of the material presented in this chapter was published as Ghirardo et al. (2015b).

4.1 Introduction

A successful method for modelling thermoacoustic instabilities is the truncated harmonic balance method (Boudy et al., 2011; Dowling, 1997; Noiray et al., 2008; Palies et al., 2011). This approach has so far been restricted to situations with only one mode of the system, close to the Hopf bifurcation, and to longitudinal configurations. Under these restrictions, the method involves the study of the solutions of a nonlinear dispersion relation $f(\omega, A) = 0$ that depends on the amplitude $A > 0$ of the oscillation. A limit-cycle is formed if there exists a non-trivial solution with a zero growth-rate, i.e. $A > 0, \omega \in \mathbb{R}$. In the analysis, there is no need to study the phase φ of the oscillation, because the system is self-excited and is then invariant under a shift of the time variable. For a detailed description, we refer the reader to Dowling (1997); Noiray et al. (2008).

The application of this framework to annular combustors is more challenging because of the presence of azimuthal modes. These appear as mode pairs, with amplitudes A_1 and A_2 (say), because of the discrete rotational symmetry of the problem. Although the system remains time-invariant to a temporal shift, the phase difference of the oscillations of the two modes, defined as $\varphi \equiv \varphi_1 - \varphi_2$, plays a role in the dynamics. This leads to finding the solutions of a nonlinear dispersion relation $f(\omega, A_1, A_2, \varphi) = 0$ and evaluating their stability. This is harder for two modes than for one. Some introductory work has been carried out by Campa and Camporeale (2014); Campa et al. (2013)

using a Helmholtz solver, where the stability with respect to only the amplitude of the mode was considered.

Low-order, state-space models overcome this difficulty (Ghirardo and Juniper, 2013; Noiray et al., 2011; Noiray and Schuermans, 2013; Schuermans et al., 2006). They allow the discussion of not just the amplitude of the solutions, but also the temporal evolution of the system and the stability of the solutions, features missing in the truncated harmonic balance method. Usually the method of averaging is applied to the state-space model, allowing a discussion of the temporal evolution of the two amplitudes A_1, A_2 and of the phase difference φ. The proposed fluctuating heat release rate model is limited in those studies to simple phenomenological expressions, in terms of the acoustic pressure and/or the acoustic azimuthal velocity. Also, only systems with fluctuating heat release rate uniformly distributed along the circumference were studied.

This chapter bridges the gap between low-order state space models and the truncated harmonic balance approach. We first show in §4.2 that the equations of the low-order model can be obtained by studying the governing equations of the problem as weakly nonlinear. We then show how to exploit the describing function in applying the method of temporal averaging in §4.3. This allows the flame response to remain generic, in contrast with all previous studies that considered a specific fluctuating heat release rate model. This allows us to prove with generality many properties of thermoacoustic oscillations in rotationally symmetric annular chambers. In particular we discuss the conditions under which spinning and standing waves are stable attractors of the system, and provide measurable quantities in experiments, which allow the validity of the hypotheses of this model to be tested.

We then present in §4.4 an example that illustrates this framework. The example is the first analytical study of an annular combustor capable of exhibiting thermoacoustic triggering, and shows that flames responding with a weak gain at small amplitudes and with a strong gain at large amplitudes can lead to stable, self-excited standing and spinning solutions in annular configurations. Notice that here the adjective stable refers to a limit-cycle solution, so that in the following for example a stable standing solution is a stable periodic attractor of the dynamical system, not a standing eigenmode of the problem with a negative growth-rate.

4.2 Governing equations

We discuss the geometry of the problem in §4.2.1 and the modelling of the fluctuating heat release rate in §4.2.2. We introduce the governing equations in §4.2.3, both in the time domain and the frequency domain. We discuss the degeneracy of the linear solutions in the frequency domain in §4.2.4. In §4.2.5 we carry out the weakly nonlinear analysis of the problem, which consists of two steps. Firstly, we increase/reduce the flame response until the linear solution is neutrally stable, and calculate its spatial structure. Then, we project the original nonlinear governing equations on this structure, which is assumed to change very little in the nonlinear regime because the system is weakly nonlinear.

The resulting truncated equations describe the temporal evolution of the amplitudes of two standing modes describing the whole acoustic field. These two amplitudes are two damped oscillator, coupled nonlinearly through the fluctuating heat release rate. The two oscillators' equations were already derived in chapter §2 for a fluctuating heat release rate uniformly distributed in the azimuthal direction using a Galerkin base instead.

4.2.1 Problem geometry

We adopt cylindrical coordinates z, r, θ, with the z-axis corresponding to the axis of the combustion chamber, and θ in $[0\,,\,2\pi)$. We assume that a number N_b of equal burners are equispaced along the annulus, and that each of the N_b sectors has the same geometry. The problem then has a discrete rotational group of symmetry of order N_b, with the fundamental domain being a sector spanning the angle $\Delta\theta \equiv 2\pi/N_b$.

In most industrial configurations, each flame is situated in a swirling flow, and all flames will swirl in the same direction. Depending on the geometry of the chamber, and on the viscous drag of inner and outer walls, a mean azimuthal velocity U_θ can be established in the annulus by the swirlers. In many cases the mean flow U_θ is very small compared to the speed of sound, and is fixed to zero in the following (for example U_θ is of the order of 10 m/s in Wolf et al. (2010)).

A non-zero azimuthal mean flow U_θ has two effects. Firstly, a non-zero U_θ makes one of the two spinning modes rotate faster and the other slower, and gives rise to slowly rotating modes, with pressure and velocity nodes moving at the speed of the mean azimuthal flow. See for example Wolf et al. (2010) for numerical evidence and a discussion. From a mathematical perspective, a non-zero U_θ makes the system lose the reflection symmetry mapping θ to $-\theta$, and restricts the group of discrete symmetries

of the system from the discrete rotation group with reflection symmetry D_{N_b} to the discrete rotation group Z_{N_b} without reflection symmetry of the same order. Refer to Bauerheim et al. (2015, 2014) for a detailed analysis of this first effect of U_θ in a linear framework.

Secondly, a non-zero U_θ bends the flames in the azimuthal direction, orthogonally to the burner's axis. This leads to a loss of axisymmetry of the mean flame shape, and this loss of axisymmetry is in turn a necessary condition for the flame to have a non-zero linear response to azimuthal velocity perturbations, as proven by Acharya and Lieuwen (2014).

We assume that the flames are acoustically compact, so that the fluctuating heat release rate is concentrated at the locations of the burners:

$$q(\boldsymbol{x},t) = \sum_{j=1}^{N_b} q_j(t)\delta(\boldsymbol{x}-\boldsymbol{x}_j) \qquad \boldsymbol{x} \equiv (z,r,\theta) \ , \ \boldsymbol{x}_j \equiv (0,\overline{r},\theta_j) \tag{4.1}$$

where δ is the Dirac delta in 3 dimensions, $\overline{r}$ is the radial position of the burners, and the plane $z=0$ is at the interface between the combustion chamber and the burners, which are located at the azimuthal positions θ_j, equispaced by $\Delta\theta$. We number the burners in anti-clockwise direction, and we choose a frame of reference so that the first burner is positioned at

$$\theta_1 = \frac{\pi}{4} + \frac{\Delta\theta}{4}\zeta \qquad \begin{cases} \zeta \in \{0,2\} & \text{if } N_b \text{ is even} \\ \zeta \in \{0,1,2,3\} & \text{if } N_b \text{ is odd} \end{cases} \tag{4.2}$$

The addition of the coefficient ζ is arbitrary, and corresponds to a simple rotation of the frame of reference, which will be useful later. For the time being, it suffices to observe from (4.2) that the position at the angle $\theta = \pi/4$:

- for $\zeta = 0$ is occupied by a burner;
- for $\zeta = 2$ is equispaced between two adjacent burners;
- for $\zeta = 1$ is $3\Delta\theta/4$ far from the preceding burner and $\Delta\theta/4$ far from the next.

4.2.2 Flame response

In this work, we assume that the flame response to the acoustic field is known, both in the linear and nonlinear regime. A common modelling approach consists of expressing the fluctuating heat release rate q_j of the j-th flame in terms of only the acoustic

axial velocity v_j just upstream of the burner. Doing so, we assume that the azimuthal, acoustic velocity u does not affect the response. This last point is proved theoretically in the linear limit for axisymmetric premixed flames in Acharya et al. (2012). This influence is experimentally verified to be small at low amplitudes of transverse forcing, for the cases of a burner positioned at pressure/velocity nodes, and for the case where it is swept by a spinning wave, where both u and v are excited at the same time (Saurabh et al., 2014). This effect is usually not taken into account because little is known in the nonlinear regime, i.e. at amplitudes of oscillation typical of self-excited thermoacoustic oscillations. In this chapter we make the same assumption, but point out that the nonlinear effect of the transverse azimuthal velocity u on each flame was investigated in chapter §2. It does not affect the linear stability properties of the system, but it does affect the nonlinear dynamics, and can explain stable standing solutions in axisymmetric annular chambers.

The longitudinal fluctuating velocity v_j oscillating in the j-th burner can be expressed as a linear time-invariant operator of the acoustic pressure difference Δp_j between the two sides of the burner, which are the chamber and the plenum, under the assumption of burner's acoustic compactness (Blimbaum et al., 2012), which allows the burners to be modelled as a lumped element. However, if we consider one mode oscillating harmonically in time, and we assume that the burner transfer function of the lumped element does not depend on the amplitude of oscillation (as validated for example in Ćosić et al. (2014)), then Δp_j is proportional to p_j, and one can express v_j as a linear operator of the local value of the pressure in the chamber p_j. The same reasoning applies also to two degenerate azimuthal modes oscillating at the same frequency, as will be the case in the following.

In particular, we model the fluctuating heat release rate as a time-invariant operator $\mathcal{Q}$:

$$q_j(t) = \mathcal{Q}[p_j(t)] \tag{4.3}$$

The operator $\mathcal{Q}$ contains all the complexity of the relation between p_j and q_j, and is nonlinear. We restrict our study to operators $\mathcal{Q}$ that, excited with a harmonic input $p = A\cos(\omega t)$, respond strongly at the same input frequency ω and weakly at higher harmonics $2\omega, 3\omega, \ldots$. This assumption is usually called the filtering hypothesis (Gelb and Vander Velde, 1968). We observe however that this is a feature of flames, acting like a low-pass filter on the acoustic input (Schuller et al., 2003). This, together with the acoustics being a narrow band filter, is one of the reasons why frequency domain calculations truncated at the first harmonic have proven successful in thermoacoustics

even for limit-cycles calculations. We also assume that $\mathcal{Q}$ is a stable operator, i.e. heat release fluctuations are present only if an external acoustic wave perturbs the flame. This means for example that we do not consider the flame response to its own acoustic field (Assier and Wu, 2014) if it leads to a linearly unstable flame.

We will study the problem both in the time and frequency domains. We refer with the calligraphic symbol $\mathcal{Q}$ to the time domain operator mapping pressure perturbations to fluctuations in heat release rate. In the frequency domain, we can calculate the corresponding describing function, which we label with the uppercase Q, defined as (Gelb and Vander Velde, 1968):

$$Q(A,\omega) \equiv \frac{1}{A}\frac{1}{\pi/\omega}\int_0^{2\pi/\omega} \mathcal{Q}\left[A\cos(\omega t)\right] e^{i\omega t} dt \tag{4.4}$$

The real and imaginary parts of $Q(A,\omega)$ express the amplitudes of the components of the fluctuating heat release rate, i.e. the output of the operator, respectively in phase and in quadrature with the sinusoidal pressure input. In particular it is $\mathrm{Re}[Q(A,\omega)]$ that leads to a contribution to the energy production term $q(t)p(t)$ in the Rayleigh criterion: if positive, the fluctuating heat release rate is partially in-phase with respect to the pressure input and the energy production term $\mathcal{Q}[p(t)]p(t)$ in the Rayleigh criterion is positive over a limit-cycle. One can then define the gain G and the phase lag ϕ of the flame response as:

$$Q(A,\omega) = G(A,\omega)e^{i\phi(A,\omega)} \tag{4.5}$$

$$\begin{cases} G(A,\omega) &= |Q(A,\omega)| \\ \phi(A,\omega) &= \arg[Q(A,\omega)] \end{cases} \tag{4.6}$$

Notice that for a model with a constant time-delay τ between the pressure and the fluctuating heat release rate we have $\phi(A,\omega) = +\omega\tau$. The sign convention of $+i\omega t$ in the exponential in equation (4.4) is historical, and we already point out that it is the opposite of the Fourier transform that we will use later.

The response of the flame is always bounded, i.e. the gain is always between 0 and $G_{\max}$. We also assume that the describing function is a continuous function of the amplitude A and of the frequency ω. This is usually an observed property of the experimental data (see for example Palies et al. (2011)), though it can also happen that the flame abruptly extinguishes above a certain amplitude of forcing, typically because of blow-off or flash-back events.

We also observe that the gain of acoustic damping sources are typically constant or decrease with the amplitude of oscillation (Ćosić et al., 2012). This means that limit-cycle oscillations occur because the flame response decreases with amplitude to the point of attaining an energy balance. Since we do not want to set a lower bound for the level of acoustic damping, we characterize the existence of an amplitude at which the energy balance is obtained by assuming that $\lim_{A\to\infty}|Q(A,\omega)| = 0$.

These three simple assumptions will play a key role in discussing the existence and the number of solutions later on (but not their stability).

4.2.3 Governing equations

Making a zero-Mach number assumption, the inhomogeneous wave equation governing the problem is, as derived for example by Nicoud et al. (2007) :

$$\nabla\cdot\left(\frac{1}{\rho_0}\nabla p_1\right) - \frac{1}{\gamma p_0}\frac{\partial^2 p_1}{\partial t^2} = -\frac{\gamma-1}{\gamma p_0}\frac{\partial q_1}{\partial t} \tag{4.7}$$

In the equation, subscript 0 refers to mean quantities, which depend on $\boldsymbol{x}$ only, while subscript 1 refers to fluctuating quantities, which depend on $\boldsymbol{x}$ and t. In this chapter we assume that the density ρ_0 and the isentropic coefficient γ are uniform. This hypothesis can possibly be lifted, but the equations become complicated without adding more insight. We also nondimensionalize the equations, with respect to a spatial lengthscale D (say the radius of the annular chamber) and the acoustic timescale D/c, with c being the mean speed of sound in the chamber. We assume an ideal gas, so that $\rho_0 c^2 = \gamma p_0$. We introduce the nondimensional fluctuating pressure p and fluctuating heat release rate q as

$$p \equiv \frac{p_1}{\rho_0 c^2} \qquad q \equiv q_1 \frac{\gamma-1}{\gamma p_0}\frac{D}{c} \tag{4.8}$$

In the new non-dimensional coordinates, equation (4.7) simplifies to

$$\frac{\partial^2 p}{\partial t^2} - \nabla^2 p = \sum_{j=1}^{N_b} \delta(\boldsymbol{x}-\boldsymbol{x}_j)\frac{\partial \mathcal{Q}[p_j]}{\partial t} \tag{4.9}$$

where we substituted the expression (4.1) and (4.3) for the fluctuating heat release rate q. We adopt the following convention for the definition of the Fourier transform:

$$\hat{f}(\omega) \equiv \frac{1}{\pi}\int_{-\infty}^{\infty} f(t)e^{-i\omega t}dt \qquad f(t) = \frac{1}{2}\int_{-\infty}^{\infty}\hat{f}(\omega)e^{+i\omega t}d\omega \tag{4.10}$$

By multiplying all terms of (4.9) by $e^{-i\omega t}/\pi$ and integrating over the time t we obtain the inhomogeneous Helmholtz equation:

$$\omega^2\hat{p}(\boldsymbol{x},\omega)+\nabla^2\hat{p}(\boldsymbol{x},\omega)=-\sum_{j=1}^{N_b}\delta(\boldsymbol{x}-\boldsymbol{x}_j)\frac{1}{\pi}\int_{-\infty}^{\infty}\frac{\partial\mathcal{Q}[p(\boldsymbol{x}_j,t)]}{\partial t}e^{-i\omega t}dt \tag{4.11}$$

Each of the integrals in the sum on the RHS can be rewritten as

$$\begin{aligned}\frac{1}{\pi}\int_{-\infty}^{\infty}\frac{\partial\mathcal{Q}[p(\boldsymbol{x}_j,t)]}{\partial t}e^{-i\omega t}dt &= +i\omega\frac{1}{\pi}\int_{-\infty}^{\infty}\mathcal{Q}[p(\boldsymbol{x}_j,t)]e^{-i\omega t}dt\\ &= +i\omega Q(|\hat{p}(\boldsymbol{x}_j)|,\omega)^*\hat{p}(\boldsymbol{x}_j,\omega)\end{aligned} \tag{4.12}$$

Notice that we assume that the response at the frequency ω of $\mathcal{Q}[p(\boldsymbol{x},t)]$ only depends on the amplitude $|\hat{p}(\boldsymbol{x})|$ of the solution at the same frequency ω. This is correct as long as all other harmonics are negligible, i.e. the filtering hypothesis holds (Gelb and Vander Velde, 1968). We also point out that in the last passage of (4.12) the complex conjugation denoted by the asterisk appears because of the different sign convention in the exponential in the definitions (4.4) and (4.10). Substituting (4.12) in (4.11) we obtain:

$$\omega^2\hat{p}(\boldsymbol{x},\omega)+\nabla^2\hat{p}(\boldsymbol{x},\omega)=-i\omega\sum_{j=1}^{N_b}\delta(\boldsymbol{x}-\boldsymbol{x}_j)Q(|\hat{p}(\boldsymbol{x}_j)|,\omega)^*\hat{p}(\boldsymbol{x}_j,\omega) \tag{4.13}$$

Equation (4.13) must be accompanied by suitable boundary conditions. At the combustor walls these will be zero normal gradient conditions for the pressure. At the axial extremes of the domain, the combustor inlet and outlet, the boundary conditions will in general be of impedance type, $\hat{p}=Z(\omega)\hat{u}$, with $Z(\omega)$ a complex-valued function.

4.2.4 Eigenmodes' degeneracy

We linearize equation (4.13) with respect to the amplitude $|\hat{p}(\boldsymbol{x})|$ of the solution and obtain:

$$\omega^2\hat{p}(\boldsymbol{x},\omega)+\nabla^2\hat{p}(\boldsymbol{x},\omega)=-i\omega\sum_{j=1}^{N_b}\delta(\boldsymbol{x}-\boldsymbol{x}_j)L(\omega)\hat{p}(\boldsymbol{x}_j,\omega) \tag{4.14}$$

where $L(\omega)$ is the transfer function of $\mathcal{Q}[p(t)]$ at infinitesimal amplitudes. The set of solutions of the eigenvalue problem (4.14) is $\{(\hat{\psi}_n(\boldsymbol{x}),\sigma_n+i\hat{\omega}_n)\ \text{ with }\ \sigma_n,\hat{\omega}_n\in\mathbb{R}\ ,n=1,2,\ldots\}$ where $\hat{\psi}_n(\boldsymbol{x})$ is the complex-valued eigenvector describing the shape of the

mode, and $\sigma_n + i\hat{\omega}_n$ is the corresponding eigenvalue. The modes and their eigenvalues can be calculated using a Helmholtz solver (Nicoud et al., 2007), or a thermoacoustic network model of the problem (Schuermans et al., 2003; Stow and Dowling, 2001).

We are particularly interested in azimuthal modes, i.e. solutions that are n-periodic in θ in $[0\,,\,2\pi]$, with n called the azimuthal wavenumber of the mode. As discussed by Bauerheim et al. (2014); Moeck et al. (2010), an azimuthal mode of wavenumber n belongs to an eigenspace of dimension two because of the rotational symmetry of the problem. There are however exceptions, when n is a multiple of $N_b/2$ in the case of an even number of burners N_b, and when n is a multiple of N_b in the case of N_b odd. We refer the reader also to section 5.4 of Salas (2013) for a concise summary of these two cases. These exceptions are non-degenerate cases, i.e. their modes belong to an eigenspace of dimension one, and occur because the rotational symmetry is discrete. We focus the analysis on the degenerate case where the dimensionality is two because: *1)* N_b is usually large and the excited modes typically have a low azimuthal wavenumber n (up to $n = 4$ in Seume et al. (1998)); *2)* the non-degenerate case does not give rise to the rich dynamics that can be observed in the degenerate case. We study thermoacoustic oscillations of azimuthal modes with $n = 1$ in the following, but the same analysis can be generalized to higher n, as long as the case stays degenerate.

We assume that these modes are close to their Hopf bifurcation. In other words, we assume that all other modes are stable, and only azimuthal modes of wavenumber $n = 1$ take part in the oscillation. One solution of the eigenspace with $n = 1$ is of the type $\tilde{\chi}(z, r)e^{i\theta}$. The Floquet-Bloch theorem states (Brillouin, 1953) that these solutions are perturbed by a pattern periodic in $2\pi/N_b$, because of the discreteness of the rotational symmetry of the burners and of any other feature of the problem, which is not considered here. We mention that this near field in θ can be taken into account (Mensah and Moeck, 2015).

Because of the reflection symmetry of the problem, there exists a second solution of the eigenspace that is symmetric with respect to the first, with structure $\tilde{\chi}(z, r)e^{-i\theta}$. We refer to these two modes in the following as spinning modes, because their phase linearly increases or decreases in the azimuthal direction.

By linearly combining these two spinning modes we can obtain two solutions ψ_1 and ψ_2 that have a constant phase as a function of θ:

$$\tilde{\psi}_1(\boldsymbol{x}) = \frac{1}{2}\left[\tilde{\chi}(z, r)e^{i\theta} + \tilde{\chi}(z, r)e^{-i\theta}\right] = \tilde{\chi}(z, r)\cos(\theta) \tag{4.15a}$$

$$\tilde{\psi}_2(\boldsymbol{x}) = \frac{1}{2i}\left[\tilde{\chi}(z, r)e^{i\theta} - \tilde{\chi}(z, r)e^{-i\theta}\right] = \tilde{\chi}(z, r)\sin(\theta) \tag{4.15b}$$

We refer to these modes in the following as standing modes, because if observed only at the burners' location they have pressure nodes and pressure anti-nodes fixed in time and in space. By direct substitution one can prove that they are orthogonal:

$$\int_\Omega \tilde{\psi}_1(\boldsymbol{x})\tilde{\psi}_2(\boldsymbol{x})^* d\Omega = 0, \tag{4.16a}$$

where Ω is the domain of the problem. One proves by direct substitution also that

$$\int_\Omega \tilde{\psi}_1^* \nabla^2 \tilde{\psi}_2 d\Omega = \int_\Omega \tilde{\psi}_2^* \nabla^2 \tilde{\psi}_1 d\Omega = 0 \tag{4.16b}$$

We normalise the standing modes by fixing the value of $\tilde{\chi}(0, \overline{r})$ to 1 at the burners' positions $(z, r, \theta) = (0, \overline{r}, \theta_j)$, so that

$$\begin{cases} \tilde{\psi}_1(\boldsymbol{x}_j) = \tilde{\psi}_1(0, \overline{r}, \theta_j) = c_j \\ \tilde{\psi}_2(\boldsymbol{x}_j) = \tilde{\psi}_2(0, \overline{r}, \theta_j) = s_j \end{cases}, \quad \text{with the notation:} \quad \begin{cases} c_j & \equiv \cos(\theta_j) \\ s_j & \equiv \sin(\theta_j) \end{cases} \tag{4.17}$$

4.2.5 Weakly nonlinear analysis

We want to study the solution of the nonlinear problem as a perturbation of its linear, neutrally stable counterpart. We obtain the latter by changing the problem (4.14), by substituting $\tilde{\xi} L(\omega)$ in place of $L(\omega)$, with $\tilde{\xi}$ a real, non-negative coefficient, so that for $\tilde{\xi} = 1$ we recover the original equations. We then look for the value ξ of the coefficient $\tilde{\xi}$ such that the growth-rate of the first two modes $\sigma_{1,2}(\tilde{\xi})$ is zero. In other words, we linearly increase/decrease the gain of the flame response to the level that makes the system neutrally stable. Notice that by looking at equation (4.14), one may guess that this may happen only for $\tilde{\xi} = 0$. This is not generally the case, due to the presence of partially transmitting boundary conditions or sources of damping, such as Helmholtz resonators and/or acoustic liners that dissipate energy in the system. In this work, we consider only linear damping. Nonlinear acoustic damping effects at the boundaries can be characterised with a describing function Schuller et al. (2009) in frequency domain, and its time-domain realization in time domain as discussed in chapter §3. We refer to quantities evaluated for $\tilde{\xi} = \xi$ by dropping the tilde, so that the eigenmodes are indicated with $\psi_1(\boldsymbol{x})$ and $\psi_2(\boldsymbol{x})$, and their real-valued eigenfrequency is $\omega_1 = \omega_2$.

For later use, we write equation (4.14) for the first two modes to obtain

$$\nabla^2\left[\psi_k(\boldsymbol{x})\right] = -\Big[\omega_k^2\psi_k(\boldsymbol{x}) - \sum_{j=1}^{N_b}\delta(\boldsymbol{x}-\boldsymbol{x}_j)\omega_k\xi\mathrm{Im}\left[L(\omega_k)\right]\psi_k(\boldsymbol{x}_j)\Big] - \quad \ldots$$
$$\ldots \quad i\sum_{j=1}^{N_b}\delta(\boldsymbol{x}-\boldsymbol{x}_j)\omega_k\xi\mathrm{Re}\left[L(\omega_k)\right]\psi_k(\boldsymbol{x}_j) \qquad k=1,2 \quad \omega_1=\omega_2 \tag{4.18}$$

We can multiply all terms of (4.18) by ψ_k^* and integrate over the domain Ω:

$$\int_\Omega \nabla^2\psi_k\psi_k^* d\Omega = -\left[\omega_0^2 + i\omega_k\alpha\right]\int_\Omega \psi_k\psi_k^* d\Omega \qquad k=1,2, \tag{4.19}$$

where, by exploiting the fact that $\sum_{j=1}^{N_b} c_j^2 = \sum_{j=1}^{N_b} s_j^2 = N_b/2$, we introduced the quantities

$$\omega_0^2 \equiv \omega_k^2 - \omega_k\xi\mathrm{Im}\left[L(\omega_k)\right]\mu\sum_{j=1}^{N_b}|\psi_k(\boldsymbol{x}_j)|^2 = \omega_k^2 - \omega_k\xi\mathrm{Im}\left[L(\omega_k)\right]\mu\frac{N_b}{2} \tag{4.20a}$$

$$\alpha \equiv \xi\mathrm{Re}\left[L(\omega_k)\right]\mu\sum_{j=1}^{N_b}|\psi_k(\boldsymbol{x}_j)|^2 = \xi\mathrm{Re}\left[L(\omega_n)\right]\mu\frac{N_b}{2} \tag{4.20b}$$

and $\mu = \mu_1 = \mu_2$ is a real-valued normalisation factor that is the same for the two modes, defined as:

$$\mu = \frac{1}{\int_\Omega \psi_1\psi_1^* d\Omega} \tag{4.21}$$

which physically measures the ratio between the maximum amplitude of oscillation of the mode at the burners and the amplitude of the whole 3D mode. In the two RHS of (4.20) the frequency $\omega_k = \omega_1 = \omega_2$ is much larger than the other terms, so that $\omega_0 \approx \omega_k$ and $\alpha \ll |\omega_k|$. This follows from the weakly nonlinear nature of thermoacoustic problems. The coefficient α is the equivalent damping of the system when the flame response is uniformly reduced in the annulus to the point of making the system neutrally stable, i.e. at $\tilde{\xi} = \xi$. The frequency ω_0 is the natural frequency of oscillation of the two acoustic modes when the flames and the acoustic damping are shut off. This paragraph led to equation (4.19), which will be used in the following.

At the value $\tilde{\xi} = \xi$ no dissipation/gain of energy in a limit-cycle occurs in the linearised system for the dominant mode, and the exact solution of the problem is

$$p(\boldsymbol{x},t) = \left[X_1\psi_1(\boldsymbol{x})e^{i(\omega_1 t+\varphi_1)} + X_2\psi_2(\boldsymbol{x})e^{i(\omega_1 t+\varphi_2)} + c.c.\right] \; + \; \text{decaying terms}, \tag{4.22}$$

where X_1 and X_2 are two complex-valued constants, and the decaying terms depend on the initial condition, and they will be neglected in the following because they converge to zero in time after the initial transient. We now study the original nonlinear problem (4.9) as a perturbation of this, as $\tilde{\xi}$ changes from ξ to 1. We choose as ansatz in the frequency domain

$$\hat{p}(\boldsymbol{x},\omega) = i\omega\left[\hat{\eta}_1(\omega)\psi_1(\boldsymbol{x}) + \hat{\eta}_2(\omega)\psi_2(\boldsymbol{x})\right] + \varepsilon\hat{p}_\varepsilon(\boldsymbol{x},\omega) \tag{4.23}$$

In (4.23), ε expresses the deviation of the nonlinear solution from the linear solution, because of the onset of higher harmonics in time and in space, and because of the structural change in the equations that can affect slightly the shape of the modes. Using equation (4.17), the expression for the pressure field at the burners' location reads

$$\hat{p}(\boldsymbol{x}_j,\omega) = \left[i\omega\hat{\eta}_1(\omega)c_j + i\omega\hat{\eta}_2(\omega)s_j\right] + \varepsilon\hat{p}_\varepsilon(\boldsymbol{x}_j,\omega) \tag{4.24}$$

We then substitute this ansatz into (4.13), multiply all terms by $-\psi_1(\boldsymbol{x})^*/(i\omega)$, and integrate over the domain Ω. We first exploit the orthogonality properties (4.16) between the two degenerate modes, and then substitute the equation (4.19) and obtain:

$$\begin{aligned}\Big[-\omega^2\hat{\eta}_1 + i\omega_1\alpha\hat{\eta}_1 + \omega_0^2\hat{\eta}_1\Big]\int_\Omega \psi_1\psi_1^* d\Omega = \quad &\dots \\ \dots \quad \sum_{j=1}^{N_b} Q^*\Big(|i\omega\hat{\eta}_1 c_j + i\omega\hat{\eta}_2 s_j|,\omega\Big)\Big[i\omega\hat{\eta}_1 c_j + i\omega\hat{\eta}_2 s_j\Big]c_j + \mathcal{O}(\varepsilon) \qquad &(4.25)\end{aligned}$$

Notice how on the LHS, the frequency ω_1 is the frequency of the mode ψ_1, so that in principle $i\omega_1\hat{\eta}_1$ is not the Fourier transform of $\partial\eta_1/\partial t$. However, the frequency of the nonlinear system ω is close to ω_1, and we can make this approximation. We take the inverse Fourier transform of all terms and obtain

$$\frac{\partial^2\eta_1}{\partial t^2} + \alpha\frac{\partial\eta_1}{\partial t} + \omega_0^2\eta_1 = \sum_{j=1}^{N_b}\mathcal{Q}\left[\frac{\partial\eta_1}{\partial t}c_j + \frac{\partial\eta_2}{\partial t}s_j\right]\mu c_j + \mathcal{O}(\varepsilon) \tag{4.26a}$$

$$\frac{\partial^2\eta_2}{\partial t^2} + \alpha\frac{\partial\eta_2}{\partial t} + \omega_0^2\eta_2 = \sum_{j=1}^{N_b}\mathcal{Q}\left[\frac{\partial\eta_1}{\partial t}c_j + \frac{\partial\eta_2}{\partial t}s_j\right]\mu s_j + \mathcal{O}(\varepsilon) \tag{4.26b}$$

where the second symmetric equation was obtained similarly but multiplying by ψ_2^*. In (4.26), the coefficients c_j and s_j were introduced in (4.17), and μ was defined in (4.21). The equations (4.26) are investigated in the rest of the chapter, and describe the temporal evolution of the amplitudes $\eta_1(t)$ and $\eta_2(t)$ of the two standing modes

ψ_1 and ψ_2. The LHS of equation (4.26a) describes a damped oscillator with natural frequency ω_0, defined in (4.20a), and the damping α, defined in (4.20b). The RHS of equation (4.26a) is the ensemble response of the flames. The argument $\eta_1 c_j + \eta_2 s_j$ of the operator $\mathcal{Q}$ is the local value of the pressure at the j-th burner truncated at zero order, as can be observed in equation (4.24). Notice how the local contribution of the j-th term in the sum on the RHS is weighted by the term c_j. In particular the fluctuating heat release rate close to where $c_j = \cos(\theta_j)$ is large makes a larger contribution to η_1.

Linear analysis

In the linear limit, by exploiting the fact that $\sum_{j=1}^{N_b} c_j s_j = 0$ and that $\sum_{j=1}^{N_b} c_j^2 = N_b/2$, equation (4.26a) simplifies to:

$$\frac{\partial^2 \eta_1}{\partial t^2} + \alpha \frac{\partial \eta_1}{\partial t} + \omega_0^2 \eta_1 = \sum_{j=1}^{N_b} \mathcal{L}\left[\frac{\partial \eta_1}{\partial t}\right] c_j^2 = \mu \frac{N_b}{2} \mathcal{L}\left[\frac{\partial \eta_1}{\partial t}\right] \tag{4.27}$$

where $\mathcal{L}$ is the linearization of the nonlinear time domain operator $\mathcal{Q}$, and the equation for the second oscillator (4.26b) follows similarly with s_j^2 in place of c_j^2. The two modes are linearly decoupled, and two Hopf bifurcations take place at the same time. In the linear limit,

$$\mathcal{L}\left[\frac{\partial p(t)}{\partial t}\right] = G(0,\omega_0)\frac{\partial p}{\partial t}\left(t - \frac{\phi(0,\omega_0)}{\omega_0}\right) \equiv \beta \frac{\partial p}{\partial t}(t-\tau) \tag{4.28}$$

where τ mimics the phase lag of the fluctuating heat release rate with respect to the pressure, and β is a linear driving coefficient. We substitute this into (4.27) and obtain:

$$\frac{\partial^2 \eta_1}{\partial t^2} + \alpha \frac{\partial \eta_1}{\partial t} + \omega_0^2 \eta_1 = \mu \frac{N_b}{2} \beta \frac{\partial \eta_1}{\partial t}\Big|_{t=t-\tau} \tag{4.29}$$

One can look for the solutions of the characteristic equation $P(\lambda) = 0$ of (4.29), with $\lambda = \sigma + i\omega_{lin}$. We opt for an iterative solution:

$$2\sigma^{(n+1)} = -\alpha + \frac{\mu N_b \beta}{2} e^{-\sigma^{(n)}\tau}\left(\cos(\omega_{lin}^{(n)}\tau) - \sigma^{(n)}/\omega_{lin}^{(n)} \sin(\omega_{lin}^{(n)}\tau)\right) \tag{4.30a}$$

$$\omega_{lin}^{(n+1)^2} = \omega_0^2 + \alpha\sigma^{(n)} + \sigma^{(n)^2} - \frac{\mu N_b \beta}{2} e^{-\sigma^{(n)}\tau}\left(\sigma^{(n)} \cos(\omega_{lin}^{(n)}\tau) + \omega_{lin} \sin(\omega_{lin}^{(n)}\tau)\right) \tag{4.30b}$$

Truncating the iteration at the first step, and starting with $\lambda^{(n=0)} = i\omega_0$, we obtain

$$\begin{cases} \sigma \approx \sigma^{(1)} = & -\frac{\alpha}{2} + \frac{\mu N_b \beta}{2} \cos(\tau\omega_0) \\ \omega_{lin}^2 \approx {\omega_{lin}^{(1)}}^2 = & \omega_0^2 - \omega_0 \frac{\mu N_b \beta}{2} \sin(\tau\omega_0) \end{cases} \tag{4.31}$$

We find that the system is linearly stable if the growth-rate σ is negative, i.e. if $\mu\beta\cos(\tau\omega_0)\ N_b/2 < \alpha$. In principle one can perform more iterations and evaluate the exact linear frequency of oscillation. This can be carried out also in the nonlinear regime and in transients, by solving a dispersion relation that is dependent on the amplitudes as well. The exact determination of the frequency of oscillation is however not part of this chapter, and we simply observe that the frequency of oscillation is typically close to the frequency ω_0 of the purely acoustic mode obtained neglecting acoustic energy sources and sinks.

To discuss a typical instability, we observe that the growth-rate σ, nondimensionalized with respect to the frequency ω_{lin}, is typically smaller than 0.08 in a thermoacoustically unstable annular combustor (see for example Bothien et al. (2015) for an industrial application). Equation (4.31) then provides a relation between the nondimensional linear driving coefficient β/ω_{lin} and the non-dimensional damping coefficient α/ω_{lin}:

$$2\frac{\sigma}{\omega_{lin}} = \frac{\beta\cos(\tau\omega_0)}{\omega_{lin}}\frac{\mu N_b}{2} - \frac{\alpha}{\omega_{lin}} \tag{4.32}$$

In this section we studied when the system (4.26) is linearly stable/unstable; this will be useful later to discuss if the system can exhibit thermoacoustic triggering. We then discussed the typical range for the parameters that occur in real applications; This will be used in §4.4 to discuss a plausible example.

4.2.6 The final oscillator model

We now fix $\mu = 1$ in (4.26) without loss of generality, because the same effect could be obtained by rescaling $\mathcal{Q}$. In the following we denote ω_0 simply as ω because we remain in the time domain. By neglecting the correction in $O(\varepsilon)$ and by denoting the time derivative with a prime, the system (4.26) is:

$$\eta_1'' + \omega^2\eta_1 = f_1(\eta_1', \eta_2') - \alpha\eta_1' \tag{4.33a}$$

$$\eta_2'' + \omega^2\eta_2 = f_2(\eta_1', \eta_2') - \alpha\eta_2' \tag{4.33b}$$

where the functions f_k on the RHS are:

$$f_1(\eta_1', \eta_2') = \sum_{j=1}^{N_b} \mathcal{Q}\left[\eta_1' c_j + \eta_2' s_j\right] c_j \tag{4.34a}$$

$$f_2(\eta_1', \eta_2') = \sum_{j=1}^{N_b} \mathcal{Q}\left[\eta_1' c_j + \eta_2' s_j\right] s_j \tag{4.34b}$$

This refactoring of the equations allows a more concise discussion in §4.3.

This section rigorously derived a set of governing equations for the instantaneous amplitude of oscillations of two standing modes. These equations are consistent with existing low-order models, which are based instead on the projection of the equations on a Galerkin basis $\{\cos\theta, \sin\theta\}$ which was chosen because it matches with experiments. A great advantage of this approach is that we can calculate the coefficients with a Helmholtz solver or a network model so that the model can be used as a predictive tool.

4.3 Slow flow

In §4.3.1 we obtain the slow flow equations (4.39), which describe the dynamics of the system at a slower timescale. In §4.3.2 we introduce what standing and spinning waves are and discuss some of their properties. In §4.3.3 we show that the solutions of the system are spinning and standing solutions, and that their amplitude is governed by the Rayleigh criterion. In §4.3.4.1 and §4.3.4.2 we discuss the stability of these solutions, and present general results on the existence and nature of these solutions, and provide physical interpretations of the stability conditions.

4.3.1 Temporal averaging

In this section we apply the method of time-averaging to the equations (4.33), by assuming that the terms $f_k(\eta_1', \eta_2') - \alpha\eta_k'$ are small. From a physical standpoint, this means that we are assuming that the dynamics of the acoustic waves (the LHS in (4.33)) are only slightly influenced by the net contribution of flame response and acoustic damping (the RHS in (4.33)). This can be observed experimentally in the time traces of pressure signals: usually thermoacoustic systems take many periods of oscillation to stabilize to a periodic solution, meaning that the amount of net energy contributed to the acoustics in one limit-cycle is small.

We express each oscillator as a harmonic oscillation (Sanders and Verhulst, 2007):

$$\begin{cases} \eta_k(t) = & A_k \sin(\omega t + \varphi_k)/\omega \\ \eta_k'(t) = & A_k \cos(\omega t + \varphi_k) \end{cases}, \qquad k = 1, 2 \tag{4.35}$$

with A_k, φ_k the amplitude and the phase of the k-th oscillator, slowly varying with respect to the fast time variable t, usually referred to as slow variables of the problem.

The expression of the pressure field at the burners' position can be rewritten in terms of A_k, φ_k by substituting (4.35) and (4.17) into (4.24) and neglecting terms of order $\mathcal{O}(\varepsilon)$:

$$p(\theta_j, t) = A_1 \cos(\omega t + \varphi_1)\cos(\theta_j) + A_2 \cos(\omega t + \varphi_2)\sin(\theta_j) \tag{4.36}$$

Applying the method of temporal averaging for a delayed system (Wahi and Chatterjee, 2004) we obtain the equations governing the temporal evolution of the slow variables:

$$A_k' = -\frac{\alpha}{2} A_k + \langle f_k \cos(\omega t + \varphi_k)\rangle \qquad k = 1, 2 \tag{4.37a}$$

$$\varphi' \equiv \varphi_1' - \varphi_2' = -\frac{1}{A_1}\langle f_1 \sin(\omega t + \varphi_1)\rangle + \frac{1}{A_2}\langle f_2 \sin(\omega t + \varphi_2)\rangle \tag{4.37b}$$

where $\varphi \equiv \varphi_1 - \varphi_2$ is the phase difference between the two oscillators, and the angled brackets denote averaging over a limit-cycle:

$$\langle f_k \cos(\omega t + \varphi_k)\rangle + i\langle f_k \sin(\omega t + \varphi_k)\rangle \equiv \frac{1}{2\pi/\omega}\int_0^{2\pi/\omega} f_k\Big[A_1 \cos(\omega t + \varphi_1), \quad \ldots \quad \ldots \quad A_2 \cos(\omega t + \varphi_2)\Big] e^{i(\omega t + \varphi_k)} dt \tag{4.38}$$

The period of averaging $2\pi/\omega$ is a constant, where ω is the frequency of oscillation appearing in (4.26). This has a slight effect on the accuracy of the method and will be discussed later.

We discuss in §4.7.1 of the appendix how to find an analytical solution of the terms (4.38). We present here only the key physical features of the solution. In the integral (4.38) the function f_k consists of the sum of the contributions of each burner. Each burner responds to the local value of the pressure field as described by (4.36), which depends on the two modes A_1, A_2. However both modes A_1 and A_2 oscillate at the same frequency ω, so that each burner responds to a single harmonic input. The averaged response of one burner to a harmonic signal is by definition (with some minor multiplicative coefficient's adjustments) the describing function of the flame. Then the

integrals (4.38) can be rewritten in terms of the gain G and of the phase lag ϕ of a single flame.

By substituting the solution of (4.38) into (4.37), we obtain the slow flow equations:

$$A_1' = -\frac{\alpha}{2}A_1 + \frac{1}{2}\sum_{j=1}^{N_b} G(R_j,\omega)\left[A_1 c_j^2 \cos\phi(R_j,\omega) + A_2 c_j s_j \cos(\phi(R_j,\omega)+\varphi)\right] \quad (4.39a)$$

$$A_2' = -\frac{\alpha}{2}A_2 + \frac{1}{2}\sum_{j=1}^{N_b} G(R_j,\omega)\left[A_2 s_j^2 \cos\phi(R_j,\omega) + A_1 c_j s_j \cos(\phi(R_j,\omega)-\varphi)\right] \quad (4.39b)$$

$$\varphi' = -\frac{1}{2}\sum_{j=1}^{N_b} G(R_j,\omega)\left[(s_j^2-c_j^2)\sin\phi(R_j,\omega) + c_j s_j\left(\frac{A_2}{A_1}\sin(\phi(R_j,\omega)+\varphi) + \frac{A_1}{A_2}\sin(\phi(R_j,\omega)-\varphi)\right)\right. \quad (4.39c)$$

where R_j in (4.39) is defined as:

$$R_j(A_1,A_2,\varphi) = \sqrt{(A_1 c_j)^2 + (A_2 s_j)^2 + 2A_1 A_2 c_j s_j \cos(\varphi)} \quad (4.40)$$

and the terms $A_1 c_j$ and $A_2 s_j$ are the amplitudes of the pressure of the two modes η_1, η_2 at the j-th burner. The amplitude R_j is then the slowly-varying amplitude of oscillation of the pressure at the $j-$th burner. Notice that both the gain G and the phase lag ϕ of each burner depend on the local amplitude of oscillation R_j, and that R_j plays a role in the equations only as their forcing amplitude. The spatial structure of R_j for standing and spinning waves is examined in section §4.3.2.

The effect of the acoustic damping coefficient α (first term on the RHS of (4.39a,4.39b)) is to push individually the two standing modes to smaller amplitudes, and it opposes the effect of the flame response (second term on the RHS of (4.39a,4.39b)). In order to reach a limit-cycle a balance between the two terms must be reached in both equations.

The synchronization of the two modes is described by equation (4.39.c), and determines the standing/spinning nature of the solutions. The synchronisation does not depend on the linear features of the system, but only on its nonlinear saturation features. In fact, equation (4.39.c) depends only indirectly on the amplitudes through the dependence on R_j if we fix a certain ratio A_1/A_2.

We do not discuss the linear stability of the fixed point at the origin $(A_1, A_2, \varphi) = (0, 0, \varphi)$, because it leads to the same results discussed earlier at the end of §4.2.5.

In summary, we applied the method of averaging to the dynamic equations of the two oscillators (4.33), which were in terms of the four variables $\{\eta_1, \eta_1', \eta_2, \eta_2'\}$. The original equations may exhibit limit-cycle solutions, oscillating at a fast, acoustic

timescale with frequency ω. The resulting equations (4.39) can be rewritten as

$$\begin{cases} A_1' &= f_{A_1}(A_1, A_2, \varphi) \\ A_2' &= f_{A_2}(A_1, A_2, \varphi) \\ \varphi' &= f_{\varphi}(A_1, A_2, \varphi) \end{cases} \qquad \boldsymbol{f}(A_1, A_2, \varphi) \equiv \begin{bmatrix} f_{A_1}(A_1, A_2, \varphi) \\ f_{A_2}(A_1, A_2, \varphi) \\ f_{\varphi}(A_1, A_2, \varphi) \end{bmatrix} \tag{4.41}$$

They describe the dynamic evolution of three variables, which are oblivious of the fast acoustic timescale: the two amplitudes of the standing modes A_1 and A_2 and their phase difference φ. The limit-cycle solutions of the oscillators are fixed points (A_1, A_2, φ) of the new set of equations. The timescale of this process depends in the linear regime on the relative strengths of the linear flame response and the acoustic damping, and in the nonlinear regime on the nonlinear saturation of the gain G and of the phase ϕ of the flames.

4.3.2 Standing and spinning waves

In this section we discuss the structure of standing and spinning waves. *Waves* are considered as possible initial conditions of the problem at a certain instant of time, and the system can drift away from this initial state as time evolves. This differs from standing and spinning *solutions*, which are waves that are also periodic solutions of the problem.

Some results presented here are well known in the literature, and are presented only for reference. In particular we prove in this section that a point in the state space of the averaged system with coordinates $(A_1, A_2, \varphi) = (A, A, k\pi/2)$ is always a standing or a spinning wave:

$$(A_1, A_2, \varphi) = (A, A, k\pi/2)\,,\ k \quad \text{even} \quad \Leftrightarrow \quad p(\theta, t) \text{ is a standing wave} \tag{4.42a}$$

$$(A_1, A_2, \varphi) = (A, A, k\pi/2)\,,\ k \quad \text{odd} \quad \Leftrightarrow \quad p(\theta, t) \text{ is a spinning wave} \tag{4.42b}$$

This follows from the structure of the pressure field (4.36), and is not a property of the dynamical equations (4.39). Some other results, regarding the structure of the slowly varying, local amplitude of pressure oscillation R_j, are new and have implications in the dynamic equations (4.39).

4.3.2.1 Spinning wave

A spinning wave of amplitude A travels with a phase speed $d\theta/dt$ equal to $\mp\omega$, either in the clockwise or anticlockwise direction at the burners' position:

$$\begin{aligned} p(\theta,t) =& A\cos\left(\omega t+\varphi_1 \pm \theta\right) \\ =& A\cos(\omega t+\varphi_1)\cos(\theta) + A\cos(\omega t+\varphi_1 \pm \pi/2)\sin(\theta) \end{aligned} \tag{4.43}$$

By comparing this with (4.36), we observe that for a spinning wave we have $A = A_1 = A_2$ and $\varphi = \pm\pi/2$, with the $+/-$ sign respectively for a mode rotating in the counter-clockwise/clockwise direction. We present in Figure 4.1.a the pressure field $p(\theta)$ obtained from (4.43), nondimensionalized with respect to the amplitude A, at two instants of time. As the wave moves to the right (anticlockwise direction), it maintains the same amplitude of oscillation.

We now simplify the expression $R_j(A_1, A_2, \varphi)$ in (4.40) by substituting $A_1 = A_2$ and $\varphi = \pi/2$ in (4.40), obtaining

$$R_j^{sp} = A \tag{4.44}$$

This means that the amplitude of oscillation of a spinning wave is constant along the annulus, see Figure 4.1.b.

4.3.2.2 Standing wave

A standing wave has velocity and pressure nodes fixed in time at the burners' positions, i.e.

$$p(\theta,t) = \sqrt{2}A\cos(\omega t+\varphi_1)\cos(\theta-\pi/4) \tag{4.45}$$

where the $\sqrt{2}$ factor will be explained later, and we have chosen a frame of reference with a pressure anti-node at $\overline{\theta} = \pi/4$. This can be rewritten as

$$p(\theta,t) = A\cos(\omega t+\varphi_1)\cos(\theta) + A\cos(\omega t+\varphi_1)\sin(\theta) \tag{4.46}$$

By comparing (4.46) with (4.36), we observe that $(A_1, A_2, \varphi) = (A, A, 0)$. This is why we put a $\sqrt{2}$ factor in equation (4.45).

We present in Figure 4.1.a the pressure field $p(\theta)$ obtained from (4.45), non-dimensionalized with respect to the amplitude A, at two instants of time $t = -\varphi_1/\omega$ (continuous red line) and $t + \Delta t = -(\varphi_1 + \pi/3)/\omega$ (dashed red line).

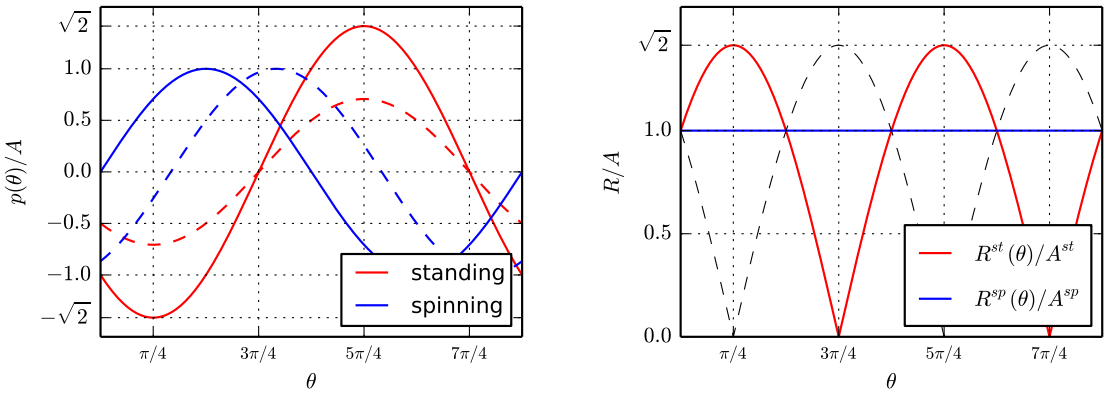

(a) pressure fields at two instants of time

(b) $R(\theta)$

Fig. 4.1 a) Pressure field of a spinning wave (blue) from equation (4.43) and of a standing wave (red) from equation (4.45), both at two instants of time. b) Amplitude of pressure oscillation of a standing wave (red line) from equation (4.47) and of a spinning wave from equation (4.44), both nondimensionalized with respect to the amplitude A of both modes $A_1 = A_2 = A$. This amplitude of oscillation is responsible for nonlinear saturation effects at the discrete angles θ_j where the burners are positioned. We also report with a dashed line the amplitude of the acoustic velocity of the standing mode for completeness. For a spinning wave, in a) one observes that in one period of oscillation every point in the annulus experiences the same pressure variation, as the wave rotates and makes a full revolution in one period. This is consistent with R^{sp} in b), where the amplitude of oscillation of a spinning wave is constant. For a standing wave, in a) one observes that different azimuthal positions experience different amplitudes of fluctuating pressure. This can be checked with R^{st} in b), where the amplitude of R^{st} is zero at the position of the pressure nodes in a).

We decide, instead of studying all the possible standing waves with various orientations in a fixed frame of reference, to study each standing wave in an ad-hoc rotated frame of reference where $A_1 = A_2$. This means that at $\theta = \pi/4$ the mode has a pressure anti-node. By varying the value of ζ in (4.2), we can choose to study a wave with a pressure anti-node at different positions, as discussed below equation (4.2).

We then evaluate the structure of $R_j(A_1, A_2, \varphi)$ by substituting the expressions (4.42a) into (4.40). We obtain

$$R_j^{st} = A\sqrt{1 + \sin(2\theta_j)} = \sqrt{2}A|\cos(\theta_j - \pi/4)| \tag{4.47}$$

The amplitude R is maximum at $\theta_j = \pi/4$, where pressure anti-nodes are located, and zero at pressure nodes. This can be observed in Figure 4.1.b, which shows the pressure amplitude of oscillation R with a red line as a function of θ. This means that the burners experience a harmonic pressure fluctuation with amplitude R_j that depends on their position in the annulus. The maximum amplitudes of standing and spinning waves are obtained from equations (4.44) and (4.47). They are trivially

$$\begin{cases} R_{max}^{sp} = & A^{sp} \\ R_{max}^{st} = & A^{st}\sqrt{2} \end{cases} \tag{4.48}$$

4.3.3 Amplitudes of standing and spinning solutions

In this section we discuss the existence and the amplitude A of standing and spinning waves as limit-cycles of (4.33), i.e. fixed points of (4.39). We then discuss separately the two cases of spinning (4.42b) and standing waves (4.42a).

The following implication holds for all values of ζ considered in (4.2):

$$f_{A_1}(A, A, k\pi/2) + f_{A_2}(A, A, k\pi/2) = 0 \;\Rightarrow\; (A, A, k\pi/2) \text{ is a fixed point of (4.39)} \tag{4.49}$$

The proof, discussed in the appendix in §4.7.2, exploits the symmetries of the equations and does not add physical insight in the problem.

We were not able to prove that the solutions with coordinates $(A, A, k\pi/2)$, which can be calculated with (4.49), plus the solutions due to the rotational symmetry of the system are all the possible fixed points of (4.39). It is in general hard to determine all the fixed points of a nonlinear dynamical system, in this case in three dimensions. In all the following we will assume that there are no other solutions. In all the cases

studied we could not numerically find any other fixed points, and the system did not converge to other solutions in the time domain.

4.3.3.1 Spinning solution

We look for spinning solutions, which are fixed points of the slow flow (4.39). We substitute the definition (4.42b) of a spinning wave and the corresponding slowly varying amplitude R_j from (4.44) into the criterion (4.49), obtaining

$$F^{sp}(A) = \alpha \tag{4.50}$$

where we introduce

$$F^{sp}(A) \equiv \frac{N_b}{2}\mathrm{Re}\left[Q(A,\omega)\right] \tag{4.51}$$

In the following we denote with A^{sp} a solution of (4.50), which is the amplitude of a spinning solution.

Notice how $\mathrm{Re}\left[Q(A,\omega)\right] = G(A,\omega)\cos\phi(A,\omega)$ is the component of the fluctuating heat release rate that is in phase with the pressure p. It is possible to prove that the condition (4.50) can be obtained from the Rayleigh criterion for a spinning wave:

$$\int_\Omega \int_0^{2\pi/\omega} \left[q(\boldsymbol{x},t)p(\boldsymbol{x},t) - \alpha p(\boldsymbol{x},t)\right] p(\boldsymbol{x},t)dt\, d\Omega = 0 \;\;,\;\; p(0,\overline{r},\theta,t) = A\cos(\omega t - \theta) \tag{4.52}$$

where the equation enforces a zero energy balance in one cycle of oscillation. We however stress that the Rayleigh criterion is not sufficient to characterize the problem, because in (4.52) we are imposing a specific solution for the pressure field, which is a result of the current analysis.

Since the gain G of the describing function is bounded, the function $F^{sp}(A)$ is a bounded function of the amplitude too. This means that depending on the value of the acoustic damping coefficient α there can be zero, one or more solutions. This will be discussed further in §4.3.4.1.

4.3.3.2 Standing solution

We look for standing solutions, which are fixed points of the slow flow (4.39). We substitute the definition (4.42a) of a standing wave and the corresponding slowly

varying amplitude R_j from (4.47) in the criterion (4.49), obtaining

$$\alpha A = + \frac{1}{2}\sum_{j=1}^{N_b}\left[(c_j^2+s_j^2)A + 2c_j s_j A\right]\cos\phi\left(A\sqrt{1+\sin(2\theta_j)},\omega\right)G\left(A\sqrt{1+\sin(2\theta_j)},\omega\right)$$

We collect A, and substitute (4.47) to obtain

$$\alpha = \frac{1}{2}\sum_{j=1}^{N_b}(1+\sin(2\theta_j))\cos\phi\left(A\sqrt{1+\sin(2\theta_j)},\omega\right)G\left(A\sqrt{1+\sin(2\theta_j)},\omega\right) \tag{4.53}$$

we can define the RHS of (4.53) as

$$F^{st}(A) \equiv \frac{1}{2}\sum_{j=1}^{N_b}(1+\sin(2\theta_j))\,\mathrm{Re}\left[Q\left(A\sqrt{1+\sin(2\theta_j)},\omega\right)\right] \tag{4.54}$$

so that equation (4.53) becomes

$$F^{st}(A) = \alpha \tag{4.55}$$

In the following we denote with A^{st} a solution of (4.55), which is the amplitude of a standing solution. Similar to the spinning solutions, $F^{st}(A)$ is a bounded function. Depending on the value of the acoustic damping coefficient, α, there can be zero, one or more amplitudes, A, that are solutions of (4.55). This will be discussed further in §4.3.4.2. One can also prove that

$$\max\left\{F^{st}(A)\right\} \leq \max\left\{F^{sp}(A)\right\} \tag{4.56}$$

4.3.3.3 Orientation of standing solutions

It is here useful to define *equivalent* solutions as solutions that can be obtained from each other by applying symmetry operations. These *equivalent* solutions share the same amplitude of oscillation, stability properties, nonlinear oscillation frequency and heat release rate pattern. We also introduce the concept of *distinct* solutions, as solutions that cannot be obtained from each other by applying symmetry operations. One can determine all the non-identical solutions of the system by first determining all the distinct solutions, and then obtain N_b more from each of them, by rotating each by $k\Delta\theta$, $k = 1, \ldots N_b - 1$, obtain $N_b - 1$ more solutions. One must be cautious however, because the rotation may map a distinct solution to itself. It follows that the total

number of non-identical solutions will be the number of *distinct* solutions p and all their *equivalent* non-identical solutions.

We follow this strategy and look for the distinct solutions constraining ζ to the set of values $\{0, 2\}$ if the number of burners N_b is even, and constraining ζ to the set of values $\{0, 1, 2, 3\}$ if N_b is odd. By doing so, we are looking for standing solutions that present a pressure anti-node at $\theta = \pi/4$ within a fixed segment of the annulus, as discussed in (4.2). The coefficient ζ is then a physical parameter, which describes the position of the pressure anti-node of the solution we are looking for. We choose only these positions, i.e. values of ζ, because we can prove the theorem (4.49) only for these cases. It is however much easier to understand this by sketching the velocity nodal line, i.e. the diameter on which the velocity nodes of the standing mode lie, of these solutions. We present the possible orientations of the standing solutions for the two cases of N_b even and odd in Figure 4.2.

For the following argument we assume that one standing wave with a pressure antinode at one burner position is a solution, and we refer to Figure 4.2. We look for this solution using equation (4.55) by setting $\zeta = 0$.

If the number of burners N_b is even, each burner is diametrically opposite another burner (the black line in Figure 4.2.a). Because of the rotational symmetry, two standing modes that are just one burner apart are equivalent solutions and will be both stable/unstable. We find that for this system there is only one unstable manifold between them, which is respectively unstable/stable. On such a manifold there can be another solution (the gray line) and because of the symmetry of the system this other solution is exactly half-way between the two equivalent solutions, and can be studied by setting $\zeta = 2$. For N_b even, the rotations of $k\Delta\theta,\ k = 1, \ldots, N_b/2 - 1$ do not map a solution to itself, so the total number of non-identical solutions is the number of distinct solutions found with $\zeta = 0$ and then with $\zeta = 2$ (if any), multiplied by $N_b/2$.

If the number of burners N_b is odd, each burner is diametrically opposite a space between two burners. As a consequence, and because of the rotational symmetry, two equivalent standing modes in this case are just a half-burner apart, and they will be both stable/unstable. The reasoning of the previous paragraph applies here as well, so that there can be an additional solution between these two modes, corresponding to the solution of (4.55) for $\zeta = 1$. For N_b odd, certain rotations map some solutions to themselves; in particular the solutions found with $\zeta = 0$ are equivalent to the solutions found with $\zeta = 2$, and the solutions found with $\zeta = 1$ are equivalent to the solutions found with $\zeta = 3$. The total number of non-identical solutions is the number of distinct solutions found with $\zeta = 0$ and then with $\zeta = 1$ (if any), multiplied by N_b.

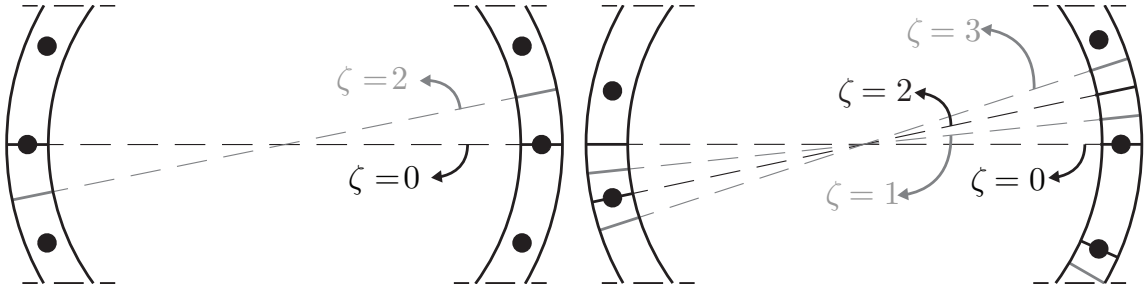

(a) $N_b = 16$ (b) $N_b = 15$

Fig. 4.2 Position of the velocity nodal lines of all possible standing waves in a section of annular combustor with equispaced burners. The physical coefficient ζ defines the orientation of the velocity nodal line. The velocity nodal lines link two pressure antinodes, and only the lines fully contained in this view are reported. The burners are represented with large black discs, and the semicircles are the internal and external walls of the chamber. In a) the number of burners N_b is even and each burner faces another burner on the other side of the annulus. in the angle $\Delta\theta = 2\pi/N_b$ we have one black and one gray line for a total of 2 standing waves for each burner. In b) the number of burners is odd, and each burner faces the space between two other burners on the other side of the annulus. There are a total of 4 standing waves for each burner. Nonetheless, we can count them only in $[0\,,\,\pi)$, as the modes repeat themselves after a rotation of π.

The same argument applies if one assumes that one standing wave with a pressure antinode just between two consecutive burners is a solution. Notice that we are not stating that all the standing modes with these orientations necessarily exist, but that if they exist they have these orientations. Their existence depends strongly on the considered problem, as §4.4 will exemplify.

These results are consistent with the standing modes observed in the MICCA annular combustor at the laboratoire EM2C (Ecole Centrale Paris), equipped with sixteen burners. When the burners are of the swirl type, the pressure field is quite noisy, but the nodal line exhibits a preferential position between two burners (Bourgouin et al., 2013). When equipped with matrix burners, the system is less noisy and the velocity nodal line stays again between two burners (Bourgouin, 2014; Durox et al., 2013).

The tendency of standing modes of preferring these fixed orientations disappears for a large number of burners, as will be proved in §4.3.4.2. The nodal lines of the modes then take an arbitrary orientation and move at the speed of the mean azimuthal velocity if non-zero, as observed in the simulations of Wolf et al. (2010).

4.3.4 Stability of standing and spinning solutions

The previous section investigated the amplitudes of standing and spinning solutions. This and the next section discusses the stability of these solutions, and presents implications for experiments/simulations and industrial applications. We are here discussing the stability of periodic solutions of the equations (4.33), which are fixed points of (4.39). By evaluating the eigenvalues of the Jacobian of these fixed points we can establish necessary and sufficient conditions for the stability of the periodic solutions. This can be done analytically, as discussed in §4.7.5 of the appendix, and results in necessary and sufficient conditions for the stability of the solutions. Consistently with the system having three variables, we find three eigenvalues and require all three growth rates to be negative in order for the solution to be an attractor.

4.3.4.1 Stable spinning solutions

We prove in §4.7.6 of the appendix that for the case of a spinning solution two of the three conditions are trivially satisfied when the third condition is satisfied, which is:

$$\mathrm{Re}\left[Q'(A^{sp},\omega)\right] <0 \tag{4.57}$$

where the prime indicates the derivative of the describing function Q with respect to the amplitude A of oscillation, and the quantity is calculated at the amplitude A^{sp} of a spinning solution, i.e. at one solution of (4.50).

A spinning solution with amplitude A^{sp} is stable if and only if (4.57) is respected. Notice that this condition could be obtained by differentiating the Rayleigh criterion with respect to the amplitude A (see (4.51) and (4.52)). It follows that the condition (4.57) requires the flame response to be weaker than the damping at amplitudes larger then A^{sp}, and stronger than the damping at amplitudes smaller then A^{sp}. This is the same criterion for a stable thermoacoustic limit-cycle in longitudinal configurations.

Moreover, notice that, since the inequality (4.56) holds, if one assumes that: *1)* the flame does not extinguish, (i.e. the describing function is defined and continuous at all amplitudes); *2)* the gain of the describing function eventually decreases with amplitude; *3)* the damping is not large enough to make the system globally stable (granted in all cases of interest); then there necessarily exists a stable spinning solution, whatever flame response is assumed.

4.3.4.2 Stable standing solutions

We start with discussing the existence of standing solutions, regardless of their stability. We find that the three conditions described at the end of §4.3.4.1 are not sufficient for the existence of standing solutions: there can be values of the damping α where one can find solutions A^{sp} of equation (4.50), but cannot find solutions A^{st} of equation (4.55), because the maximum value of $F^{st}(A)$ is smaller or equal to the maximum value of $F^{sp}(A)$, as reported in equation (4.56). This is exemplified later in Figure 4.6.

There are three necessary and sufficient conditions for the stability of a standing solution with amplitude A^{st}. The mathematical proof of the expressions discussed in the following can be found in §4.7.7 of the appendix

Before discussing each of the conditions, we discuss two general points. Firstly, if two conditions are respected, and the other condition results in $0 > 0$, the system is neutrally stable, with two negative and one zero growth rates. Secondly, if not all the conditions are respected, but at the same time one or two of them are, the standing solution will attract the state of the dynamical system on a certain manifold of the 3D phase space, and it will repel it on another. In other words, the standing solution will be a saddle of the problem, as first observed by Schuermans et al. (2006) for a fixed heat release rate model. This serves as a warning to any interpretation of noisy experimental and simulation data, which must take into account that standing solutions can be attractors and repellors, but also saddles of the system, so that the observed state of the system can linger for long times in the vicinity of a standing mode without necessarily implying that the standing mode is a stable solution.

We study the three conditions separately in §4.3.4.2.1, §4.3.4.2.2 and §4.3.4.2.3. We will discuss the physical meaning of the second and third condition by considering the asymptotic limit $N_b \to \infty$ while keeping the product βN_b constant, so that the overall flame response of the combustion chamber stays constant as well. In such case, the summations can be replaced by integrals in θ over the domain $[0\,,\,2\pi)$, and we recover a distributed heat release rate model employed in some articles on the theoretical modelling of annular combustors (Ghirardo and Juniper, 2013; Noiray et al., 2011; Schuermans et al., 2006). From a physical perspective, this asymptotic limit is reached in combustors that have a large number of burners around the annulus.

4.3.4.2.1 Rayleigh condition The first condition for stable standing modes is

$$F^{st\prime}(A^{st}) < 0 \tag{4.58a}$$

where the prime indicates the first derivative of F^{st} with respect to the amplitude of oscillation A, defined in (4.54). The condition follows exactly the same interpretation as the only condition (4.57) for the spinning solution: if a standing mode is stable, at amplitudes larger then A^{st} the damping losses are larger than the energy gains. As for the spinning solution, this can be explained by considering the derivative of the Rayleigh criterion with respect to the amplitude A^{st} of oscillation.

4.3.4.2.2 Orientation condition The second condition for stable standing modes is:

$$\begin{aligned}
&\left[\sum_{j=1}^{N_b} c_j s_j \mathrm{Re}\left[Q(A^{st}\sqrt{1+2c_j s_j},\omega)\right] - A^{st}\frac{1}{4}\sum_{j=1}^{N_b}\frac{(c_j^2-s_j^2)^2}{\sqrt{1+2c_j s_j}}\mathrm{Re}\left[Q'(A^{st}\sqrt{1+2c_j s_j},\omega)\right]\right]\times \\
&\left[\sum_{j=1}^{N_b} c_j s_j \mathrm{Re}\left[Q(A^{st}\sqrt{1+2c_j s_j},\omega)\right]\right] + \left[\sum_{j=1}^{N_b} c_j s_j \mathrm{Im}\left[Q(A^{st}\sqrt{1+2c_j s_j},\omega)\right]\right]\times \\
&\left[\sum_{j=1}^{N_b} c_j s_j \mathrm{Im}\left[Q(A^{st}\sqrt{1+2c_j s_j},\omega)\right] - A^{st}\frac{1}{4}\sum_{j=1}^{N_b}\frac{(c_j^2-s_j^2)^2}{\sqrt{1+2c_j s_j}}\mathrm{Im}\left[Q'(A^{st}\sqrt{1+2c_j s_j},\omega)\right]\right] > 0
\end{aligned} \tag{4.58b}$$

For a large number of burners this condition simplifies to $0 \geq 0$ as proved in §4.7.7.2, where it is reinterpreted as a condition for neutral stability. This means that the standing mode will be indifferent to a shift of the fixed point in a certain direction, which is a rotation of the nodal line of an arbitrary angle in the azimuthal direction, like a marble subject to gravity on a horizontal flat surface. This is a known feature of standing solutions in models with distributed heat release rate, discussed in chapter §2. On the other hand, for a finite number of burners we have a fixed number of possible positions of the nodal lines as discussed in §4.3.3.3, and the condition (4.58b) discusses if a certain family of equivalent standing solutions is stable/unstable in the azimuthal direction (see Figure 4.2).

4.3.4.2.3 Standing pattern condition The third condition for stable standing modes is

$$\begin{aligned}
&\sum_{j=1}^{N_b} c_j s_j \mathrm{Re}\left[Q(A^{st}\sqrt{1+2c_j s_j},\omega)\right] - \quad \dots \\
&\qquad \dots A^{st}\frac{1}{8}\sum_{j=1}^{N_b}\frac{(c_j^2-s_j^2)^2}{\sqrt{1+2c_j s_j}}\mathrm{Re}\left[Q'(A^{st}\sqrt{1+2c_j s_j},\omega)\right] > 0
\end{aligned} \tag{4.58c}$$

For a large number of burners this condition simplifies to (proved in §4.7.7.1):

$$N_2 \equiv \int_0^{2\pi} \mathrm{Re}\left[Q(A^{st}\sqrt{1+\sin(2\theta)},\omega)\right]\sin(2\theta)d\theta > 0 \tag{4.59}$$

We recall that $Q(A,\omega)$ is the describing function of the flame response to a harmonic input of pressure amplitude A, and ω is the frequency of the standing solution. The argument $A^{st}\sqrt{1+\sin(2\theta)}$ is the spatial distribution of the pressure amplitude of oscillation of the standing solution appearing in red in Figure 4.1.b.

Before discussing further the condition (4.59), we recall from Noiray et al. (2011) the quantity:

$$C_{2n} = \int_0^{2\pi} \mathrm{Re}\big[Q_\theta(0,\omega)\big]\sin(2n\theta)d\theta \tag{4.60}$$

We use here a slightly different notation and definition of C_{2n} for simpler comparison with the conventions adopted in this chapter, though the same exact role and meaning holds. This coefficient C_{2n} is the harmonic at 2θ of the linear heat release rate response along the annulus, and n is the azimuthal wavenumber of the oscillation. In the integral (4.60) the linear response Q_θ depends directly on the azimuthal angle θ, because it models a variation of the linear gain of the flames along the annulus. In particular Noiray et al. (2011) consider a simple heat release rate model $q_\theta(p) = \beta(\theta)p - p^3$, and prove that:

1. for a rotationally symmetric chamber $C_{2n} = 0$ the system stabilizes towards a spinning solution;

2. for small asymmetry in the $2n\theta$ component, i.e. for intermediate values of C_{2n}, the system stabilizes to a mixed spinning/standing mode;

3. for large asymmetry, in the $2n\theta$ component, i.e. large values of C_{2n}, the system stabilizes to a standing mode.

The coefficient C_{2n} is a linear property of the system (because it describes the azimuthal variation of the transfer functions of the flames, which are linear operators): only the specific loss of rotational symmetry in the 2θ component affects the nature of the solutions.

This chapter focuses on rotationally symmetric configurations, where C_{2n} is fixed to zero, and keeps the flame response arbitrary. Nonetheless, N_2 introduced in (4.59), and its generalization N_{2n}, have strong analogies to C_{2n}.

N_{2n} is measured on the limit-cycle with amplitude A^{st}, and it is the $2n\theta$ component of the nonlinear, amplitude dependent gain $\mathrm{Re}[Q]$ that affects the stability of standing modes. For a large number of burners, a standing solution always respects the first and the second condition, the latter in a marginally stable sense. It follows that if the third condition $N_{2n} > 0$ is respected, the solution is stable, and vice-versa if $N_{2n} < 0$ the solution is unstable.

It is easy to prove that for the specific heat release model $q(p) = \beta p - p^3$ proposed by Noiray et al. (2011), N_{2n} is negative and one recovers their results, that in rotationally symmetric chambers standing solutions are not stable attractors for a cubic flame response without delay. On the other hand, one should make use of C_{2n} to predict the stability of standing modes only if the flame response is quite similar to $q(p) = \beta p - p^3$. In the example presented in §4.4 we have for example that $C_{2n} = 0$ and $N_{2n} > 0$, i.e. standing solutions are stable attractors.

In experiments, one can measure N_{2n} for an observed, stable standing mode simply as

$$N_{2n} = \int_0^{2\pi} \mathrm{Re}[Q_\theta^{\mathrm{st}}] \sin(2n\theta) d\theta \tag{4.61}$$

where the frame of reference is chosen such that $p(t)$ has a pressure anti-node at $\theta = \pi/4$, and $\mathrm{Re}[Q_\theta^{\mathrm{st}}]$ is the real part of the transfer function between the local heat release rate and the local pressure fluctuation, calculated from the data of a self-excited annular combustor experiencing a stable standing mode with azimuthal wavenumber n.

In many cases the describing function phase does not vary strongly with amplitude. Moreover, a favourable (q being quite in phase with p) phase lag in the linear regime is also often required to observe a thermoacoustic instability. Under these circumstances, it is reasonable to assume that the real part does not change sign with amplitude. Under this restrictive assumption, and noticing that $\sin(2n\theta)$ spans from -1 at pressure nodes to $+1$ at pressure anti-nodes, a flame responding with a strong gain at small amplitudes (close to pressure nodes) and with a weak gain at large amplitudes (close to pressure anti-nodes) will lead to a negative overall integral, and standing modes will not be attractors of the problem. The example presented in §4.4 lends itself to this interpretation.

This subsection showed that there are three conditions for stable standing modes: the first one corresponds to an energy balance stability, which can be interpreted with the Rayleigh criterion. The second condition discusses the stability of the orientation of the standing mode, and disappears for a large number of burners. The third condition discusses the stability of the standing wave pattern.

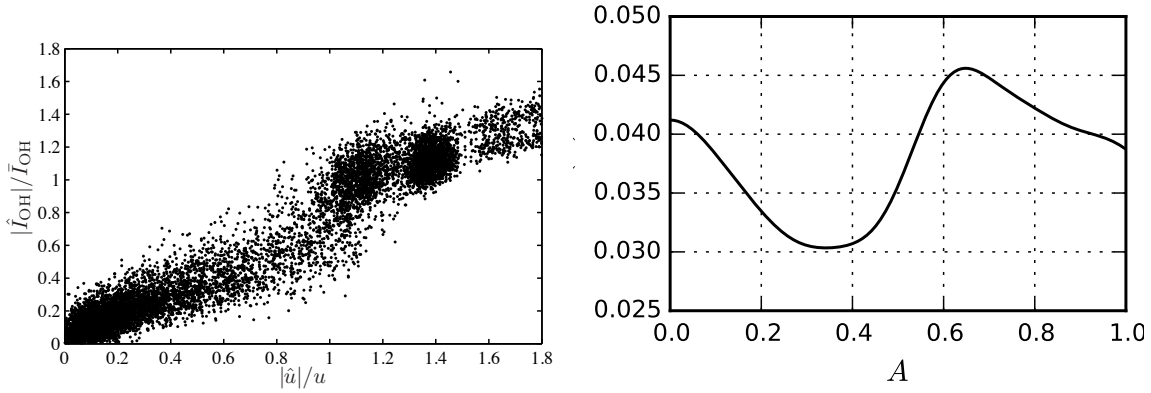

(a) instantaneous flame response (b) extracted gain of the flame response

Fig. 4.3 a) instantaneous amplitudes of the dominant Fourier component of OH-chemiluminescence and of the longitudinal velocity at the burner's position, taken from Moeck et al. (2008). b) Gain modelled. For $A \in [0\ 1]$, the gain was extracted using equation (4.62). The result has then been scaled in both horizontal and vertical axes.

4.4 Triggering in annular combustors

In this section we apply the framework developed in the previous chapters to an annular combustor with an elaborate flame response. In particular this combustor can exhibit thermoacoustic triggering, and to the knowledge of the authors this is the first theoretical study of the phenomenon in annular combustors. The reader can refer to Lepers et al. (2005) for a discussion of triggering in an experimental industrial annular test-rig.

In this example we focus on the effect of the gain. To isolate this effect, we fix the dependence of the phase lag ϕ to be constant, $\phi = \pi/5$. To make the example more compelling, we use as flame response the data from Moeck et al. (2008), which is an experimental and modelling study of a system exhibiting thermoacoustic triggering in a longitudinal test-rig. The instantaneous spatially-integrated OH-chemiluminescence response of the experiment is shown with black dots for a run of the experiment in Figure 4.3.a, as a function of the longitudinal velocity at the burner. Notice how the response is linear at low amplitudes, then drops between 0.5 and 0.8, and regains strength at amplitudes at around 1. We assume that the heat release rate response is proportional to the OH-chemiluminescence, and extract the gain of the response as

$$G(\hat{u}/u) = \frac{|\hat{I}_{OH}|/\bar{I}_{OH}}{|\hat{u}|/\overline{u}} \tag{4.62}$$

Under the hypothesis of acoustically compact burners, $G(A) \propto G(\hat{u}/u)$, where A is the amplitude of oscillation of the pressure at the burner's location in the chamber. We arbitrarily scale the argument A so that it is in the range $[0\,,\,1]$, because the linear operator between pressure in the chamber and longitudinal velocity in the burner discussed in §4.2.2 is unknown.

We also scale the value of $G(A)$ to account for typical growth-rates values of annular combustors in nondimensional frequency units, obtained from experimental data, using the relation (4.32), where we fix the number of burners N_b to six for a first example. The details of this scaling are discussed in §4.7.8 of the appendix.

We then study two combustors with $N_b = 6$ burners that differ only in the amount of acoustic damping $\alpha_1 = 0.085$ and $\alpha_2 = 0.105$. The amplitudes of the spinning and standing solutions are the solutions of the equations (4.50,4.55). We study these equations as a function of the maximum amplitude R_{max}, in time and space, as introduced in equation (4.48). We present in Figure 4.4.a: *1)* the function $F^{sp}(R_{max})$ in blue to discuss spinning modes; *2)* the function $F^{st,0}(R_{max})$ in red, to discuss standing modes with a pressure anti-node at the location of one burner ($\zeta = 0$); *3)* the function $F^{st,2}(R_{max})$ in magenta, to discuss standing modes with a pressure anti-node located exactly between two consecutive burners ($\zeta = 2$).

The solutions are the intersections of these curves with the horizontal dashed and dashed-dotted black lines at the two ordinates α_1, α_2. We use the conditions (4.57,4.58) to discuss the stability of the solutions, and mark with a filled/empty circle solutions that are respectively stable/unstable.

Before discussing these solutions, we introduce two critical values of damping, reported in Figure 4.4.a with two horizontal black lines:

$$\alpha_l \equiv F^{sp}(0) = F^{st,\zeta}(0) \tag{4.63}$$

$$\alpha_h \equiv \max\{F^{sp}\} \tag{4.64}$$

Notice that we do not have data about the flame response at amplitudes larger than 1.4 from Figure 4.3.b. We assume that the response decreases monotonically with amplitude there when we calculate α_h in (4.64). We can define three ranges of study for the acoustic damping coefficient α:

1. if $\alpha < \alpha_l$ the fixed point is linearly unstable. In fact, one can show that α_l, which is the value of the definitions (4.51) and (4.54) at $A = 0$, is equal to the term $N_b\beta\cos\tau/2$ that was introduced in the linear analysis at the end of §4.2.5. Then

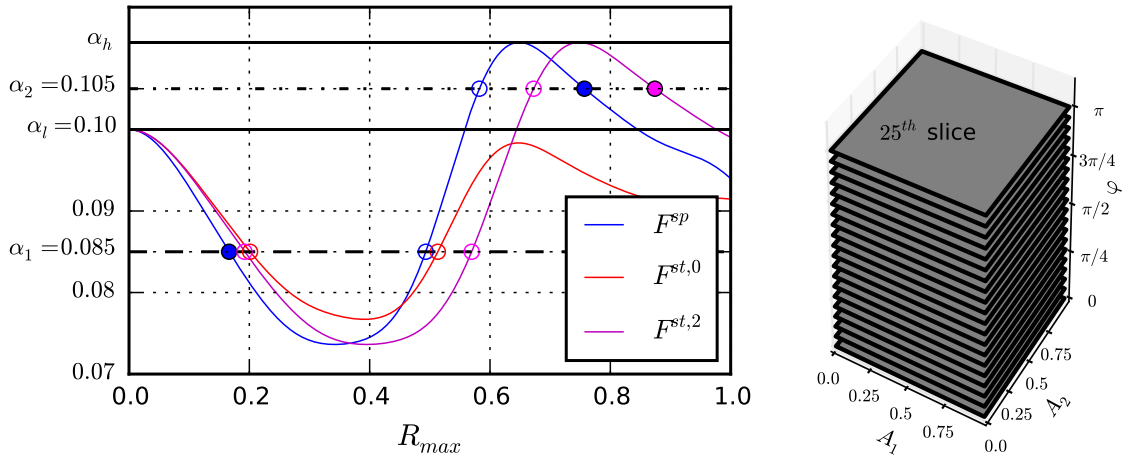

(a) analysis of the solutions (b) slices of the phase space

Fig. 4.4 a) Amplitude of oscillation R_{max} of spinning (blue) and standing (red/magenta) solutions for a combustor equipped with six burners. We consider two combustors that differ only in the acoustic damping coefficient α, presented with the two dashed and dashed dotted lines. The solutions are circles, which are filled/empty if the solution is stable/unstable. (b) sketch of the equi-spaced slices of the phase space at constant values of $\phi = k\pi/25$, for $k = 0, \ldots, 24$ presented in Figure 4.5.

the condition $\alpha < \alpha_l$ simply imposes that the growth-rate σ introduced in (4.32) is positive, i.e. that the thermoacoustic system is linearly unstable

2. if $\alpha_l < \alpha < \alpha_h$ the fixed point is linearly stable, but there exist standing and spinning solutions at large amplitudes of oscillation. The system is bistable and, with a suitable disturbance, is capable of triggering;

3. if $\alpha > \alpha_h$ the fixed point is linearly stable, and we cannot find standing or spinning solutions. The system is globally stable, in the sense that the damping is large enough to kill off thermoacoustic instabilities completely.

The first value of damping, α_1 in Figure 4.4.a, belongs to the first case, while the second value of damping, α_2, belongs to the second case. Notice how at $\alpha = \alpha_1$ there are six apparent solutions and only one of them is stable, and it is of spinning type. We say apparent because there must be at least three more solutions at amplitudes $R_{max} > 1$, but it is impossible to determine their amplitudes because we do not know what the flame response is at those values. On the other hand at $\alpha = \alpha_2$ there are two stable solutions, one of spinning and one of standing type.

It is important to point out that this analysis of the fixed points does not discuss the dynamics of the system, which take place in the 3D phase space (A_1, A_2, φ), which

depends on the value of the damping α. We unveil the dynamics of the problem for $\alpha = \alpha_2$ by cutting horizontally the phase space with 25 slices as clarified in Figure 4.4.b, and presenting the slices in Figure 4.5. The phase space is much richer and more complicated than in previous studies (Ghirardo and Juniper, 2013; Noiray et al., 2011). Depending on the initial condition, one can qualitatively track the state of the system following the in-plane streamlines of the flow and the colour for the vertical component. One can find the spinning and standing solutions (blue and magenta circles in figure 4.4.a) in the middle-center and top-left or bottom-right slice respectively, with the same colours. Notice how a non-zero phase lag leads to an oscillatory behaviour as the system converges to a solution. This can be observed looking at the colour of the vertical component as the system gets closer to a solution: it is positive on one side (pulling upwards) and negative (pushing downwards) on the other, meaning that the system will spiral towards the solution instead of converging to it monotonically, as found in previous models with a zero phase lag.

We can carry out the same analysis of Figure 4.4.a for any value of the damping α, as presented in Figure 4.6.a. We omit the horizontal lines corresponding to the different values of the damping, and we draw the functions F with a thick/thin line wherever the solutions are respectively stable/unstable. These are typical bifurcation diagrams, but with the damping as bifurcation parameter reported on the vertical axis. As expected, the acoustic damping coefficient α strongly affects the amplitude of the solutions, but it also affects the type of stable solutions. We can then generalize the analysis to any number of burners N_b, and do so by rescaling the gain of the flame response so that the product βN_b is constant. We present in Figure 4.6 the result for $6, 7, 8, 9$ burners, for an arbitrary value of the damping. We observe that the stability and the amplitudes of the standing modes are affected by the number of burners. This exemplifies the fact that the condition (4.61) is a good criterion to look at the stability of standing solutions only for large values of N_b, because the number of burners N_b affects the exact position of the burners along the annulus in the stability conditions (4.58b,4.58c).

The example of this section showed how a flame that responds with a small gain at low amplitudes (in the linear regime) and with a higher gain at larger amplitudes (closer to the saturated amplitude of a standing solution), can present stable standing solutions (filled magenta circle in Figure 4.4) because it respects the condition (4.58c).

Notice how this is just one example of a system exhibiting stable standing solutions, and we are not here implying that thermoacoustic triggering is a necessary condition for stable standing solutions to occur. We point out, without discussing the details,

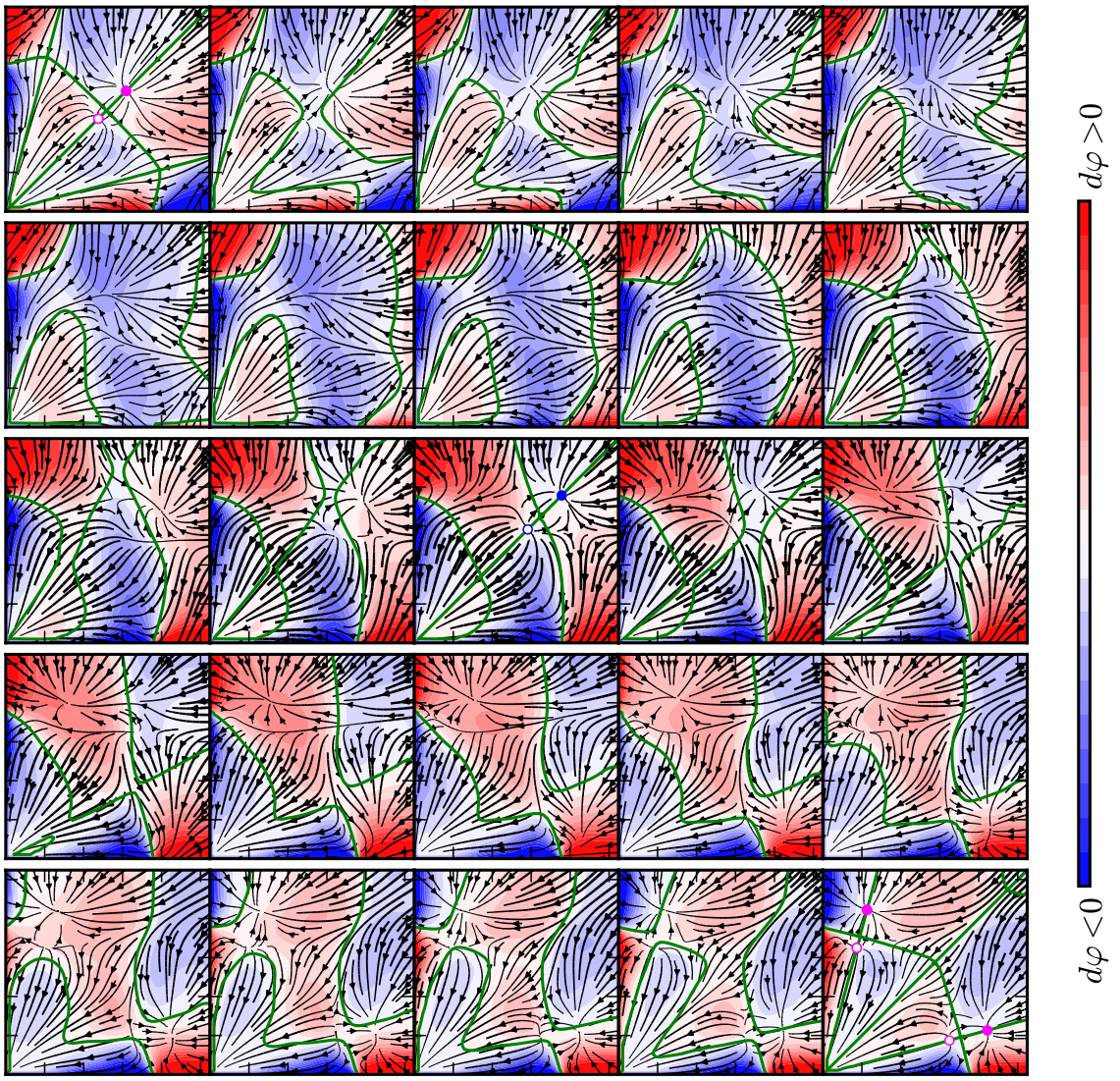

Fig. 4.5 25 slices of the phase space as presented in Figure 4.4.b, with the first slice in the top-left corner, ordered to the right and then to the bottom. This case is for six burners and for $\alpha = \alpha_2 = 0.105$ as presented in Figure 4.4.a. In each slice the figure axes are A_1 and A_2 from 0 to $\sqrt{2}$, with the point $(A_1, A_2) = (0, 0)$ in the bottom-left corner of each slice. The black streamlines represent the two in-plane components dA_1, dA_2 of the vector field, and the color represents the vertical component $d\phi$ (rescaled). The green lines are contours of $d\phi = 0$. Filled/empty circles are stable/unstable solutions. The top-left and the bottom-right square are at $\phi = 0$ and $\phi = \pi$, and present standing solutions. The slice in the middle is at $\phi = \pi/2$ and presents spinning solutions on the diagonal $A_1 = A_2$. The vector field was calculated directly from equations (4.39).

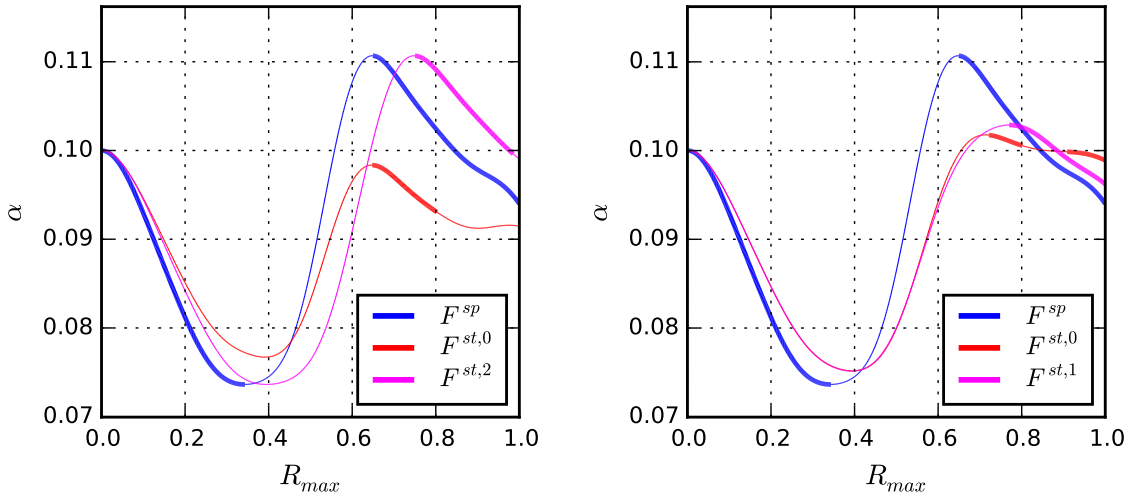

(a) $N_b = 6$ (b) $N_b = 7$

(c) $N_b = 8$ (d) $N_b = 9$

Fig. 4.6 Stability map as a function of the acoustic damping coefficient α. The number of burners N_b is different in each of the sub-figures. This analysis is a generalization of Figure 4.4.a for all values α. The lines are thick/thin if the respective solution is stable/unstable. There exist values of the damping α for which only spinning solutions exist, e.g. $\alpha = 0.105$ in d).

that we were able to obtain standing solutions as attractors with a flame response characterised by a monotonically decreasing gain, and a certain amplitude dependence of the phase lag. This is quite important when considering the annular test-rig *MICCA* developed at the laboratoire EM2C (Ecole Centrale Paris) when equipped with matrix burners, because the flames lift from the flame holder at large amplitude of excitation. This leads to a strong dependence of the phase lag with amplitude Bourgouin et al. (2014), while the gain decreases monotonically with amplitude.

4.5 Time domain validation

The results of the previous section can be compared with time domain simulations of the equations (4.33) of the two oscillators. This requires a time domain realization $\mathcal{Q}[p(t)]$ of the fluctuating heat release rate response as function of the pressure signal $p(t)$. The process of calculating the time domain realization $\mathcal{Q}[p(t)]$ of a given describing function $Q(A,\omega)$ is discussed in chapter §3. We only mention here that once the time-realization has been computed, it can be used as a black-box in any low-order, time domain thermoacoustic network (Pankiewitz and Sattelmayer, 2003; Schuermans et al., 2003; Stow and Dowling, 2009). The time domain results were in very good agreement (errors in amplitude of 1% for both standing and spinning solutions) for all cases in which the phase lag was set to zero. This validates the hypothesis of smallness of the forcing terms on the RHS of (4.33) in §4.3.1. However, the error increases for other cases with a non-zero phase lag, with the predicted amplitudes of the method of averaging being up to 10% smaller than the amplitudes obtained in time domain simulations. Saha et al. (2010) found a similar under-estimate of the amplitude when using the method of averaging on a delayed system. This is due to the fact that the frequency of oscillation changes slightly as a function of time and of the amplitude of oscillation, while the method of temporal averaging considers it fixed. We address this mismatch in Chapter §5, where we provide a dynamic equation for the temporal evolution of the frequency of oscillation.

4.6 Conclusions

We discuss azimuthal thermoacoustic oscillations in rotationally symmetric annular combustors. The key assumptions of this work are: *1)* the flames are acoustically compact; *2)* there is no effect of transverse forcing and the flame responds only to longitudinal acoustic perturbation at the burner; *3)* only one degenerate pair of modes

of azimuthal nature oscillates; *4)* the system is weakly nonlinear, and the eigenmodes do not change much in the nonlinear regime.

If the describing function of a single flame is known, we show how to build a nonlinear dynamical system of a rotationally symmetric annular chamber containing N_b such flames, with the help of a Helmholtz solver or a thermoacoustic network model. It predicts how this annular system will behave: whether it can support azimuthal oscillations, at what amplitude and of which type (spinning or standing), and whether or not they are stable.

The amplitude of spinning solutions is fixed by the Rayleigh criterion at the limit-cycle, and the same criterion provides also the necessary and sufficient condition for stable spinning solutions: the energy balance must be negative at larger amplitudes of oscillation. This is exactly the same as in the case of thermoacoustic oscillations in longitudinal configurations. We also prove that if the system is not globally stable, i.e. can exhibit a thermoacoustic oscillation, there exists at least one stable spinning solution.

The amplitude of standing solutions is also fixed by the Rayleigh criterion at the limit-cycle. In the same way valid for the spinning solution, the Rayleigh criterion provides one necessary stability condition for stable standing solutions. There are however two more conditions required to stabilize standing solutions:

1. The condition (4.58c) discusses the stability of a standing mode with respect to a rotation of its velocity nodal line in the azimuthal direction. This condition disappears for a large number of burners N_b because then every azimuthal orientation is allowed for standing solutions;

2. Another condition fixes a constraint on the spatial distribution of the heat release rate, as detailed by equation (4.59) in terms of its describing function Q calculated in terms of the pressure, and of the pressure amplitude A^{st} of the standing mode at the burners' position. We show that the azimuthal Fourier component 2θ of the part of the flame response in phase with the pressure in a limit-cycle of a standing solution is the most stringent condition for a large number of burners N_b. If this component is positive there exist stable standing solutions. This conjecture can be tested from experimental data of stable standing solutions to validate the hypotheses of this theory. This condition has a simple interpretation if $\mathrm{Re}[Q]$ is positive and stays positive at all amplitudes: we find that a flame with a small nonlinear gain close to pressure nodes and a large nonlinear gain close to pressure antinodes leads to stable standing solutions.

We show that care must be taken when processing experimental or simulation data: we prove that if the number of burners is large and a standing solution is not stable, then the solution is necessarily a saddle of the system, so that it can attract the state of the system for a certain period of time and from a certain direction, before pushing it towards the stable spinning solution. This means that it will be discern discuss the stability of standing solutions in the data, especially if it regards a noisy experiment or a numerical simulation with a limited duration.

We then present an example of the analysis that shows that an annular combustor capable of thermoacoustic triggering can present stable standing solutions. We predict amplitudes and stability of the spinning and standing solutions, parametrically in the acoustic damping coefficient α and in the number of burners N_b of the combustor. The dynamics of the system are very rich, and the phase space of the problem is strongly influenced by the nonlinear flame response, and particularly by a non-zero phase lag between the pressure and the heat release rate.

We obtained some general implications regarding standing modes. Their occurrence as a stable state of the system: *1)* when the combustor is rotationally non-symmetric; *2)* when the flame response respects the standing pattern condition (4.59); *3)* when there are other physical mechanisms, such as for example transverse forcing, dynamical temperature effects, or the effect of a mean azimuthal flow on the flame response; or *4)* with the onset of other acoustic modes, leading to scenarios of nonlinear mode-to-mode interaction and/or mode synchronisation, that are not considered in this chapter.

Future work should focus on studying to what extent the shape of the standing modes is affected in the nonlinearly saturated limit-cycle, to validate the truncation of the equations. One could also include the effect of transverse velocity in the flame model, and discuss how it affects the system in broader generality. Another important direction of investigation regards the discussion of the effect of noise on this framework, and how it affects the double Hopf bifurcation and the multi-stable character of the system. Finally, one can study what happens to a combustor that shows a certain degree of asymmetry, so that in the nonlinear regime the linear effects due to the asymmetry and the nonlinear response of the flames will compete.

4.7 Appendices

4.7.1 Averaging with describing functions

This appendix shows how to evaluate the expressions (4.38) for $k = 1$, with the case $k = 2$ following similarly. We substitute the definition of f_1 from (4.34a), and consider

only the j-th term of the summation in (4.38):

$$\frac{c_j}{2}\frac{1}{\pi/\omega}\int_0^{2\pi/\omega}\mathcal{Q}\left[A_1c_j\cos(\omega t+\varphi_1)+A_2s_j\cos(\omega t+\varphi_2)\right]e^{i(\omega t+\varphi_1)}dt \tag{4.65}$$

We introduce the first change of variables

$$\begin{cases} a_j = A_1c_j\cos\varphi_1 + A_2s_j\cos\varphi_2 \\ b_j = A_1c_j\sin\varphi_1 + A_2s_j\sin\varphi_2 \end{cases} \tag{4.66}$$

and the second change of variables

$$\begin{cases} a_j = R_j\cos\psi_j \\ b_j = R_j\sin\psi_j \end{cases} \qquad \begin{cases} R_j = \sqrt{a_j^2+b_j^2} \\ \psi_j = \arg\left(a_j+ib_j\right) \end{cases} \tag{4.67}$$

Notice that we can rewrite the definition of R_j by substituing the expression for a_j, b_j from (4.66), obtaining equation (4.40). We trigonometrically expand the argument of $\mathcal{Q}'$ in equation (4.65), and substitute first (4.66) and then (4.67). The expression (4.65) simplifies to

$$\frac{c_j}{2}\frac{1}{\pi/\omega}\int_0^{2\pi/\omega}\mathcal{Q}\left[R_j\cos(\omega t+\psi_j)\right]e^{i(\omega t+\varphi_1)}dt \tag{4.68}$$

We first change the time variable to $t\to t-\psi_j/\omega$ and then slide the interval of definition of the integrand because it is periodic. We obtain

$$\frac{c_j}{2}\frac{1}{\pi/\omega}\int_0^{2\pi/\omega}\mathcal{Q}\left[R_j\cos(\omega t)\right]e^{i(\omega t+\varphi_1-\psi_j)}dt \tag{4.69}$$

We then expand the complex exponential in the integrand, take the constants out of the integral, and divide and multiply by R_j:

$$R_je^{-i\psi_j}\frac{c_j}{2}e^{i\varphi_1}\left[\frac{1}{R_j}\frac{1}{\pi/\omega}\int_0^{2\pi/\omega}\mathcal{Q}\left[R_j\cos(\omega t)\right]e^{i\omega t}dt\right] \tag{4.70}$$

We now observe that the term in the outer square brackets is the describing function of $\mathcal{Q}$ defined in (4.4). From (4.67) we have that $R_je^{-i\psi_j} = a_j - ib_j$. The expression simplifies to

$$(a_j-ib_j)\frac{c_j}{2}e^{i\varphi_1}G(R_j,\omega)e^{i\phi(R_j,\omega)} \tag{4.71}$$

where we have rewritten the describing function $Q(R_j, \omega)$ in terms of gain G and phase response ϕ as presented in equation (4.5). This is the contribution of the j-th burner. The final expression of (4.38) is

$$\langle f_k \cos(\omega t + \varphi_k)\rangle + i\langle f_k \sin(\omega t + \varphi_k)\rangle = \sum_{j=1}^{N_b}(a_j - ib_j)\frac{c_j}{2}G(R_j,\omega)e^{i(\phi(R_j,\omega)+\varphi_k)} \tag{4.72}$$

The two averaged terms are the real and imaginary parts of (4.72). By substituting a_j, b_j from (4.66) we obtain:

$$\langle f_1 \cos(\omega t + \varphi_1)\rangle = +\frac{1}{2}\sum_{j=1}^{N_b} G(R_j,\omega)\left[A_1 c_j^2 \cos\phi(R_j,\omega) + A_2 c_j s_j \cos(\phi(R_j,\omega)+\varphi)\right] \tag{4.73a}$$

$$\langle f_1 \sin(\omega t + \varphi_1)\rangle = +\frac{1}{2}\sum_{j=1}^{N_b} G(R_j,\omega)\left[A_1 c_j^2 \sin\phi(R_j,\omega) + A_2 c_j s_j \sin(\phi(R_j,\omega)+\varphi)\right] \tag{4.73b}$$

Similary for $j = 2$ we obtain

$$\langle f_2 \cos(\omega t + \varphi_1)\rangle = +\frac{1}{2}\sum_{j=1}^{N_b} G(R_j,\omega)\left[A_2 s_j^2 \cos\phi(R_j,\omega) + A_1 c_j s_j \cos(\phi(R_j,\omega)-\varphi)\right] \tag{4.73c}$$

$$\langle f_2 \sin(\omega t + \varphi_1)\rangle = +\frac{1}{2}\sum_{j=1}^{N_b} G(R_j,\omega)\left[A_2 s_j^2 \sin\phi(R_j,\omega) + A_1 c_j s_j \sin(\phi(R_j,\omega)-\varphi)\right] \tag{4.73d}$$

Finally, by substituting (4.73) in (4.37), we obtain the slow flow equations (4.39).

4.7.2 Sufficient condition for the existence of fixed points

This appendix proves the implication (4.49). We first introduce some simple mathematical identities, and then provide the proof in §4.7.4.

4.7.3 Mathematical identities

The following properties hold for any function $f : \mathbb{R} \to \mathbb{R}$:

$$\sum_{j=1}^{N_b} c_j^2 f\left(R_j(A_2, A_1, -\varphi)\right) = \sum_{j=1}^{N_b} s_j^2 f\left(R_j(A_1, A_2, \varphi)\right) \tag{4.74a}$$

$$\sum_{j=1}^{N_b} \cos(2\theta_j) f(R_j) = 0 \qquad \forall\, \varphi\,,\ A_1 = A_2 \tag{4.74b}$$

$$\sum_{j=1}^{N_b} \sin(2\theta_j) f(R_j) = 0 \qquad \varphi = \pm\frac{\pi}{2}\,,\ A_1 = A_2 \tag{4.74c}$$

$$\sum_{j=1}^{N_b} c_j^2 = \sum_{j=1}^{N_b} s_j^2 = \frac{N_b}{2} \qquad , \qquad \sum_{j=1}^{N_b} c_j s_j = 0 \tag{4.74d}$$

where c_j and s_j are defined in (4.17)

4.7.4 Proof of (4.49)

The proof proceeds following these steps. In §4.7.4.1 we first prove that $f_\varphi(A, A, k\pi/2)$ is zero for all integer values of k. We then prove in §4.7.4.2 that $f_{A_1}(A, A, k\pi/2) - f_{A_2}(A, A, k\pi/2)$ is zero. It follows that if also $f_{A_1}(A, A, k\pi/2) + f_{A_2}(A, A, k\pi/2)$ is zero, as is the hypothesis of the implication, then the individual terms, $f_{A_1}(A, A, k\pi/2)$ and $f_{A_2}(A, A, k\pi/2)$ also have to be zero. Then, all the three functions $f_\varphi, f_{A_1}, f_{A_2}$ are zero, and the point $(A, A, k\pi/2)$ is therefore a fixed point.

4.7.4.1 First part: $f_\varphi = 0$

The function $f_\varphi(A, A, \varphi)$ is odd with respect to φ. It follows that $\varphi = 0$ is a zero of the function:

$$f_\varphi(A, A, 2k\pi) = 0 \ \forall k \in \mathbb{Z} \tag{4.75}$$

By direct substitution, we can show that (4.75) holds also at $\varphi = \pm\pi/2$ and $\varphi = \pi$:

$$f_\varphi(A, A, k\pi/2) = 0 \ \forall k \in \mathbb{Z} \tag{4.76}$$

We prove (4.76):

- for $\varphi = \pi/2$ by observing that R_j is independent of j. The expression becomes

$$f_\varphi(A, A, \pm\pi/2) = \frac{1}{2}\sum_{j=1}^{N_b}\left[\left(s_j^2 - c_j^2\right)\sin\phi\,(A,\omega) - 2c_j s_j\cos\phi\right] G\,(A,\omega) \tag{4.77}$$

  This equation (4.77) can be split into two summations of $\cos 2\theta_j$ and $\sin 2\theta_j$, which are zero when summed over $[0\,,\,2\pi]$ as can be deduced from (4.74d):

- for $\varphi = \pi$ in (4.76) we obtain

$$\begin{aligned} f_\varphi(A, A, \pi) =& \frac{1}{2}\sum_{j=1}^{N_b}\left(s_j^2 - c_j^2\right)\sin\phi(R_j,\omega)G\,(R_j,\omega) \\ =& -\frac{1}{2}\sum_{j=1}^{N_b}\cos(2\theta_j)\sin\phi\,(R_j,\omega)\,G\,(R_j,\omega) \end{aligned} \tag{4.78}$$

  This summation vanishes by applying the property (4.74b).

4.7.4.2 Second part: $f_{A_1} - f_{A_2} = 0$

We now prove that

$$f_{A_1}(A, A, k\pi/2) - f_{A_2}(A, A, k\pi/2) = 0\ \forall k \in \mathbb{Z} \tag{4.79}$$

1) for $\varphi = 0$ by direct substitution and by exploiting (4.74a); *2)* for $\varphi = \pi$, by direct substitution and exploiting (4.74a) for $A_1 = A_2$ in the resulting equation; for $\varphi = \pi/2$ by also applying (4.74c) twice. We also observe that

$$\begin{cases} f_{A_1}(A, A, k\pi/2) = & 0 \\ f_{A_2}(A, A, k\pi/2) = & 0 \end{cases} \Leftrightarrow \quad \begin{cases} f_{A_1}(A, A, k\pi/2) - f_{A_2}(A, A, k\pi/2) = & 0 \\ f_{A_1}(A, A, k\pi/2) + f_{A_2}(A, A, k\pi/2) = & 0 \end{cases} \tag{4.80}$$

This, together with (4.79) and (4.76) implies that

$$f_{A_1}(A, A, k\pi/2) + f_{A_2}(A, A, k\pi/2) = 0 \quad \Rightarrow \quad \boldsymbol{f}(A, A, k\pi/2) = 0 \tag{4.81}$$

4.7.5 Sufficient condition for the existence of fixed points

One can numerically calculate the amplitudes A^{st} of standing solutions from equation (4.55) and the amplitudes A^{sp} of spinning solutions from equation (4.50). We can then discuss the stability of these solutions by evaluating the eigenvalues of the Jacobian of

the system (4.39). If all eigenvalues are negative the point is an attractor, i.e. a stable solution. Since the eigenvalues are invariant with respect to a change of variables, we consider the new set of variables

$$\begin{cases} 2C = A_1 + A_2 \\ 2D = A_1 - A_2 \end{cases} \tag{4.82a}$$

$$\begin{cases} A_1 = C + D \\ A_2 = C - D \end{cases} \tag{4.82b}$$

This transformation maps the point $(A_1, A_2, \varphi) = (A, A, \varphi)$ to the point $(C, D, \varphi) = (A, 0, \varphi)$, and the reason we apply the transformation will be apparent later. By evaluating the time derivative of (4.82a) and substituting first (4.39) and then (4.82b), we obtain the slow flow in terms of the new variables:

$$\begin{aligned} C' = -\frac{\alpha}{2}C + \frac{1}{4}\sum_{j=1}^{N_b} [\Big((c_j^2 - s_j^2)D + C\Big) \cos\phi\left(R_j, \omega\right) + \\ c_j s_j (C - D) \cos\left(\phi\left(R_j, \omega\right) + \varphi\right) + c_j s_j (C + D) \cos(\phi\left(R_j, \omega\right) - \varphi)] G\left(R_j, \omega\right) \end{aligned} \tag{4.83a}$$

$$\begin{aligned} D' = -\frac{\alpha}{2}D + \frac{1}{4}\sum_{j=1}^{N_b} [\Big((c_j^2 - s_j^2)C + D\Big) \cos\phi\left(R_j, \omega\right) + \\ c_j s_j (C - D) \cos(\phi\left(R_j, \omega\right) + \varphi) - c_j s_j (C + D) \cos(\phi\left(R_j, \omega\right) - \varphi)] G\left(R_j, \omega\right) \end{aligned} \tag{4.83b}$$

$$\begin{aligned} \varphi' = \frac{1}{2}\sum_{j=1}^{N_b} \Bigg[\Big(s_j^2 - c_j^2\Big) \sin\phi\left(R_j, \omega\right) - \\ c_j s_j \left(\frac{C - D}{C + D} \sin(\phi\left(R_j, \omega\right) + \varphi) - \frac{C + D}{C - D} \sin(\phi\left(R_j, \omega\right) - \varphi)\right) \Bigg] G\left(R_j, \omega\right) \end{aligned} \tag{4.83c}$$

We can rewrite the system (4.83) in compact form, and study the gradients of f_C, f_D, f_φ at the position of the fixed points found in §4.3.3, to obtain the Jacobian matrix $\boldsymbol{J}$:

$$\begin{cases} C' &= f_C(C, D, \varphi) \\ D' &= f_D(C, D, \varphi) \\ \varphi' &= f_\varphi(C, D, \varphi) \end{cases} \qquad \boldsymbol{J} = \begin{bmatrix} \frac{\partial f_C}{\partial C} & \frac{\partial f_C}{\partial D} & \frac{\partial f_C}{\partial \varphi} \\ \frac{\partial f_D}{\partial C} & \frac{\partial f_D}{\partial D} & \frac{\partial f_D}{\partial \varphi} \\ \frac{\partial f_\varphi}{\partial C} & \frac{\partial f_\varphi}{\partial D} & \frac{\partial f_\varphi}{\partial \varphi} \end{bmatrix} \tag{4.84}$$

The eigenvalues of $\boldsymbol{J}$ will allow the stability of the fixed points to be assessed. In order to evaluate this, we need to study the dependence of R_j as a function of C, D, φ. Applying the change of variables (4.82b) to the definition (4.40) of R_j, and then setting

$D = 0$, we obtain

$$R_j = C\sqrt{1 + 2c_j s_j \cos\varphi} \tag{4.85}$$

The derivatives of R_j with respect to C, D, φ at a point $(C, D = 0, \varphi)$ are

$$\begin{cases} \frac{\partial R_j}{\partial C} & = \sqrt{1 + 2c_j s_j \cos\varphi} \\ \frac{\partial R_j}{\partial D} & = \frac{c_j^2 - s_j^2}{\sqrt{1+2c_j s_j \cos\varphi}} \\ \frac{\partial R_j}{\partial \varphi} & = -\frac{c_j s_j \sin\varphi}{\sqrt{1+2c_j s_j \cos\varphi}} C \end{cases} \tag{4.86a}$$

For a spinning wave, i.e. setting $(C, D, \varphi) = (A^{sp}, 0, \pi/2)$ and a standing wave, i.e. setting $(C, D, \varphi) = (A^{st}, 0, 0)$, equations (4.85) and (4.86) become

$$\text{spinn. wave:} \quad \begin{cases} R_j & = A^{sp} \\ \frac{\partial R_j}{\partial C} & = 1 \\ \frac{\partial R_j}{\partial D} & = c_j^2 - s_j^2 \\ \frac{\partial R_j}{\partial \varphi} & = -c_j s_j A^{sp} \end{cases} \qquad \text{stand. wave:} \quad \begin{cases} R_j & = A^{st}\sqrt{1 + 2c_j s_j} \\ \frac{\partial R_j}{\partial C} & = \sqrt{1 + 2c_j s_j} \\ \frac{\partial R_j}{\partial D} & = \frac{c_j^2 - s_j^2}{\sqrt{1+2c_j s_j}} \\ \frac{\partial R_j}{\partial \varphi} & = 0 \end{cases} \tag{4.87}$$

From now onwards, we will use a subscript *sp* to denote that a quantity is evaluated at the fixed point of a spinning wave, and a subscript *st* to denote that a quantity is evaluated at the fixed point of a standing wave.

In evaluating the terms of (4.84), one first analytically evaluates the gradients, and then substitute $(C, D, \varphi) = (A^{sp}, 0, \pi/2)$ for spinning solutions and $(C, D, \varphi) = (A^{st}, 0, 0)$ for standing solutions, and then equation (4.87). For both standing and spinning waves the Jacobian is a block diagonal matrix:

$$\boldsymbol{J} = \begin{bmatrix} \frac{\partial f_C}{\partial C} & 0 & 0 \\ 0 & \frac{\partial f_D}{\partial D} & \frac{\partial f_D}{\partial \varphi} \\ 0 & \frac{\partial f_\varphi}{\partial D} & \frac{\partial f_\varphi}{\partial \varphi} \end{bmatrix} \tag{4.88}$$

This was expected from the symmetries of the equations and is the reason why we applied the change of variables (4.82b). One eigenvalue is trivially $\lambda_1 = \frac{\partial f_C}{\partial C}$, and can be interpreted in terms of the Rayleigh criterion at limit-cycles, as discussed in the main manuscript. The other 2 eigenvalues are the solutions of the characteristic

polynomial

$$\lambda^2 - \left(\frac{\partial f_D}{\partial D} + \frac{\partial f_\varphi}{\partial \varphi}\right)\lambda + \left(\frac{\partial f_D}{\partial D}\frac{\partial f_\varphi}{\partial \varphi} - \frac{\partial f_D}{\partial \varphi}\frac{\partial f_\varphi}{\partial D}\right) = 0 \tag{4.89}$$

Applying the Routh-Hurwitz criterion, all the real parts of the three eigenvalues are not negative, i.e. the fixed point is stable or neutrally stable, if and only if all the coefficients of the second order polynomial (4.89) are not negative (Hurwitz, 1964). This leads to the following necessary and sufficient conditions for stability:

$$\begin{cases} \frac{\partial f_C}{\partial C} & \leq 0 \\ \frac{\partial f_D}{\partial D} + \frac{\partial f_\varphi}{\partial \varphi} & \leq 0 \\ \frac{\partial f_D}{\partial D}\frac{\partial f_\varphi}{\partial \varphi} - \frac{\partial f_D}{\partial \varphi}\frac{\partial f_\varphi}{\partial D} & \geq 0 \end{cases} \tag{4.90}$$

4.7.6 Stability of spinning solutions

For a spinning solution $(C, D, \varphi) = (A^{sp}, 0, \pi/2)$, the 5 components of the Jacobian (4.88) are:

$$\left.\frac{\partial f_C}{\partial C}\right|_{sp} = \frac{A^{sp}}{2} F^{sp'}\left(A^{sp}\right) \tag{4.91a}$$

$$\left.\frac{\partial f_D}{\partial D}\right|_{sp} = \frac{A^{sp}}{4} F^{sp'}\left(A^{sp}\right) \tag{4.91b}$$

$$\left.\frac{\partial f_D}{\partial \varphi}\right|_{sp} = \frac{A^{sp^2}}{16} N_b \mathrm{Im}\left[Q'\left(A^{sp}, \omega\right)\right] \tag{4.91c}$$

$$\left.\frac{\partial f_\varphi}{\partial D}\right|_{sp} = -\frac{N_b}{4}\mathrm{Im}[Q'\left(A^{sp}, \omega\right)] \tag{4.91d}$$

$$\left.\frac{\partial f_\varphi}{\partial \varphi}\right|_{sp} = \frac{A^{sp}}{4} F^{sp'}\left(A^{sp}\right) \tag{4.91e}$$

where the prime expresses a derivative with respect to the amplitude A. The stability conditions (4.90) for a spinning mode are:

$$F^{sp'}\left(A^{sp}\right) < 0 \tag{4.92a}$$

$$\frac{A^{sp}}{4} F^{sp'}\left(A^{sp}\right) + \frac{A^{sp}}{4} F^{sp'}\left(A^{sp}\right) < 0 \tag{4.92b}$$

$$\left(\frac{A^{sp}}{4} F^{sp'}\left(A^{sp}\right)\right)^2 - \frac{A^{sp^2}}{16} N_b \mathrm{Im}\left[Q'\left(A^{sp}, \omega\right)\right]\left(-\frac{N_b}{4}\mathrm{Im}[Q'\left(A^{sp}, \omega\right)]\right) > 0 \tag{4.92c}$$

Trivially the second inequality is equivalent to the first one. We substitute in the first and third inequality the definition of F^{sp} from (4.51), and we obtain:

$$\mathrm{Re}\left[Q'\left(A^{sp},\omega\right)\right] <0 \tag{4.93}$$

$$\mathrm{Re}\left[Q'\left(A^{sp},\omega\right)\right]^2 + \mathrm{Im}\left[Q'\left(A^{sp},\omega\right)\right]^2 >0 \tag{4.94}$$

with equation (4.94) always satisfied if $\mathrm{Re}\left[Q'\left(A^{sp},\omega\right)\right] < 0$. It follows that a spinning wave with amplitude A^{sp} is stable if and only if (4.93) holds, which is the condition (4.57) reported in the manuscript.

4.7.7 Stability of standing solutions

For a standing solution $(C, D, \varphi) = (A, 0, \varphi)$, the 5 components of the Jacobian (4.88) are:

$$\frac{\partial f_C}{\partial C}_{st} = \frac{A^{st}}{2} F^{st'}\left(A^{st}\right) \tag{4.95a}$$

$$\frac{\partial f_D}{\partial D}_{st} = -\sum_{j=1}^{N_b} c_j s_j \mathrm{Re}\left[Q\left(A^{st}\sqrt{1+2c_j s_j},\omega\right)\right] + \ldots$$

$$\ldots \quad A^{st}\frac{1}{4}\sum_{j=1}^{N_b}\frac{(c_j^2-s_j^2)^2}{\sqrt{1+2c_j s_j}}\mathrm{Re}\left[Q'\left(A^{st}\sqrt{1+2c_j s_j},\omega\right)\right] \tag{4.95b}$$

$$\frac{\partial f_D}{\partial \varphi}_{st} = -\frac{A_{st}}{2}\sum_{j=0}^{N_b} c_j s_j \mathrm{Im}\left[Q\left(A^{st}\sqrt{1+2c_j s_j},\omega\right)\right] \tag{4.95c}$$

$$\frac{\partial f_\varphi}{\partial D}_{st} = \frac{2}{A^{st}}\sum_{j=1}^{N_b} c_j s_j \mathrm{Im}\left[Q\left(A^{st}\sqrt{1+2c_j s_j},\omega\right)\right] - \ldots$$

$$\ldots \quad \frac{1}{2}\sum_{j=1}^{N_b}\frac{(c_j^2-s_j^2)^2}{\sqrt{1+2c_j s_j}}\mathrm{Im}\left[Q'\left(A^{st}\sqrt{1+2c_j s_j},\omega\right)\right] \tag{4.95d}$$

$$\frac{\partial f_\varphi}{\partial \varphi}_{st} = -\sum_{j=1}^{N_b} c_j s_j \mathrm{Re}\left[Q\left(A^{st}\sqrt{1+2c_j s_j},\omega\right)\right] \tag{4.95e}$$

The stability conditions (4.90) for a spinning mode are reported in the inequalities (4.58). We prove here some asymptotic properties of the inequalities (4.58) discussed in the main body of the chapter. For a large number of burners N_b, we have that the sums in (4.58) can be approximated as an integral.

4.7.7.1 Standing pattern condition

We first discuss the third condition (4.58c), which becomes

$$\int_0^{2\pi} \frac{\sin(2\theta)}{2} \mathrm{Re}\left[Q(A^{st}\sqrt{1+\sin(2\theta)},\omega)\right] d\theta - \dots$$
$$\dots \quad \int_0^{2\pi} A^{st} \frac{1}{8} \frac{\cos(2\theta)^2}{\sqrt{1+\sin(2\theta)}} \mathrm{Re}\left[Q'(A^{st}\sqrt{1+\sin(2\theta)},\omega)\right] d\theta > 0 \tag{4.96}$$

We rewrite the second integral as

$$-\frac{1}{8}\int_0^{2\pi} \cos(2\theta) \left[\frac{A^{st}\cos(2\theta)}{\sqrt{1+\sin(2\theta)}} \mathrm{Re}\left[Q'(A^{st}\sqrt{1+\sin(2\theta)},\omega)\right]\right] d\theta \tag{4.97}$$

where the term between square brackets is the derivative with respect to θ of the function $\mathrm{Re}\left[Q(A^{st}\sqrt{1+\sin(2\theta)},\omega)\right]$. We integrate by parts, and obtain

$$-\frac{1}{8}\Big[\left\{\cos(2\theta)\mathrm{Re}\left[Q(A^{st}\sqrt{1+\sin(2\theta)},\omega)\right]\right\}_0^{2\pi} + \dots$$
$$\dots \quad 2\int_0^{2\pi} \sin(2\theta)\mathrm{Re}\left[Q(A^{st}\sqrt{1+\sin(2\theta)},\omega)\right] d\theta\Big] \tag{4.98}$$

where the first term in square brackets evaluates to zero. We substitute this expression in (4.96) and obtain the condition (4.59).

4.7.7.2 Orientation condition

We then discuss the second condition (4.58c). We observe that

$$0 = \int_0^{2\pi} \frac{\partial}{\partial\theta}\left[-\frac{\cos(2\theta)}{4}\mathrm{Re}\left[Q(A\sqrt{1+\sin(2\theta)},\omega)\right]\right] d\theta$$
$$= \int_0^{2\pi} \frac{\sin(2\theta)}{2}\mathrm{Re}\left[Q(A^{st}\sqrt{1+\sin(2\theta)},\omega)\right] d\theta - \dots$$
$$\dots \quad \int_0^{2\pi} A^{st}\frac{1}{4}\frac{\cos(2\theta)^2}{\sqrt{1+\sin(2\theta)}}\mathrm{Re}\left[Q'(A^{st}\sqrt{1+\sin(2\theta)},\omega)\right] d\theta \tag{4.99}$$

Notice how the last expression of the identity (4.99) is the first term in square brackets in the first addend of (4.58c). For the same reason, also the second term in square brackets in the second addend of (4.58c) is zero. It follows that the condition results in $0 \geq 0$.

4.7.8 Scaling of the flame response

We here discuss the choice of values of σ_r/ω_{lin} and α_r/ω_{lin} used in §4.4. We choose quite a small[1] growth-rate $\overline{\sigma}_r \equiv \sigma/\omega_{lin} = 0.01$ because we are studying a thermoacoustic system exhibiting triggering, so that the flame gain is weak at small amplitudes. We then exploit the fact that $\omega_0 \approx \omega_{lin}$ and fix $\overline{\alpha}_r \equiv \alpha/\omega_1 = 0.08$ similarly to Noiray et al. (2011), where $\alpha/\omega_0 = 0.08$. Then we can use the relation (4.32) for a given number of burners N_b and calculate a reasonable value for $\overline{\beta} \equiv \beta/\omega_{lin}$:

$$\frac{N_b\overline{\beta}\cos(\phi)}{2} = (2\overline{\sigma}_r + \overline{\alpha}_r) = 0.10 \tag{4.100}$$

In the chapter we decide to fix the phase response to $\phi = \pi/5$. $\overline{\beta}$ is the gain of the flame response that leads to the vertical scaling of Figure 4.3.b for $N_b = 6$, and equation (4.100) fixes the product $\overline{\beta}N_b$ to a constant.

Notice how $\overline{\alpha}_r$ is just a reasonable value of the damping used to fix the product $\overline{\beta}N_b$, while in the manuscript the study is parametric in α. We can finally calculate ω_0 from equation (4.31):

$$\omega_0 = \omega_{lin}\sqrt{\omega_{lin}^2 + B^2} + B \qquad \text{with:} \quad B = \frac{\beta N_b}{4}\sin(\pi/5) \tag{4.101}$$

We then change the time variable $t \to \omega_{lin}t$, so that in equations (4.33) instead of α we have $\overline{\alpha}$, and instead of ω_0 (in that equation ω is actually ω_0, refer to the text just before the equation) we have ω_0/ω_{lin}. In the time domain simulations we simply fix $\omega_{lin} = 1$.

[1] In Bothien et al. (2015) the value σ/ω_{lin} is typically of 0.05, see their figure 6.

Chapter 5

Nonlinear analytic modelling of the delay

5.1 Introduction

Low-order models of azimuthal instabilities usually describe the system as a damped wave equation, with the fluctuating heat release q as a source term. The equations from chapter §2 are:

$$\begin{cases} u_{,t} + p_{,\theta} = 0 \\ p_{,t} + u_{,\theta} = q - \alpha p \end{cases} \tag{5.1}$$

In the equation, α is a positive damping coefficient, $p(t, \theta)$ is the fluctuating pressure, $u(t, \theta)$ is the fluctuating velocity in the azimuthal direction, with θ being the azimuthal angle in the periodic domain $[0\,,\,2\pi)$. We focus on a rotationally symmetric system in the azimuthal direction θ, i.e. we assume that u, p, q do not have any direct dependence on θ. A discussion of the direct dependence on θ of the equation can be found in Noiray et al. (2011). A discussion of the effect of a discrete[1] rotation group of symmetry, instead of full rotational symmetry, can be found in chapter §4.

The focus of this chapter is on the effect of the time delay between acoustic excitation and flame response, and on the accuracy of the nonlinear mathematical methods used to treat the problem. The chapter is organised as follows. In §5.1.1 we further characterize the problem, and massage the equations. In §5.2 we discuss the effect of the delay τ on the linear stability of the system and on the nonlinear solutions

[1] in reality there is always an integer number N of burners in annular combustors, so that the problem repeats itself when a rotation of the angle $2\pi/N$ is applied

of the problem. We then carry out a nonlinear analysis of the system by applying the method of temporal averaging in §5.3 and the method of multiple scales in §5.4. We show that in the space of parameters leading to a limit-cycle the delay does not affect the type and the stability of oscillatory solutions: the only stable solution is spinning clockwise/anticlockwise, with the standing mode being always an unstable solution. We finally discuss the accuracy of the two methods in predicting the nonlinear solutions in §5.5, by comparing their results with numerical time domain simulations of the problem. This is particularly important for the application of nonlinear system identification techniques.

5.1.1 Model

We model the fluctuating heat release q at one time t as a function of the acoustic longitudinal fluctuating velocity u_L at the flame inlet, at a previous time $t - \tau_1$:

$$q(t) = q(u_L(t - \tau_1)). \tag{5.2}$$

The reasoning behind this is that an acoustic fluctuation of the longitudinal velocity at the injector induces a perturbation of the fuel/air mixture fraction and/or of the local flow field. This second perturbation is amplified by means of flow instabilities and/or modulates the swirl in swirling flames, and both mechanisms lead to perturbations of the flame response. For an in-depth review of these and other mechanisms, refer to Candel et al. (2013); Ducruix et al. (2003); Lieuwen (2003, 2012).

The fluctuating longitudinal velocity u_L can be expressed as a linear transfer function of the pressure p in the annular chamber, as long as only one thermoacoustic mode oscillates, as discussed in chapter §4. This transfer function will depend on the geometrical properties of the whole combustor and on the acoustic response of the burner. This longitudinal wave is accompanied by a mass flow oscillation, which in Wolf et al. (2012) is proposed to be the major cause of heat release fluctuations, consistently with (5.2). We can then write that

$$q(t) = q(p(t - \tau)) \tag{5.3}$$

where τ is different from the delay τ_1 presented in (5.2). We study the nonlinear saturated model for q:

$$q(t) = \beta p(t - \tau) - \kappa p(t - \tau)^3 \tag{5.4}$$

A cubic saturation model for the fluctuating heat release response q was first proposed by Noiray et al. (2011), to which we refer the reader for a discussion. We can recover the model of Noiray et al. (2011) by setting τ to zero in (5.4). The coefficient $\kappa > 0$ of p^3 in (5.4) can be taken out of the analysis, after applying the change of variables $(p, u) \to (p/\sqrt{\kappa}, u/\sqrt{\kappa})$ as discussed in chapter §2. This coefficient is however required in order to apply system identification to the system, as discussed by Noiray and Schuermans (2013). If there are limit-cycle solutions, a non-zero delay τ in (5.4) leads to a shift of their frequency of oscillation. Because it puts out of sync q and p, it causes a less favourable Rayleigh criterion and makes a system less unstable or more stable Rayleigh (1894), as reviewed in Dowling and Stow (2003) for a duct with a flame modelled as a point source.

We project the equations (5.1) on the Galerkin base $\{\cos(n\theta), \sin(n\theta)\}$ as discussed in chapter §2:

$$\begin{cases} u(t,\theta) \approx n\eta_1(t)\sin(n\theta) - n\eta_2(t)\cos(n\theta) \\ p(t,\theta) \approx \eta_1'(t)\cos(n\theta) + \eta_2'(t)\sin(n\theta) \end{cases} \tag{5.5}$$

where the prime denotes a time derivative, and n is the azimuthal wavenumber of the thermoacoustic mode we are studying. We obtain the equations:

$$\eta_1''(t) + \omega_0^2\eta_1(t) = f(\eta_1'(t), \eta_1'(t-\tau), \eta_2'(t-\tau)) \tag{5.6a}$$
$$\eta_2''(t) + \omega_0^2\eta_2(t) = f(\eta_2'(t), \eta_2'(t-\tau), \eta_1'(t-\tau)) \tag{5.6b}$$

where $\omega_0 = n$ and the function f is defined as:

$$f(a, a_\tau, b_\tau) \equiv a_\tau \left[\beta - \frac{3}{4}\kappa\left(a_\tau^2 + b_\tau^2\right)\right] - \alpha a \tag{5.7}$$

An example of time domain simulation of the oscillators (5.6) is presented in Figure 5.1, where η_1 and η_2 are oscillating as a function of time, reported with continuous thin lines, and the other lines will be discussed later.

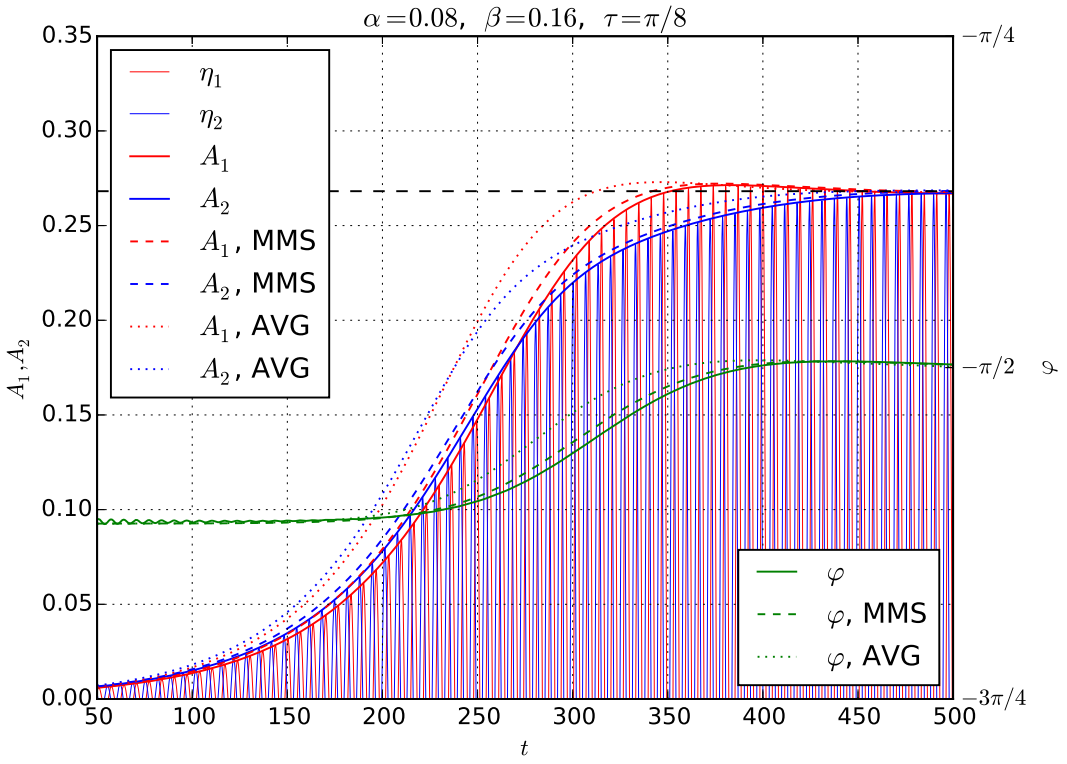

Fig. 5.1 Example of a time domain simulation of the coupled oscillators η_i and their amplitudes of oscillation A_i (continuous lines), of the slow flow calculated with the method of multiple scales (dashed lines), and of the slow flow calculated with the method of averaging (dotted lines). The horizontal dashed black line is the amplitude of oscillation at the limit-cycle as predicted by the two methods.

5.2 Linear Analysis

In this section we study the boundary of linear stability of (5.6). We proceed by retaining only the linear terms in (5.6a) and (5.6b), and obtain:

$$\eta_j''(t) + \alpha\eta_j'(t) - \beta\eta_j'(t-\tau) + \omega_0^2\eta_j(t) = 0 \qquad j = 1, 2 \tag{5.8}$$

We substitute $\eta_1(t) = e^{(\sigma+i\omega)t}$ into (5.8) and obtain the characteristic equation. We then split the equation in real and imaginary parts and after some manipulations obtain:

$$\beta\cos(\tau\omega)e^{-\sigma\tau} - \alpha = \frac{\sigma}{\omega}\left[2\omega + \beta\sin(\tau\omega)e^{-\sigma\tau}\right] \tag{5.9a}$$

$$\omega^2 - \omega_0^2 + \beta\omega\sin(\tau\omega)e^{-\sigma\tau} = \sigma^2 + \alpha\sigma - \beta\sigma\cos(\tau\omega)e^{-\sigma\tau} \tag{5.9b}$$

We then study for which parameters $\{\alpha, \beta, \tau\} \in \mathbb{R}^{+3}$ the system is neutrally stable, i.e. there exist real-valued solutions ω_L of the system of equations (5.9) when setting the growth-rate σ to zero:

$$\beta \cos(\tau\omega_L) - \alpha = 0 \tag{5.10a}$$

$$\omega_L^2 - \omega_0^2 + \beta\omega_L \sin(\tau\omega_L) = 0 \tag{5.10b}$$

By studying as a function of σ the LHS and RHS of (5.9a), we find that there exists only one solution for the growth-rate σ, and that it is positive if $\beta \cos(\tau\omega) - \alpha > 0$. It follows that equation (5.10a) defines the boundary of instability, with the system being unstable if the LHS is positive. We also observe from (5.10b) that when on the boundary, if the delay τ is zero, ω_L matches the natural frequency of oscillation ω_0.

The domain of investigation of the problem is $(\alpha, \beta, \tau) \in \mathbb{R}^{+3}$. We observe that if (α, β, τ) provide a real-valued solution ω_L of (5.10), then (α, β, τ_k) is a solution too, with

$$\tau_k = \tau + 2k\pi/\omega_L \ , \qquad k \in \mathbb{N}^+. \tag{5.11}$$

We can then initially limit the search of solutions restricting the domain of τ to

$$\tau \in \left[-\frac{\pi}{\omega_L}, \frac{\pi}{\omega_L}\right) \tag{5.12}$$

and then exploit (5.11) to generate the other solutions. Since ω_L is close to the natural frequency of the system ω_0 the domain (5.12) is bounded. Moreover, since α and β are positive, equation (5.10a) allows us to further restrict the domain so that the cosine term is positive:

$$\tau \in \left[-\frac{\pi}{2\omega_L}, \frac{\pi}{2\omega_L}\right) \tag{5.13}$$

This is in line with the Rayleigh criterion Rayleigh (1878): the phase difference between q and p must be in the range $(-\pi/2, \pi/2)$ to cause instability.

The domain (5.13) allows negative values of τ, though a negative value in the system does not make physical sense. We investigate negative solutions nonetheless, because negative solutions τ lead to positive solutions τ_k by the application of (5.11). We study the boundary parametrically in α, and in the following figures we will fix $\alpha/\omega_0 = 0.08$. The neutrality of the solutions is defined by (5.10a), from which we can calculate the reduced linear driving β_L at the onset of instability as a function of α

and τ:

$$\beta_L = \alpha \sec(\tau\omega_L), \tag{5.14}$$

The frequencies of the neutrally stable solutions are the solutions ω_L of (5.10b). We substitute β from (5.14) into (5.10b) and obtain:

$$h(\tau, \omega_L) \equiv \omega_L^2 - \omega_0^2 + \alpha\omega_L \tan(\omega_L\tau) = 0 \tag{5.15}$$

Since we cannot solve analytically ω_L as a function of τ from (5.15), we show in Figure 5.2 a contour plot of h/ω_0^2, in the restricted domain (5.13). The solution of (5.15) is the implicit curve satisfying $h/\omega_0^2 = 0$, reported in the figure with the black line. There are two solutions ω_L for each value of τ if $\hat{\tau} < \tau < 0$, with $\hat{\tau}\omega_0 \approx -1.13$. This line shows the effect of the delay τ, non-dimensionalized with respect to ω_0, on the frequency shift ω_L/ω_0 on the border of neutral stability.

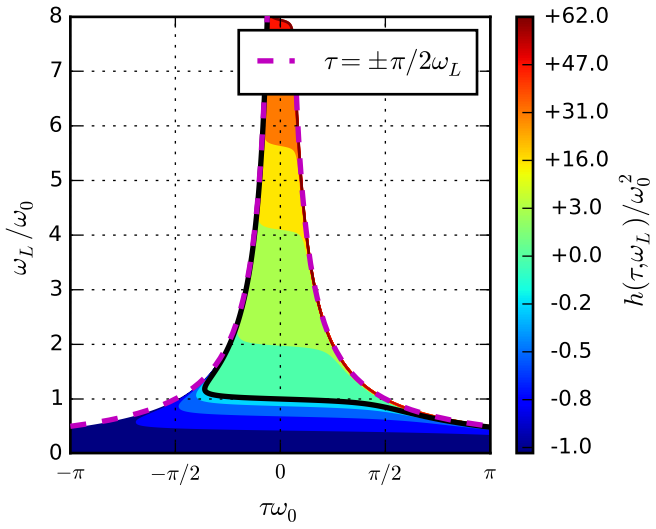

Fig. 5.2 Contour plots of h from equation (5.15), with $\alpha/\omega_0 = 0.08$. On the black line $h = 0$, i.e. equation (5.10) is satisfied and the system is neutrally stable.

Figure 5.3 shows the critical value of β/α along the neutral stability contour $h = 0$ of Figure 5.2. The value of β/α that makes also ω_B a neutrally stable solution is much higher. For the applications we are interested in, Figure 5.4 shows a restricted view of the space of parameters, fixing a maximum value of $\beta/\alpha = 4$. On the left of the same figure we can appreciate the drift of the frequency as a function of the delay, always within 15% of the natural acoustic frequency of the system.

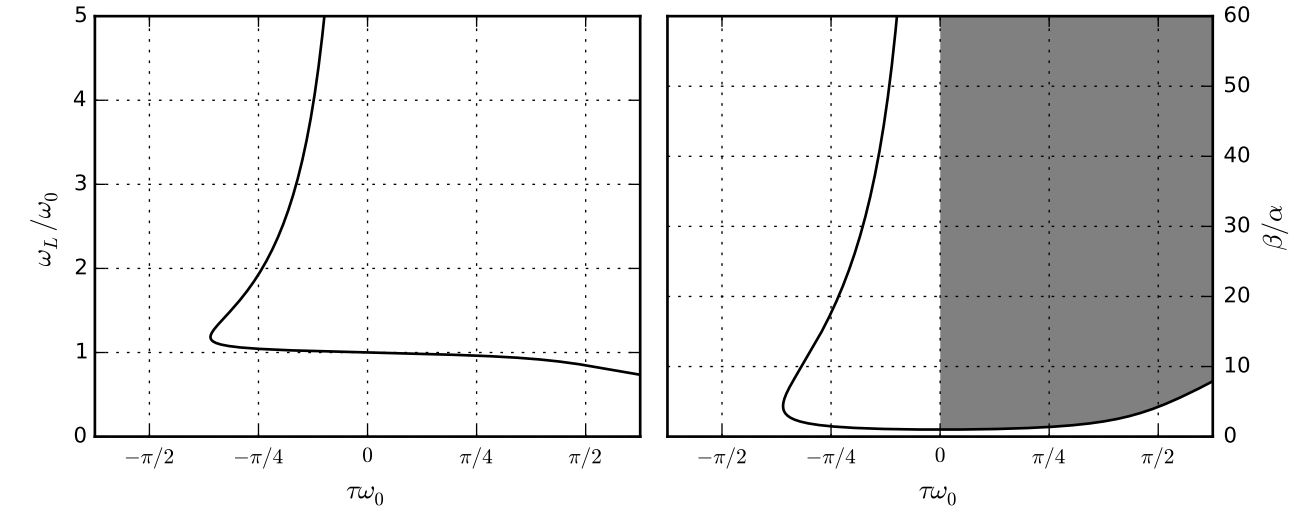

Fig. 5.3 On the left, the implicit function showing the frequency of the neutrally stable modes as a function of the delay τ. On the right, the stability map of the system. The curve represents the values of β/α as a function of τ on which the system is neutrally stable. We study the system for positive values of the delay τ, where the linearly unstable region is reported in gray.

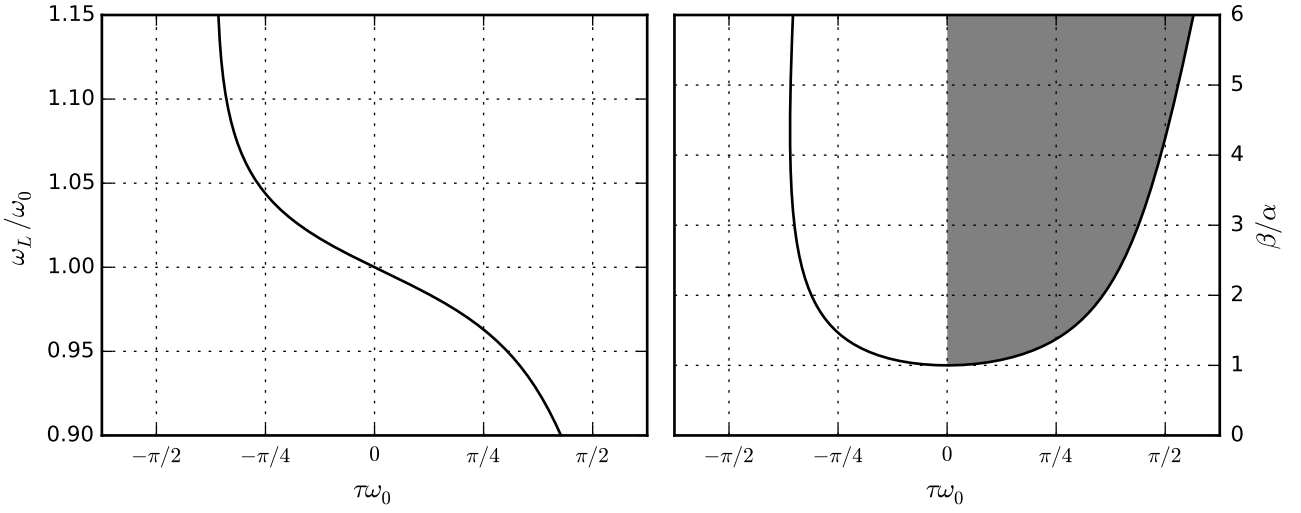

Fig. 5.4 Zoom of Figure 5.3, restricted to values of $\beta/\alpha \leq 6$. The frequency increase/decrease due to the coupling with the fluctuating heat release is clearly visible on the left. Positive/negative values of τ lead to negative/positive frequency shifts.

For a fixed value of the damping parameter α, the full boundary of neutral stability can be obtained by applying the transformation (5.11) to values of $(\beta/\alpha, \tau\omega_0)$ from Figure 5.3. A part of it is reported as thick black line in Figure 5.6. We observe that the boundary of stability gets closer to the line $\beta/\alpha = 1$ as the delay τ increases. This means

that the phase response of the flame is less influential for high-frequency instabilities than for low-frequency instabilities, because the ratio between the time-delay τ and the acoustic period T is larger for them.

We present in Figure 5.5 all the neutrally stable solutions, obtained applying the transformation (5.11) to the neutral boundary presented in figure 5.3.

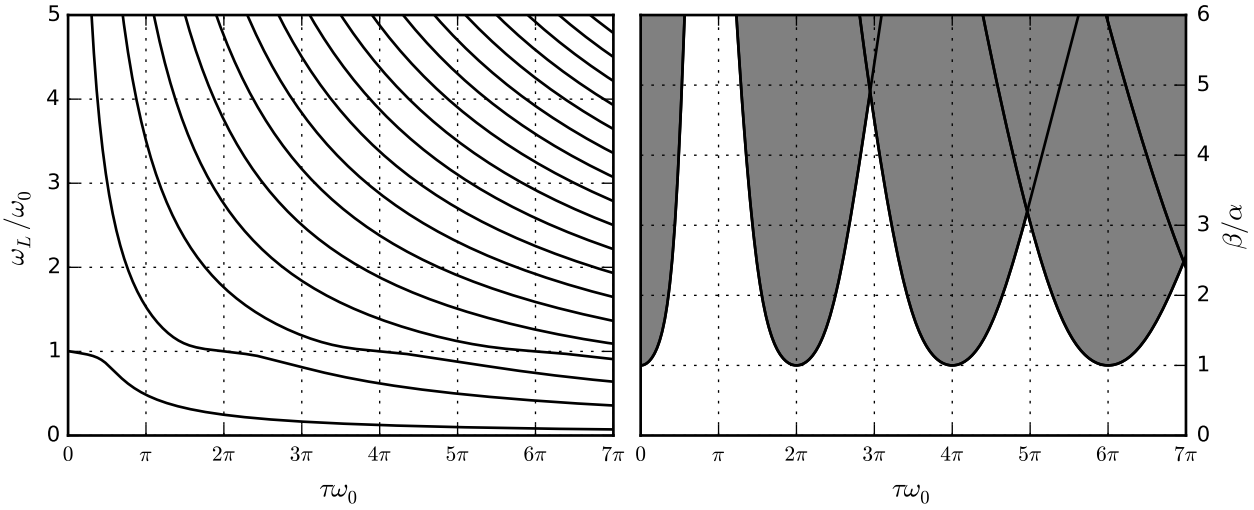

Fig. 5.5 On the left, the frequencies of oscillation on the boundary of neutral stability of the problem, for $\alpha/\omega_0 = 0.08$. On the right, the stability map of the system, with the linearly unstable region reported in gray.

5.3 Method of averaging

In this section we apply first order averaging to the model, as defined and discussed in Sanders and Verhulst (2007). We rewrite (5.6) as a first order system $(x_j, y_j) \equiv (\eta_j, \eta_j')$:

$$x_j'(t) = y_j(t) \tag{5.16a}$$
$$y_j'(t) = -\omega_0^2 x_j(t) + f_j \tag{5.16b}$$

where $f_1 = f(y_1(t), y_1(t-\tau), y_2(t-\tau))$ and $f_2 = f(y_2(t), y_2(t-\tau), y_1(t-\tau))$. We introduce the change of variables $(x_j, y_j) \to (A_j, \varphi_j)$:

$$\begin{cases} 2x_j(t) = & A_j(t)e^{i(\omega t+\varphi_j(t))} + \text{c.c.} \\ 2y_j(t) = & i\omega A_j(t)e^{i(\omega t+\varphi_j(t))} + \text{c.c.} \end{cases} \tag{5.17}$$

where c.c. denotes the complex conjugate of the expression to its left. We then substitute (5.17) into (5.16), and add (5.16a) multiplied by $ie^{i(\omega t+\varphi_j)}\omega$ and (5.16b) multiplied by $-e^{i(\omega t+\varphi_j)}$. We obtain

$$\frac{\omega^2-\omega_0^2}{2}A_j e^{2i(\omega t+\varphi_j(t))}+\omega\left(\varphi_i'(t)+\frac{\omega}{2}-\frac{\omega_0^2}{2\omega}\right)A_j(t)+i\omega A_j'(t)=-e^{i(\omega t+\varphi_j(t))}f_j(t,A_1(t),A_1(t),\ldots) \tag{5.18}$$

where f depends on the fast time variable t and on the slow variables, which are the amplitudes $A_1(t), A_2(t), A_1(t-\tau), A_2(t-\tau)$ and the phases $\varphi_1(t), \varphi_2(t), \varphi_1(t-\tau), \varphi_2(t-\tau)$. Notice that f is periodic in its direct dependence on t, with period $2\pi/\omega$. We apply first order averaging Sanders and Verhulst (2007): we approximate the slow variables as constant in the period of oscillation $2\pi/\omega$ and time-average both sides of (5.18). The first term on the LHS has period π/ω and vanishes out. We are left with:

$$\left(\varphi_i'(t)+\frac{\omega}{2}-\frac{\omega_0^2}{2\omega}\right)A_j(t)\omega+i\omega A_j'(t)\approx-\frac{1}{2\pi/\omega}\int_{t-\pi/\omega}^{t+\pi/\omega}e^{i(\omega s+\varphi_j(t))}f_j(s,A_1(t),\ldots)ds \tag{5.19}$$

The delayed slow variables such as $A_1(t-\tau)$ are approximated as $A_1(t)$ since the delay τ is assumed to be of the same order of the period of oscillation, i.e. small compared to the timescale of the slow variables, as discussed in Saha et al. (2010); Wahi and Chatterjee (2004).

We then evaluate the integral at the RHS of (5.19). We take the constant term $e^{i\varphi_j(t)}$ out of the integral, introduce the point $z=e^{i\omega_0 s}$ on the complex unit circle and change the integration variable from s to z, obtaining a closed path integral on the unit circle around the origin:

$$-e^{i\varphi_j(t)}\frac{1}{2\pi i}\oint f_j(z,A_1(t),\ldots)dz=-e^{i\varphi_j(t)}\mathrm{Res}_{z=0}[f_j] \tag{5.20}$$

The term $f_j(z,A_1(t),\ldots)$ is a Laurent polynomial in z, and is then holomorphic everywhere except at $z=0$, so that in the last passage above we applied the residue theorem. The residue is the coefficient of $1/z$ in the expression of f_j:

$$\begin{aligned}g_1(A_1,A_2,\varphi)\equiv&-\frac{e^{i\varphi_1(t)}}{\omega}\mathrm{Res}_{z=0}[f_1]\\=&\frac{1}{2}iA_1\left(\beta e^{i\tau\omega}-\alpha\right)-\frac{3}{32}iA_1\kappa\omega^2e^{i\tau\omega}\left(A_2^2e^{2i\varphi}+3A_1^2+2A_2^2\right)\end{aligned} \tag{5.21}$$

where φ is the difference between the phases of the first and second oscillator, $\varphi = \varphi_1 - \varphi_2$, and the expression for g_2 is obtained similarly. From (5.19) we obtain the equations for the time evolution of the slow variables of the two oscillators:

$$\begin{cases} (\varphi_1'(t) + \omega - \omega_0^2/\omega)\, A_1(t) + iA_1'(t) = \quad g_1(A_1, A_2, +\varphi) \\ (\varphi_2'(t) + \omega - \omega_0^2/\omega)\, A_2(t) + iA_2'(t) = \quad g_2(A_2, A_1, -\varphi) \end{cases} \qquad \varphi \equiv \varphi_1 - \varphi_2 \tag{5.22}$$

This dynamical system is in terms of the variables $\{A_1, A_2, \varphi_1, \varphi_2\}$ and can present solutions where both phases φ_1 and φ_2, in the limit $t \to \infty$, present a common oblique asymptote, i.e. the two oscillators undergo the same shift of their oscillation frequency. However, these solutions are not fixed points of (5.22) since $\varphi_j(t) \neq 0$. These solutions are however fixed points of an equivalent system, in terms of the variables $\boldsymbol{x} = \{A_1, A_2, \varphi, \varphi_{avg} \equiv (\varphi_1 + \varphi_2)/2\}$:

$$\begin{aligned}
A_1' =& \frac{A_1}{2}(\beta\cos(\tau\omega) - \alpha) - \frac{3}{32}A_1\kappa\omega^2(A_2^2\cos(\tau\omega + 2\varphi) + \quad \dots \\
& \qquad \dots \quad 3A_1^2\cos(\tau\omega) + 2A_2^2\cos(\tau\omega)) && \text{(5.23a)} \\
A_2' =& \frac{A_2}{2}(\beta\cos(\tau\omega) - \alpha) - \frac{3}{32}A_2\kappa\omega^2(A_1^2\cos(2\varphi - \tau\omega) + \quad \dots \\
& \qquad \dots \quad 2A_1^2\cos(\tau\omega) + 3A_2^2\cos(\tau\omega)) && \text{(5.23b)} \\
\varphi' =& \frac{3}{16}\kappa\omega^2\sin(\varphi)\left(A_1^2\cos(\varphi - \tau\omega) + A_2^2\cos(\varphi + \tau\omega)\right) && \text{(5.23c)} \\
\varphi_{avg}' + \omega =& \frac{\omega_0^2}{\omega} - \frac{1}{2}\beta\sin(\tau\omega) + \frac{3}{64}\kappa\omega^2(A_2^2\sin(\tau\omega + 2\varphi) - A_1^2\sin(2\varphi - \tau\omega) + \quad \dots \\
& \qquad \dots \quad 5(A_1^2 + A_2^2)\sin(\tau\omega)) && \text{(5.23d)}
\end{aligned}$$

In (5.23), the first three equations describe the amplitudes and the synchronization of the two oscillators: the fixed points of these three equations, which depend parametrically in ω, are the synchronized solutions of the system.

5.3.1 The choice of ω

When applying the method of averaging, one often assumes that the frequency of oscillation ω is close to the natural frequency of oscillation ω_0 of the unperturbed oscillator, and can approximate $\omega \approx \omega_0$. This assumption is often carried out earlier in the analysis, by fixing $\omega = \omega_0$ in (5.17). We have however observed in §5.2 that the

frequency of oscillation ω_L of the neutrally stable, linearized system departs from ω_0, and is most noticeably dependent on τ, as in figure 5.4.

We can improve the choice of ω from ω_0 by using equation (5.23d), and choosing ω such that the mean average phase φ_{avg} is a fixed point of the system too, by setting it to zero. This leads to an equation for ω:

$$\omega^2 = \omega_0^2 - \frac{1}{2}\beta\omega\sin(\tau\omega) + \frac{3}{64}\kappa\omega^3(A_2^2\sin(\tau\omega+2\varphi) - A_1^2\sin(2\varphi-\tau\omega) + \quad \dots \\ \dots \quad + 5(A_1^2+A_2^2)\sin(\tau\omega)) \tag{5.24}$$

In the linear regime $A_i \to 0$, and from (5.24) we recover the linear dispersion relation (5.10b) (but not calculated on the boundary of instability). In the nonlinear regime, the frequency of oscillation shifts from this value and it is amplitude dependent. We numerically integrate in time the first three equations (5.23), and at each timestep calculate the instantaneous frequency ω which satisfies (5.24). An example of a simulation is reported in Figure 5.1, where A_1, A_2 and φ are reported as dashed lines.

5.3.1.1 The dynamic equation for ω in the general case

For reference, we discuss the dynamic equation for the frequency also for the generic choice of the heat release response discussed in Chapter §4. One obtains:

$$\omega - \frac{\omega_0^2}{\omega} = -\frac{1}{A_1}\langle f_1\sin(\omega t+\varphi_1)\rangle - \frac{1}{A_2}\langle f_2\sin(\omega t+\varphi_2)\rangle \tag{5.25}$$

We proceed by substituting the expressions (4.73b) and (4.73d) in (5.25) and obtain

$$\omega - \frac{\omega_0^2}{\omega} = -\frac{1}{2}\sum_{j=1}^{N_b} G(R_j,\omega)\Big[\sin\phi(R_j,\omega) + c_j s_j\Big(\frac{A_2}{A_1}\sin(\phi(R_j,\omega)+\varphi) + \quad \dots \\ \dots \quad \frac{A_1}{A_2}\sin(\phi(R_j,\omega)-\varphi)\Big)\Big] \tag{5.26}$$

This equation describes the time evolution of the frequency of oscillation ω that appears in (4.39). This shift of the frequency was not taken into account in §4 as discussed after equation (4.38). This is a likely explanation of the mismatch discussed in section §4.5.

5.3.2 Limit-cycle solutions

There are only two stable solutions among the fixed points of the system of equations (5.23a),(5.23b) and (5.23c), for a fixed value of ω. These stable solutions are:

$$\begin{cases} A_1 = & A_2 = \frac{2}{\sqrt{3}\omega}\sqrt{\frac{\beta-\alpha\sec(\tau\omega)}{\kappa}} \\ \varphi = & \pm\pi/2 \end{cases} \tag{5.27}$$

We calculate the frequency of oscillation of this limit cycle by substituting (5.27) in (5.24), and obtain the same equation (5.15), which describes the system at its neutrally stable state. We can numerically solve equation (5.27) for ω and obtain ω_L, and then calculate the amplitude of oscillation A_i of the stable solution with (5.27). This solution is a spinning wave, rotating either clockwise or anticlockwise in the θ direction in the annular chamber. The frequency of oscillation at the limit-cycle coincides with the frequency of oscillation ω_L of the system at the border of stability.

5.4 The method of multiple scales

We apply the method of multiple scales as presented in Kevorkian and Cole (1996). We study the system for values of β and τ where the system is linearly unstable, with $\alpha/\omega_0 = 0.08$ fixed. We first consider the system at the onset of the instability, by decreasing β to the reduced linear driving β_L, as defined by equation (5.14). At the onset of instability, the neutrally stable solution oscillates at the frequency ω_L, solution of (5.15). We then apply the method by perturbing such neutrally stable solution. We introduce

$$\varepsilon^2 \equiv \beta - \beta_L \geq 0. \tag{5.28}$$

where we assume that $\varepsilon \ll 1$. We then rewrite the system of equations (5.6) in terms of ε and by susbstituting

$$\eta_j(t) \equiv \varepsilon\xi_j(t), \qquad j = 1, 2 \tag{5.29}$$

we obtain:

$$\begin{aligned}
&\xi_1''(t) + \alpha\xi_1'(t) - \beta_L\xi_1'(t-\tau) + \xi_1(t) + \quad \dots \\
&\qquad \dots \quad \epsilon^2\Big(\frac{3}{4}\xi_1'(t-\tau)^3 + \frac{3}{4}\xi_2'(t-\tau)^2\xi_1'(t-\tau) - \xi_1'(t-\tau)\Big) = 0 \qquad (5.30a)\\
&\xi_2''(t) + \xi_2(t) + \alpha\xi_2'(t) - \beta_L\xi_2'(t-\tau) + \quad \dots \\
&\qquad \dots \quad + \epsilon^2\Big(\frac{3}{4}\xi_2'(t-\tau)^3 + \frac{3}{4}\xi_1'(t-\tau)^2\xi_2'(t-\tau) - \xi_2'(t-\tau)\Big) = 0 \qquad (5.30b)
\end{aligned}$$

The system is linearly unstable for $\varepsilon > 0$, while for $\varepsilon = 0$ we recover the linear differential equation studied in §5.2, but at the onset of instability.

Once the solution $\xi_j(t)$ of (5.30) is found in terms of ε, the solution $\eta_j(t)$ of the original problem (5.6) can be recovered, by substituting ε from (5.28) in (5.29). Since the two equations (5.30) conserve the symmetry with respect to the swap of subscripts 1 and 2, we focus only on (5.30a) in the following.

5.4.1 Timescales, series expansion and time delay approximation

We look for a solution $\xi_j(t)$ with the following dependence on time:

$$\xi_j(t) = \xi_j(T_0(t), T_1(t), T_2(t)) \qquad (5.31a)$$

$$T_k \equiv \varepsilon^k t \qquad k = 0, 1, 2 \qquad (5.31b)$$

where T_j are called slower timescales and are indirectly dependent on the original time variable t through powers of ε. Here we decided to truncate the expansion of the time variable to the second order, so that we consider slower timescales up to T_2. The time derivatives of $\xi_j(t)$ are obtained by applying the chain rule to (5.31a) on the three timescales:

$$\xi_j'(t) = D_0\xi_j\left(T_0, T_1, T_2\right) + \varepsilon D_1\xi_j\left(T_0, T_1, T_2\right) + \varepsilon^2 D_2\xi_j\left(T_0, T_1, T_2\right) + \mathcal{O}(\varepsilon^3) \qquad (5.32a)$$

$$\begin{aligned}
\xi_j''(t) =& D_0^2\xi_j\left(T_0, T_1, T_2\right) + 2\varepsilon D_0 D_1\xi_j\left(T_0, T_1, T_2\right) + \quad \dots \\
\dots \quad & \varepsilon^2\left(D_1^2\xi_j\left(T_0, T_1, T_2\right) + 2D_0 D_2\xi_j\left(T_0, T_1, T_2\right)\right) + \mathcal{O}(\varepsilon^3) \qquad (5.32b)
\end{aligned}$$

where we employed the notation

$$D_n \equiv \frac{\partial}{\partial T_n} \quad , \qquad D_n^m \equiv \frac{\partial^m}{\partial T_n^m}. \qquad (5.33)$$

The time delay appears in all the timescales T_j, and is expanded as a McLaurin series in ε (Das and Chatterjee, 2002) in the expressions (5.31a) and (5.32a):

$$\begin{aligned}\xi_i(t-\tau) =&\xi_i(T_0-\tau, T_1-\varepsilon\tau, T_2-\varepsilon^2\tau)\\ =&\xi_i\left(T_0-\tau,T_1,T_2\right)+\varepsilon\Big(-\tau D_1\xi_i\left(T_0-\tau,T_1,T_2\right)\Big)+\quad\ldots\\ \ldots&\quad\varepsilon^2\Big(-\tau D_2\xi_i\left(T_0-\tau,T_1,T_2\right)+\frac{\tau^2}{2}D_1^2\xi_i\left(T_0-\tau,T_1,T_2\right)\Big)\end{aligned}\tag{5.34a}$$

$$\begin{aligned}\xi_i'(t-\tau) =&D_0\xi_i\left(T_0-\tau,T_1,T_2\right)+\quad\ldots\\ \ldots&\quad\varepsilon\Big(-\tau D_0D_1\xi_i\left(T_0-\tau,T_1,T_2\right)+D_1\xi_i\left(T_0-\tau,T_1,T_2\right)\Big)+\quad\ldots\\ \ldots&\quad\varepsilon^2\Big(-\tau D_0D_2\xi_i\left(T_0-\tau,T_1,T_2\right)+\frac{\tau^2}{2}D_0D_1^2\xi_i\left(T_0-\tau,T_1,T_2\right)-\quad\ldots\\ &\ldots\quad\tau D_1^2\xi_i\left(T_0-\tau,T_1,T_2\right)+D_2\xi_i\left(T_0-\tau,T_1,T_2\right)\Big)\end{aligned}\tag{5.34b}$$

We also look for a solution in terms of a power series in ε, truncated at the second order:

$$\xi_j(t)=\xi_{j,0}\left(T_0,T_1,T_2\right)+\varepsilon\xi_{j,1}\left(T_0,T_1,T_2\right)+\varepsilon^2\xi_{j,2}\left(T_0,T_1,T_2\right)+\mathcal{O}(\varepsilon^3)\tag{5.35}$$

We then substitute (5.35) in (5.32,5.34b), and then substitute (5.35,5.32,5.34b) in equations (5.30), and neglect terms at order higher than two in ε. I report here the results for the first oscillator ξ_1 only, because the second oscillator ξ_2 is symmetric to the first. The LHS of (5.30a) is a polynomial expression in ε, and we look for a solution by setting to zero all its coefficients. This gives rise to a set of delayed differential equations, one at each power of ε.

At order 0 in ε we recover the linearised equations of the problem already studied in §5.2, but at the onset of instability:

$$-\beta_L D_0\xi_{1,0}(t-\tau)+\alpha D_0\xi_{1,0}(t)+D_0^2\xi_{1,0}(t)+\omega_0^2\xi_{1,0}(t)=0\tag{5.36}$$

To ease the notation we define $\mathcal{L}_0[\,.\,]$ as the operator that defines the LHS of equation (5.36), so that (5.36) can be rewritten as

$$\mathcal{L}_0[\xi_{1,0}]=0\tag{5.37}$$

This notation is convenient, because at order one in ε the operator $\mathcal{L}_0$ is retained, but applied to $\xi_{1,1}$:

$$\mathcal{L}_0[\xi_{1,1}] = \beta_L D_1\xi_{1,0}(t-\tau) - \tau\beta_L D_0 D_1\xi_{1,0}(t-\tau) - \alpha D_1\xi_{1,0}(t) - 2D_0D_1\xi_{1,0}(t) \quad (5.38)$$

Notice how the RHS of (5.38) depends on $\xi_{1,0}$ and not on the higher order solutions $\xi_{1,1}$ and $\xi_{1,2}$. Similarly, at order two in ε the linear operator $\mathcal{L}_0$ is applied to $\xi_{1,2}$ and the RHS depends on the lower order terms of the expansion $\xi_{1,0}$ and $\xi_{1,1}$ only:

$$\begin{aligned}\mathcal{L}_0[\xi_{1,2}] = &\frac{1}{2}\tau^2\beta_L D_0 D_1^2\xi_{1,0}(t-\tau) + \beta_L D_1\xi_{1,1}(t-\tau) - \tau\beta_L D_0 D_1\xi_{1,1}(t-\tau)\\ &- \tau\beta_L D_1^2\xi_{1,0}(t-\tau) + \beta_L D_2\xi_{1,0}(t-\tau) - \tau\beta_L D_0 D_2\xi_{1,0}(t-\tau) - \alpha D_1\xi_{1,1}(t)\\ &- \alpha D_2\xi_{1,0}(t) - \frac{3}{4}\kappa\left(D_0\xi_{1,0}(t-\tau)\right)^3 - \frac{3}{4}\kappa\left(D_0\xi_{2,0}(t-\tau)\right)^2 D_0\xi_{1,0}(t-\tau)\\ &+ D_0\xi_{1,0}(t-\tau) - 2D_0D_1\xi_{1,1}(t) - D_1^2\xi_{1,0}(t) - 2D_0D_2\xi_{1,0}(t)\end{aligned} \quad (5.39)$$

5.4.2 Zero order

Following the MMS, we defined β_L in (5.13) and ε^2 in (5.28) so that the solution of the zero order equation (5.36) is neutrally stable. From the linear analysis carried out in §5.2, the only non-decaying solution of equation (5.36) is:

$$\begin{aligned}\xi_{j,0}(T_0,T_1,T_2) &= C_j(T_1,T_2)e^{i\omega_L T_0} + \overline{C}_j(T_1,T_2)e^{-i\omega_L T_0}\\ &= C_j(T_1,T_2)e^{i\omega_L T_0} + \text{c.c.} \qquad j=1,2.\end{aligned} \quad (5.40)$$

where $\overline{C}_j$ is the complex conjugate of C_j, and the angular frequency of oscillation $\omega_L = \omega_L(\alpha,\tau)$ was discussed in §5.2: in particular it is reported in figures 5.3,5.4 as a function of τ only for a fixed value of the damping $\alpha/\omega_0 = 0.08$. Applying the MMS, and writing (5.40), we assume that all the other fast modes of (5.36) decay fast enough to not change the dynamics of the system (Das and Chatterjee, 2002).

5.4.3 First order

We substitute the solution (5.40) in equation (5.38):

$$\begin{aligned}\mathcal{L}_0[\xi_{1,1}] = &-\alpha e^{iT_0\omega_L}D_1C_1 + \beta_L e^{i\omega_L(T_0-\tau)}D_1C_1 - \quad \dots\\ &\dots \quad i\tau\beta_L\omega_L e^{i\omega_L(T_0-\tau)}D_1C_1 - 2i\omega_L e^{iT_0\omega_L}D_1C_1 + c.c.\end{aligned} \quad (5.41)$$

The RHS acts as a forcing f in the equation $\mathcal{L}_0[\xi_{1,1}] = f$, at the frequency ω_L. The unforced solution $\xi_{1,1}$ has as natural frequency the same frequency ω_L. We then apply a solvability condition: to avoid secular growth we set to zero the forcing components at ω_L, by imposing that the coefficient of $e^{i\omega_L T_0}$ at the RHS is zero. This constraint supplies a temporal evolution equation for $D_1 C_1$, which in this case is trivially

$$D_1 C_j = 0 \qquad\qquad j = 1, 2 \tag{5.42}$$

Notice that constraining the coefficient of $e^{-i\omega_L T_0}$ would have led to the conjugate of (5.42). In (5.41) all terms oscillate at frequency ω_L. Then, once we enforce the condition (5.42), the RHS is zero and conversely the particular solution of the differential equation is zero. We also choose to fix the homogeneous solution of the equation to zero[2]. The solution of (5.41) is then

$$\xi_{j,1}(t) = 0 \qquad\qquad j = 1, 2 \tag{5.43}$$

5.4.4 Second order

We proceed in a similar manner, by substituting (5.40),(5.43) and (5.42) in (5.39), obtaining

$$\begin{aligned}
\mathcal{L}_0[\xi_{1,2}] = &-\frac{9}{4} i C_1^2 \kappa \bar{C}_1 \omega_L^3 e^{iT_0\omega_L - i\tau\omega_L} - \frac{3}{4} i C_2^2 \kappa \bar{C}_1 \omega_L^3 e^{iT_0\omega_L - i\tau\omega_L} \\
&- \frac{3}{2} i C_1 C_2 \kappa \bar{C}_2 \omega_L^3 e^{iT_0\omega_L - i\tau\omega_L} - \alpha e^{iT_0\omega_L} D_2 C_1 - i\tau\beta_L \omega_L e^{iT_0\omega_L - i\tau\omega_L} D_2 C_1 \\
&+ \beta_L e^{iT_0\omega_L - i\tau\omega_L} D_2 C_1 - 2i\omega_L e^{iT_0\omega_L} D_2 C_1 + \frac{3}{4} i C_1^3 \kappa \omega_L^3 e^{3iT_0\omega_L - 3i\tau\omega_L} \\
&+ \frac{3}{4} i C_1 C_2^2 \kappa \omega_L^3 e^{3iT_0\omega_L - 3i\tau\omega_L} + i C_1 \omega_L e^{iT_0\omega_L - i\tau\omega_L}
\end{aligned} \tag{5.44}$$

The enforcement of the solvability conditions in (5.44) sets to zero the terms oscillating at ω_L (resonant terms), but other terms oscillating at other frequencies remain (non-resonant terms, oscillating only at $3\omega_L$ in this case). The latter are not responsible of secular growth, and lead to a particular solution $\xi_{i,2}$ oscillating at $3\omega_L$, which is however not discussed here. By imposing the solvability condition on (5.44) and on the equation at the same order for $\xi_{2,2}(t)$, we obtain two equations in terms of $D_2 C_1$ and $D_2 C_2$, the solution of which is:

[2] this is a valid option, though not the only one, as discussed in §2.1 of Nayfeh (2005)

$$D_2 C_1 = \frac{\omega_L \left(9C_1^2 \kappa \bar{C}_1 \omega_L^2 + 3C_2^2 \kappa \bar{C}_1 \omega_L^2 + 6C_1 C_2 \kappa \bar{C}_2 \omega_L^2 - 4C_1\right)}{4\left(i\alpha e^{i\tau\omega_L} - \tau\beta_L\omega_L - i\beta_L - 2\omega_L e^{i\tau\omega_L}\right)} \tag{5.45}$$

and the solution for $D_2 C_2$ is the same of (5.45) if we swap the subscripts.

5.4.5 Amplitudes and phases

We truncate the series solution (5.35) at its first order term, and because $\xi_{j,1}(t)$ is identically zero we obtain

$$\begin{aligned} \xi_i(t) &= \xi_0(T_0, T_1, T_2) + \mathcal{O}(\varepsilon^2) \\ &= C_i(T_1, T_2) e^{i\omega_L T_0} + \text{c.c.} + \mathcal{O}(\varepsilon^2) \end{aligned} \tag{5.46}$$

We can evaluate $dC_j(t)/dt$ with the chain rule on the timescales, and since C_j does not depend on T_0 we obtain

$$\frac{dC_j(t)}{dt} = \varepsilon \frac{dC_j}{dT_1} + \varepsilon^2 \frac{dC_j}{dT_2} \qquad\qquad j = 1, 2 \tag{5.47}$$

where the RHS is described by equations (5.42) and (5.45), and the complex-valued amplitudes C_j describe the slow evolution of the oscillators $\xi_j(t)$. To compare the solution obtained with the method of multiple scales with the solution obtained with the method of averaging, we rewrite (5.46) in terms of real-valued amplitudes $A_j(t)$ and phases $\varphi_j(t)$:

$$\eta_j(t) = \varepsilon \xi_j(t) = A_j(t) \cos(\omega_L T_0 + \varphi_j) \qquad\qquad j = 1, 2 \tag{5.48}$$

From (5.46) and (5.48), we recast the evolution equation (5.47) of the complex amplitudes C_j in terms of real-valued amplitudes and phases, as discussed in detail in

appendix §5.7.1:

$$\frac{dA_1}{dt} = A_1 \frac{L - \kappa N_A(A_1^2, A_2^2, +\varphi)}{D} \tag{5.49a}$$

$$\frac{dA_2}{dt} = A_2 \frac{L - \kappa N_A(A_2^2, A_1^2, -\varphi)}{D} \tag{5.49b}$$

$$\frac{d\varphi}{dt} = \kappa \frac{N_\varphi(A_1^2, A_2^2, -\varphi)}{D} \tag{5.49c}$$

$$\frac{d\varphi_{avg}}{dt} = \frac{N_{\varphi_{avg}}(A_1^2, A_2^2, -\varphi)}{2D} \tag{5.49d}$$

where the expressions of $L, N_A, N_\varphi, N_{\varphi_{avg}}$ and D are reported in appendix §5.7.2. In the first two equations, L/D is a linear growth coefficient and the term N_A/D is responsible for the nonlinear saturation of the amplitudes. The third equation governs the synchronization of the two oscillators, and depends only on nonlinear terms, since it is proportional to κ. The RHS of (5.49d) is the frequency shift of the two oscillators, which depends on the amplitude of oscillation. There are only two stable solutions among the fixed points of the system of equations (5.49a),(5.49b) and (5.49c). These stable solutions are:

$$\begin{cases} A_1 = \quad A_2 = \frac{2}{\sqrt{3}\omega}\sqrt{\frac{\beta - \alpha\sec(\tau\omega_L)}{\kappa}} \\ \varphi = \quad \pm\pi/2 \end{cases} \tag{5.50}$$

The frequency of oscillation of the limit cycle is ω_L, because, once we substitute (5.50), equation (5.49d) evaluates to zero. This means that the method of multiple scales predicts that the frequency of oscillation is ω_L at the onset of the oscillation and at the converged limit-cycle solution.

5.5 Comparison with numerical simulations

We tested the quality of these analytical solutions for a series of numerical simulations using PYDELAY (Flunkert and Schöll, 2009), a code using the Bogacki-Shampine scheme (Bogacki and Shampine, 1989). In particular we fixed $\alpha = 0.08$ and ran simulations of (5.6) on a fine grid with 153 values of β, τ equispaced between 0 and 3 and 337 values of $\tau\omega_0$ equispaced between 0 and 8, for a total of 51561 simulations. We started the numerical integration at $t = 0$, with a history function defined for $t \in [0\,,\, -\tau]$ that is oscillatory. We then extract the amplitude and the frequency of the solutions once the numerical code has converged to a limit-cycle. We report the amplitude in Figure 5.7,

and the frequency in Figure 5.6. The agreement is overall very good for the range of parameters investigated. There is a small discrepancy for small values of β/α, where the contour line of the numerical solution at $A = 0.051$ is slightly jagged and slightly underpredicts the analytical solution in a few regions. This is interpreted with the fact that the we extracted the amplitudes from the numerical solutions too early, before the system had fully converged to the limit-cycle. This is corroborated by the fact that for a constant α, smaller values of β/α make the system more weakly nonlinear, leading to longer time-scales for the evolution of the slow flow quantities, i.e. of the phase, frequency and amplitudes of oscillation.

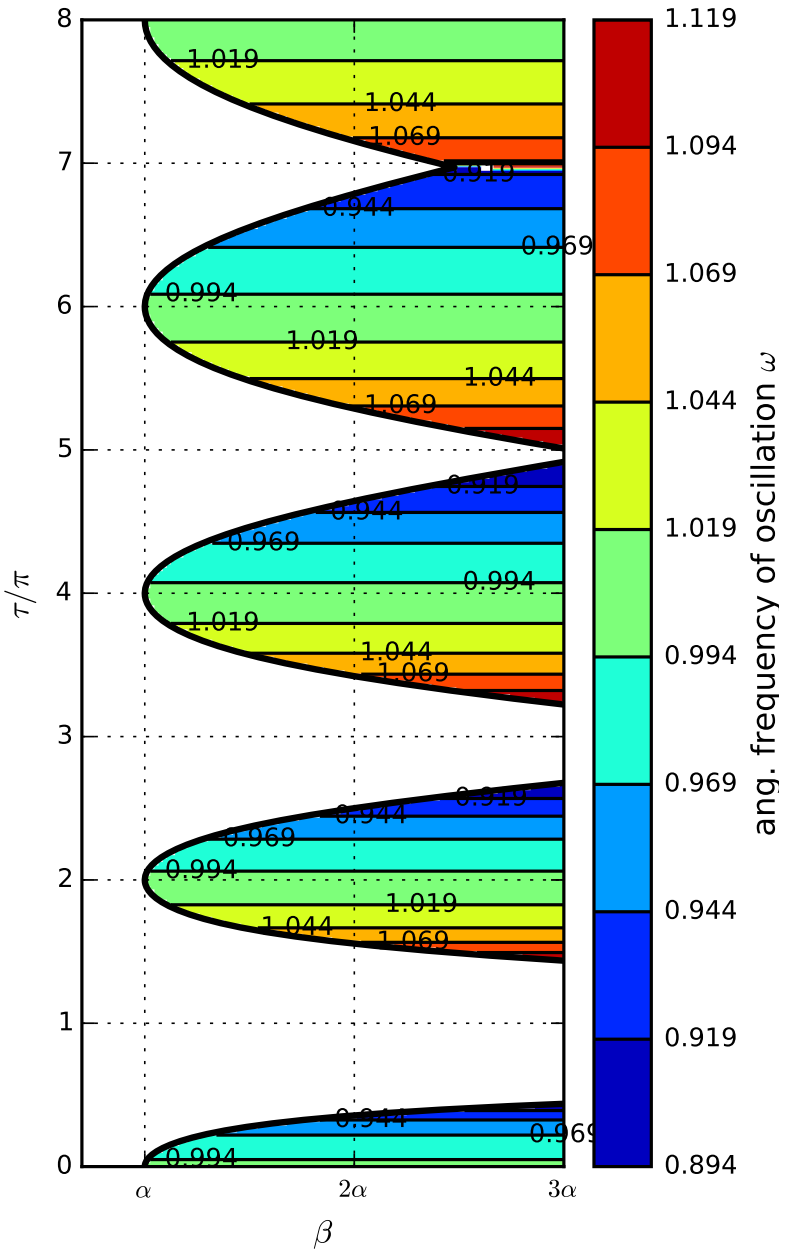

Fig. 5.6 Comparison of the saturated frequency extracted from the numerical integration of the original system of delayed coupled oscillators (contour plot in color) described by equations (5.6) and of the analytical solution (black lines). The border of neutral stability is reported with the thick line, and at its left the system is linearly stable. The black lines were chosen to be at the same levels as the colour contour boundaries. The two coincide almost exactly showing that the analytical solution gives the same results as numerical integration of the original system.

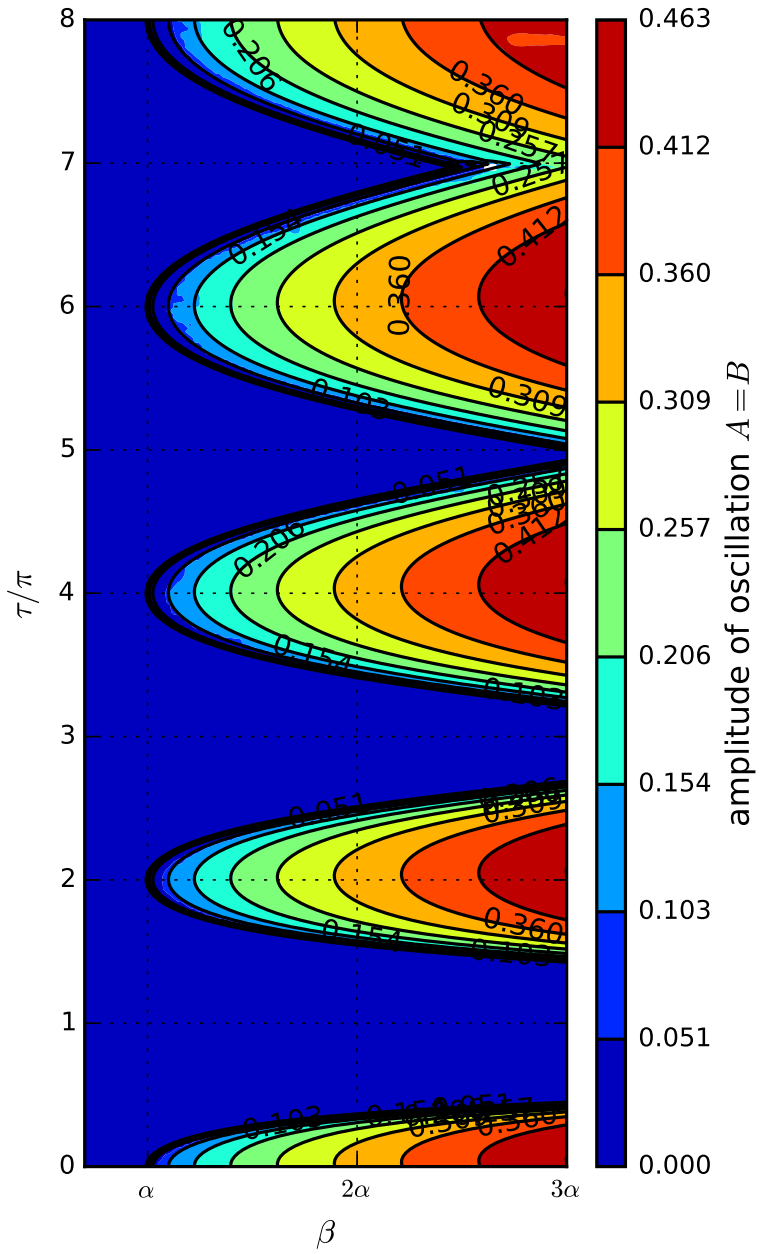

Fig. 5.7 Comparison of the saturated amplitude extracted from the numerical integration of the original system of delayed coupled oscillators (contour plot in color) described by equations (5.6) and of the analytical solution (black lines). The border of neutral stability is reported with the thick line, and at its left the system is linearly stable. The black lines were chosen to be at the same levels as the colour contour boundaries. The two coincide almost exactly showing that the analytical solution gives the same results as numerical integration of the original system.

5.6 Conclusions

In §5.2 we carry out the linear stability analysis of the system and show that a delay that is large when compared to one period of thermoacoustic oscillation linearly destabilizes the thermoacoustic system, making the system more prone to exhibit a thermoacoustic oscillation. This can be seen in Figure 5.5 where the shaded region gets closer to the horizontal asymptote $\beta/\alpha = 1$ as $\tau\omega_0$ increases.

In §5.3 we apply the method of temporal averaging to the system. We recover a dynamic equation for the frequency of oscillation ω of the system, which depends on the instantaneous values of the slowly varying amplitudes and phases of the two modes. We obtain the same equation for the more general case discussed in §4. This equation provides new opportunities for the system identification of thermoacoustic oscillations.

In §5.4 we then apply the method of multiple scales to the system. The dependence on the time delay τ is approximated with a suitable series expansion. This adds to the existing complexity of the method: the number of terms in the many equations is large, and the analytical steps required to obtain the final equations are cumbersome.

The two methods provide different dynamic equations, but the same limit-cycle solutions. We then compare these analytic solutions with the time-integrated equations in §5.5. They have excellent agreement with the nonlinear solution of the problem, suggesting that these two analytical tools are very precise for the low-order modelling of thermoacoustic problems, at least in the range of parameters investigated.

In many occasions the nonlinear flame response is available in terms of a describing function $Q(A, \omega)$. In these cases, as presented in chapter §4 one can apply the method of averaging because in the final equations (4.39) and (5.26) only the describing function Q appears. One cannot on the other hand apply directly the method of multiple-scales, because a state-space realization of the flame-response is needed. One can in principle first calculate a state-space realization of the describing function as discussed in chapter §3, and then apply the method. In the cases where the flame response is available in state space, one is free to choose between the two methods. However, the complexity of the method of multiple scales must be kept into account when making this choice. For the case of the heat release response considered in this chapter the application of the method of averaging took far less time and resources than the method of multiple scales.

This chapter provides a characterization of the effect of the time delay in the linear and nonlinear regime, and a validation of the method of averaging that was used in the other chapters.

5.7 Appendices

5.7.1 Complex to polar transformation

By comparing (5.46) with (5.48), and dropping the subscripts, we find that

$$\varepsilon C = \frac{A}{2} e^{i\varphi} \tag{5.51a}$$

$$\varepsilon \overline{C} = \frac{A}{2} e^{-i\varphi} \tag{5.51b}$$

We derive with respect to time both sides of equations (5.51), and then sum and subtract the two equations, to obtain

$$\frac{dA}{dt} = \varepsilon \frac{dC}{dt} e^{-i\varphi} + \varepsilon \frac{d\overline{C}}{dt} e^{i\varphi} \tag{5.52}$$

$$iA\frac{d\varphi}{dt} = \varepsilon \frac{dC}{dt} e^{-i\varphi} - \varepsilon \frac{d\overline{C}}{dt} e^{i\varphi} \tag{5.53}$$

From which we obtain

$$\frac{dA}{dt} = 2\varepsilon \Re \left[\frac{dC}{dt} e^{-i\varphi} \right] \tag{5.54a}$$

$$\frac{d\varphi}{dt} = \frac{2\varepsilon}{A} \Im \left[\frac{dC}{dt} e^{-i\varphi} \right] \tag{5.54b}$$

By applying the chain rule on $t(T_0, T_1, T_2)$ on both sides of (5.54), and equating terms at the same order in ε, one finds that (5.54) is valid not only for the time t, but also for $T_j\,, \;\; j = 0, 1, 2$.

5.7.2 Slow flow equations

We report here the expressions for the slow flow introduced in equations (5.49):

$$D = 16\Big(\alpha^2 + \Big(4(\alpha\tau+1)\omega_L^2 - \alpha^2\Big)\cos(2\tau\omega_L) + 2(\alpha\tau(\alpha\tau+2)+2)\omega_L^2 + 2\alpha(\alpha\tau+2)\omega_L\sin(2\tau\omega_L)\Big) \tag{5.55a}$$

$$L = -16\omega_L\left(\alpha - \beta\cos(\tau\omega_L)\right)\left(\alpha\sin(2\tau\omega_L) + 2\omega_L\left(\alpha\tau + \cos(2\tau\omega_L) + 1\right)\right) \tag{5.55b}$$

$$N_A(A_1^2, A_2^2, \varphi) = 3\omega_L^3\Big(2\omega_L\Big(A_2^2\cos(2\varphi) + 3A_1^2 + 2A_2^2\Big)\cos(\tau\omega_L)\left(\alpha\tau + \cos(2\tau\omega_L) + 1\right) + \sin(2\tau\omega_L)\left(\cos(\tau\omega_L)\left(\alpha A_2^2\cos(2\varphi) + 3\alpha A_1^2 + 2\alpha A_2^2 - 2A_2^2\omega_L\sin(2\varphi)\right) - \alpha A_2^2\sin(2\varphi)\sin(\tau\omega_L)\right)\Big) \tag{5.55c}$$

$$N_\varphi(A_1^2, A_2^2, \varphi) = 6\omega_L^3\sin(\varphi)\cos(\tau\omega_L)\Big(2\Big(A_1^2 - A_2^2\Big)\sin(\varphi)\sin(\tau\omega_L)\left(\alpha\sin(\tau\omega_L) + 2\omega_L\cos(\tau\omega_L)\right) + \Big(A_1^2 + A_2^2\Big)\cos(\varphi)\left(\alpha\sin(2\tau\omega_L) + 2\omega_L\left(\alpha\tau + \cos(2\tau\omega_L) + 1\right)\right)\Big) \tag{5.55d}$$

$$N_{\varphi_{avg}}(A_1^2, A_2^2, \varphi) = \omega_L\Big(\sin(2\tau\omega_L)\left(\alpha\sin(\tau\omega_L) + 2\omega_L\cos(\tau\omega_L)\right)\Big(15\Big(A_1^2 + A_2^2\Big)\kappa\omega_L^2 - 32\beta + 32\alpha\sec(\tau\omega_L)\Big) + 3\Big(A_1^2 + A_2^2\Big)\kappa\omega_L^2\cos(2\varphi)\sin(2\tau\omega_L)\left(\alpha\sin(\tau\omega_L) + 2\omega_L\cos(\tau\omega_L)\right) - 3\Big(A_1^2 - A_2^2\Big)\kappa\omega_L^2\sin(2\varphi)\cos(\tau\omega_L)\left(\alpha\sin(2\tau\omega_L) + 2\omega_L\left(\alpha\tau + \cos(2\tau\omega_L) + 1\right)\right)\Big) \tag{5.55e}$$

Chapter 6

Conclusions and further work

In chapter §2 we investigate how the transverse forcing of flames can affect the limit-cycle solutions in annular combustors. We find that if in the nonlinear regime the heat release response of the axisymmetric flame sufficiently reduces due to the transverse acoustic velocity, the system converges to a standing wave solution pattern instead of a spinning pattern. The chapter provides a good motivation for further studies on transverse instabilities. In particular, very little information is known on transverse forcing in the nonlinear regime, at large amplitudes of acoustic velocity that can occur at the saturated oscillating state. One other open direction of investigation regards the effect of a non-zero mean swirling flow in the azimuthal direction. If present, this grazing flow bends the flames in the transverse direction, and the modified flame response will respond linearly with respect to the transverse acoustic velocity. This will consequently affect the nonlinear saturation of azimuthal modes.

In chapter §3 we present a tool to map a nonlinear operator from the frequency domain, where it is described in terms of a describing function, to the time domain, where it is a time-invariant nonlinear state space realization. This is useful because often the available flame responses are characterised in the frequency domain, and one may instead need to work in the time domain. This tool paves the way for studies on different prototypal flame responses in low-order models, both in the frequency and the time domain, not restricted to a specific analytic expression for the nonlinear saturation in the time domain as done so far in the literature. This tool can be used in fields beyond thermoacoustics, and is useful whenever one needs to work in the time domain with an operator characterised by a given describing function.

In chapter §4 we present a weakly nonlinear analysis of thermoacoustic oscillations in annular combustion chambers. The novelty of the work consists of considering a discrete number of burners instead of a homogeneous flame response along the annulus,

and of keeping the flame response very generic, as a nonlinear time-invariant operator. This allows us to discuss the conditions on the nonlinear flame response for the existence and stability of standing and spinning waves, and the orientation and amplitudes of these solutions. The chapter provides a new nonlinear theoretical framework that extends previous models that fixed a certain heat release response. Many results of this theory can be measured in experiments. These regard both the qualitative stability results of the two types of solutions, but also the validation of the dynamic equations of the low-order model as an accurate description of the pressure oscillations in the experiments. This work can be extended to account for nonlinear sinks of acoustic damping such as Helmholtz resonators, leading to conditions regarding the nonlinear behaviour of both flames and resonators.

In chapter §5 we carry out the validation of the method of averaging in thermoacoustics, extensively used in chapters §2 and §4. We show that the predictions of the nonlinear solution of two mathematical methods, the method of averaging and the method of multiple scales, are in excellent agreement with the results of the direct numerical integration of the equations. We obtain a dynamic equation for the instantaneous frequency of oscillation, which can be used for the nonlinear system identification of the system. We also present the effect that the time delay between fluctuating heat release rate has on the system, in terms of boundary of stability and of nonlinear amplitudes and frequencies of oscillation.

References

Acharya, V. and Lieuwen, T. (2014). Response of non-axisymmetric premixed, swirl flames to helical disturbances. In *Proceedings of ASME Turbo Expo 2014. Paper no. GT2014-27059*.

Acharya, V., Shreekrishna, Shin, D.-H., and Lieuwen, T. (2012). Swirl effects on harmonically excited, premixed flame kinematics. *Combustion and Flame*, 159(3):1139–1150.

Armitage, C., Balachandran, R., Mastorakos, E., and Cant, R. (2006). Investigation of the nonlinear response of turbulent premixed flames to imposed inlet velocity oscillations. *Combustion and Flame*, 146(3):419–436.

Assier, R. C. and Wu, X. (2014). Linear and weakly nonlinear instability of a premixed curved flame under the influence of its spontaneous acoustic field. *Journal of Fluid Mechanics*, 758:180–220.

Basso, M., Genesio, R., and Tesi, A. (1997). A Frequency Method for Predicting Limit Cycle Bifurcations. *Nonlinear Dynamics*, 13:339–360.

Bauerheim, M., Cazalens, M., and Poinsot, T. (2015). A theoretical study of mean azimuthal flow and asymmetry effects on thermo-acoustic modes in annular combustors. *Proceedings of the Combustion Institute*, 35:3219–3227.

Bauerheim, M., Salas, P., Nicoud, F., and Poinsot, T. (2014). Symmetry breaking of azimuthal thermo-acoustic modes in annular cavities: a theoretical study. *Journal of Fluid Mechanics*, 760:431–465.

Bellucci, V., Flohr, P., Paschereit, C. O., and Magni, F. (2004). On the Use of Helmholtz Resonators for Damping Acoustic Pulsations in Industrial Gas Turbines. *Journal of Engineering for Gas Turbines and Power*, 126(2):271.

Blimbaum, J., Zanchetta, M., Akin, T., Acharya, V., O'Connor, J., Noble, D., and Lieuwen, T. (2012). Transverse to longitudinal acoustic coupling processes in annular combustion chambers. *International Journal of Spray and Combustion Dynamics*, 4(4):275–298.

Bogacki, P. and Shampine, L. (1989). A 3(2) Pair of Runge - Kutta Formulas. *Applied Mathematical Letters*, 2(4):321–325.

Bothien, M. R., Moeck, J. P., Lacarelle, A., and Paschereit, C. O. (2007). Time domain modelling and stability analysis of complex thermoacoustic systems. *Proceedings of the Institution of Mechanical Engineers, Part A: Journal of Power and Energy*, 221(5):657–668.

Bothien, M. R., Noiray, N., and Schuermans, B. (2015). Analysis of azimuthal thermo-acoustic modes in annular gas turbine combustion chambers. *Journal of Engineering for Gas Turbines and Power*, 137(June):061505–1 / 061505–8.

Boudy, F., Durox, D., Schuller, T., and Candel, S. (2013). Analysis of limit cycles sustained by two modes in the flame describing function framework. *Comptes Rendus Mécanique*, 341(1-2):181–190.

Boudy, F., Durox, D., Schuller, T., Jomaas, G., and Candel, S. (2011). Describing Function Analysis of Limit Cycles in a Multiple Flame Combustor. *Journal of Engineering for Gas Turbines and Power*, 133(6):061502.

Bourgouin, J.-F. (2014). *Dynamique de flamme dans les foyers annulaires comportant des injecteurs multiples*. PhD thesis, Ecole Centrale Paris.

Bourgouin, J.-F., Durox, D., Moeck, J. P., Schuller, T., and Candel, S. (2013). Self-sustained instabilities in an annular combustor coupled by azimuthal and longitudinal acoustic modes. *Proceedings of ASME Turbo Expo 2013, paper no. GT2013-95010*.

Bourgouin, J.-F., Durox, D., Moeck, J. P., Schuller, T., and Candel, S. (2014). A new pattern of instability observed in an annular combustor: The slanted mode. *Proceedings of the Combustion Institute*, 35(3):3237–3244.

Brillouin, L. (1953). *Wave propagation in periodic structures: electric filters and crystal lattices*. Chapter VIII, pp. 139-140, Dover publications, 2nd edition.

Campa, G. and Camporeale, S. M. (2014). Prediction of the thermoacoustic combustion instabilities in practical annular combustors. *Journal of Engineering for Gas Turbines and Power*, 136(September 2014):091504.

Campa, G., Cinquepalmi, M., and Camporeale, S. M. (2013). Influence of nonlinear flame models on sustained thermoacoustic oscillations in gas turbine combustion chambers. *Proceedings of ASME Turbo Expo 2013, paper no. GT2013-94495*, pages 1–13.

Candel, S., Durox, D., Schuller, T., Bourgouin, J.-F., and Moeck, J. P. (2013). Dynamics of Swirling Flames. *Annual Review of Fluid Mechanics*, 46(1):130829112240001.

Choi, A. (1997). Real-time fundamental frequency estimation by least-square fitting. *IEEE Transactions on Speech and Audio Processing*, 5(2):201–205.

Ćosić, B., Moeck, J. P., and Paschereit, C. O. (2013). Prediction of pressure amplitudes of self-excited thermoacoustic instabilities for a partially premixed swirl-flame. *Proceedings of ASME Turbo Expo 2013*, pages 1–11.

Ćosić, B., Moeck, J. P., and Paschereit, C. O. (2014). Nonlinear Instability Analysis for Partially Premixed Swirl Flames. *Combustion Science and Technology*, 186(6):713–736.

Ćosić, B., Reichel, T. G., and Paschereit, C. O. (2012). Acoustic Response of a Helmholtz Resonator Exposed to Hot-Gas Penetration and High Amplitude Oscillations. *Journal of Engineering for Gas Turbines and Power*, 134(10).

Crocco, L. (1969). Research on combustion instability in liquid propellant rockets. *Symposium (International) on Combustion*, 12(1):85–99.

Culick, F. E. C. (2006). *Unsteady Motions in Combustion Chambers for Propulsion Systems*. NATO Research and Technology Organization.

Das, S. L. and Chatterjee, A. (2002). Multiple Scales without Center Manifold Reductions for Delay Differential Equations near Hopf Bifurcations. *Nonlinear Dynamics*, 30:323–335.

Dhooge, A., Govaerts, W., and Kuznetsov, Y. A. (2003). MATCONT: A MATLAB package for numerical bifurcation analysis of ODEs. *ACM Transactions on Mathematical Software*, 29(2):141–164.

Dierckx, P. (1993). *Curve and Surface Fitting with Splines*. Oxford University Press.

Dowling, A. P. (1997). Nonlinear self-excited oscillations of a ducted flame. *Journal of Fluid Mechanics*, 346:271–290.

Dowling, A. P. and Stow, S. R. (2003). Acoustic Analysis of Gas Turbine Combustors. *Journal of Propulsion and Power*, 19(5).

Ducruix, S., Schuller, T., and Durox, D. (2003). combustion dynamics and instabilities elementary coupling and driving mechanisms. *Journal of Propulsion . . .*, 19(5).

Durox, D., Bourgouin, J.-F., Moeck, J. P., Philip, M., Schuller, T., and Candel, S. (2013). Nonlinear interactions in combustion instabilities coupled by azimuthal acoustic modes. In *(International summer school and workshop on non-normal and nonlinear effects in aero- and thermoacoustics), June 18-21, 2013, Munich*.

Eskinat, E., Johnson, S. H., and Luyben, W. L. (1991). Use of Hammerstein models in identification of nonlinear systems. *AIChE Journal*, 37(2):255–268.

Evesque, S., Polifke, W., and Pankiewitz, C. (2003). Spinning and Azimuthally Standing Acoustic Modes in Annular Combustors. *9th AIAA/CEAS Aeroacoustics Conference and Exhibit*, pages 1–8.

Flunkert, V. and Schöll, E. (2009). pydelay – a python tool for solving delay differential equations v0.1.1. *ArXiv*.

Gelb, A. and Vander Velde, W. (1968). *Multiple input describing functions and nonlinear system design*. McGraw-Hill Book.

Ghirardo, G., Ćosić, B., Juniper, M. P., and Moeck, J. P. (2015a). State-space realization of a describing function. *Nonlinear Dynamics*.

Ghirardo, G. and Juniper, M. P. (2013). Azimuthal instabilities in annular combustors : standing and spinning modes. *Proceedings of the Royal Society A: Mathematical, Physical and Engineering Sciences*, 469.

Ghirardo, G., Juniper, M. P., and Moeck, J. P. (2015b). Stability criteria for standing and spinning waves in annular combustors. *Proceedings of ASME Turbo Expo 2015, paper no. GT2015-43127*.

Gómez, J. C. and Baeyens, E. (2004). Identification of block-oriented nonlinear systems using orthonormal bases. *Journal of Process Control*, 14(6):685–697.

Guckenheimer, J. and Holmes, P. (1983). *Nonlinear oscillations, dynamical systems, and bifurcations of vector fields*. Springer.

Gustavsen, B. (2006). Improving the Pole Relocating Properties of Vector Fitting. *IEEE Transactions on Power Delivery*, 21(3):1587–1592.

Gustavsen, B. (2008). Fast Passivity Enforcement for Pole-Residue Models by Perturbation of Residue Matrix Eigenvalues. *IEEE transactions on Power Delivery*, 23(4):2278–2285.

Gustavsen, B. and Heitz, C. (2008). Modal Vector Fitting : A Tool For Generating Rational Models of High Accuracy With Arbitrary Terminal Conditions. *IEEE Transactions on advanced packaging*, 31(4):664–672.

Gustavsen, B. and Semlyen, A. (1999). Rational approximation of frequency domain responses by vector fitting. *IEEE transactions on Power Delivery*, 14(3):1052–1061.

Hajimolahoseini, H., Taban, M. R., and Soltanian-Zadeh, H. (2012). Extended Kalman Filter frequency tracker for nonstationary harmonic signals. *Measurement*, 45(1):126–132.

Hauser, M., Lorenz, M., and Sattelmayer, T. (2011). Influence of Transversal Acoustic Excitation of the Burner Approach Flow on the Flame Structure. *Journal of Engineering for Gas Turbines and Power*, 133(4):041501.

Hemchandra, S. (2012). Premixed flame response to equivalence ratio fluctuations: Comparison between reduced order modeling and detailed computations. *Combustion and Flame*, 159(12):3530–3543.

Hurwitz, A. (1964). On the conditions under which an equation has only roots with negative real parts. *Selected Papers on Mathematical Trends in Control Theory*, 65.

Kabiraj, L., Sujith, R. I., and Wahi, P. (2012). Bifurcations of Self-Excited Ducted Laminar Premixed Flames. *Journal of Engineering for Gas Turbines and Power*, 134(3):031502.

Kashinath, K., Waugh, I. C., and Juniper, M. P. (2014). Nonlinear self-excited thermoacoustic oscillations of a ducted premixed flame : bifurcations and routes to chaos. *Journal of Fluid Mechanics*, 761:399–430.

Kevorkian, J. and Cole, J. (1996). *Multiple scale and singular perturbation methods*. Springer.

Klink, W. and Payne, G. (1976). Approximating with Nonorthogonal Basis Functions. *Journal of Computational Physics*, 21:208–226.

Krediet, H. J., Beck, C. H., Krebs, W., Schimek, S., Paschereit, C. O., and Kok, J. B. W. (2012). Identification of the Flame Describing Function of a Premixed Swirl Flame from LES. *Combustion Science and Technology*, 184(7-8):888–900.

Kurokawa, S., Yamanaka, F. N. R., Prado, A. J., and Pissolato, J. (2009). Inclusion of the frequency effect in the lumped parameters transmission line model : State space formulation. *Electric power systems research*, 79:1155–1163.

Landau, L. D. and Lifshitz, E. (1978). *Fluid mechanics, 2nd edition*. Pergamon press.

Lanza, V., Bonnin, M., and Gilli, M. (2007). On the Application of the Describing Function Technique to the Bifurcation Analysis of Nonlinear Systems. *IEEE Transactions on Circuits and Systems II: Express Briefs*, 54(4):343–347.

Lepers, J., Krebs, W., Prade, B., Flohr, P., Pollarolo, G., and Ferrante, A. (2005). Investigation of thermoacoustic stability limits of an annular gas turbine combustor test-Rig with and without Helmholtz-resonators. *Proceedings of ASME Turbo Expo 2005*, pages 177–189.

Lieuwen, T. (2003). Modeling Premixed Combustion-Acoustic Wave Interactions: A Review. *Journal of Propulsion and Power*, 19(5):765–781.

Lieuwen, T. (2012). *Unsteady Combustor Physics*. Cambridge University Press, Cambridge.

Lieuwen, T. and Yang, V. (2005). *Combustion Instabilities In Gas Turbine Engines*. American Institute of Aeronautics and Astronautics, Reston ,VA.

Mensah, G. A. and Moeck, J. P. (2015). Efficient computation of thermoacoustic modes in annular combustion chambers based on Bloch-wave theory. *Proceedings of ASME Turbo Expo 2015, paper no. GT2015-43476*, pages 1–11.

Moeck, J. P., Bothien, M. R., Schimek, S., Lacarelle, A., and Paschereit, C. O. (2008). Subcritical thermoacoustic instabilities in a premixed combustor. In *14th AIAA/CEAS Aeroacoustics Conference, paper no. AIAA-2008-2946*.

Moeck, J. P. and Paschereit, C. O. (2012). Nonlinear interactions of multiple linearly unstable thermoacoustic modes. *International Journal of Spray and Combustion Dynamics*, 4(1).

Moeck, J. P., Paul, M., and Paschereit, C. O. (2010). Thermoacoustic instabilities in an annular Rijke tube. *Proceedings of ASME turbo expo 2010, paper no. GT2010-23577*.

Munjal, M. (1987). *Acoustics of ducts and mufflers*. John Wiley & Sons.

Nassirharand, A. (2009). Matlab software for inversion of describing functions. *Advances in Engineering Software*, 40(8):600–606.

Nayfeh, A. H. (2005). Resolving Controversies in the Application of the Method of Multiple Scales and the Generalized Method of Averaging. *Nonlinear Dynamics*, 40(1):61–102.

Nicoud, F., Benoit, L., Sensiau, C., and Poinsot, T. (2007). Acoustic Modes in Combustors with Complex Impedances and Multidimensional Active Flames. *AIAA Journal*, 45(2):426–441.

Noiray, N., Bothien, M. R., and Schuermans, B. (2011). Investigation of azimuthal staging concepts in annular gas turbines. *Combustion Theory and Modelling*, 15(5):585–606.

Noiray, N., Durox, D., Schuller, T., and Candel, S. (2008). A unified framework for nonlinear combustion instability analysis based on the flame describing function. *Journal of Fluid Mechanics*, 615(2008):139.

Noiray, N. and Schuermans, B. (2013). On the dynamic nature of azimuthal thermoacoustic modes in annular gas turbine combustion chambers. *Proceedings of the Royal Society A: Mathematical, Physical and Engineering Sciences*, 469.

O'Connor, J. and Lieuwen, T. (2012). Further Characterization of the Disturbance Field in a Transversely Excited Swirl-Stabilized Flame. *Journal of Engineering for Gas Turbines and Power*, 134(1):011501.

Palies, P., Durox, D., Schuller, T., and Candel, S. (2011). Nonlinear combustion instability analysis based on the flame describing function applied to turbulent premixed swirling flames. *Combustion and Flame*, 158(10):1980–1991.

Pankiewitz, C. and Sattelmayer, T. (2003). Time Domain Simulation of Combustion Instabilities in Annular Combustors. *Journal of Engineering for Gas Turbines and Power*, 125(3):677–685.

Poinsot, T., Wolf, P., Staffelbach, G., Gicquel, L. Y. M., and Muller, J. D. (2011). Identification of azimuthal modes in annular combustion chambers. *Annual research briefs. Center for Turbulence Research.*, pages 249–258.

Rayleigh, J. W. S. (1878). The explanation of certain acoustical phenomena. *Nature*, 18(455).

Rayleigh, J. W. S. (1894). *The theory of Sound*. MacMillan & Co., 2nd edition.

Saha, A., Bhattacharya, B., and Wahi, P. (2010). A comparative study on the control of friction-driven oscillations by time-delayed feedback. *Nonlinear Dynamics*, 60(1-2):15–37.

Salas, P. (2013). *Aspects numériques et physiques des instabilités thermoacoustiques dans les chambres de combustion annulaires*. PhD thesis, University of Bordeaux I.

Sanders, J. A. and Verhulst, F. (2007). *Averaging Methods in Nonlinear Dynamical Systems*, volume 59 of *Applied Mathematical Sciences*. Springer New York, New York, NY, 2nd edition.

Saurabh, A., Steinert, R., Moeck, J. P., and Paschereit, C. O. (2014). Swirl flame response to traveling acoustic waves. In *Proceedings of ASME Turbo Expo 2014. Paper no. GT2014-26829*.

Schimek, S., Moeck, J. P., and Paschereit, C. O. (2011). An Experimental Investigation of the Nonlinear Response of an Atmospheric Swirl-Stabilized Premixed Flame. *Journal of Engineering for Gas Turbines and Power*, 133(10):101502.

Schuermans, B., Bellucci, V., and Paschereit, C. O. (2003). Thermoacoustic modeling and control of multi burner combustion systems. *Proceedings of ASME Turbo Expo 2003*.

Schuermans, B., Paschereit, C. O., and Monkewitz, P. (2006). Non-Linear Combustion Instabilities in Annular Gas-Turbine Combustors. In *44th AIAA Aerospace Sciences Meeting and Exhibit. Paper no. AIAA-2006-0549*, Reston, Virginia. American Institute of Aeronautics and Astronautics.

Schuermans, B., Polifke, W., and Paschereit, C. O. (1999). Modeling transfer matrices of premixed flames and comparison with experimental results. *ASME, International Gas Turbine and Aeroengine Congress and Exhibition, Indianapolis, IN*.

Schuller, T., Durox, D., and Candel, S. (2003). A unified model for the prediction of laminar flame transfer functions. *Combustion and Flame*, 134(1-2):21–34.

Schuller, T., Tran, N., Noiray, N., Durox, D., Ducruix, S., and Candel, S. (2009). The role of nonlinear acoustic boundary conditions in combustion/acoustic coupled instabilities. In *Proceedings of ASME Turbo Expo 2009, paper no. GT2009-59390*.

Sensiau, C., Nicoud, F., and Poinsot, T. (2009). A tool to study azimuthal standing and spinning modes in annular combustors. *International Journal of Aeroacoustics*, 8(1):57–67.

Seume, J. R., Vortmeyer, N., Krause, W., Hermann, J., Hantschk, C. C., Gleis, S., Vortmeyer, D., and Orthmann, A. (1998). Application of Active Combustion Instability Control to a Heavy Duty Gas Turbine. *Journal of Engineering for Gas Turbines and Power*, 120:721–726.

Stow, S. R. and Dowling, A. P. (2001). Thermoacoustic oscillations in an annular combustor. In *Proceedings of ASME Turbo Expo 2001. Paper no. GT2014-26829*, New Orleans, Louisiana, USA.

Stow, S. R. and Dowling, A. P. (2009). A Time-Domain Network Model for Nonlinear Thermoacoustic Oscillations. *Journal of Engineering for Gas Turbines and Power*, 131(3):031502.

Tay-Wo-Chong, L., Bomberg, S., Ulhaq, A., Komarek, T., and Polifke, W. (2012). Comparative Validation Study on Identification of Premixed Flame Transfer Function. *Journal of Engineering for Gas Turbines and Power*, 134(2):021502.

Taylor, J. H. (1983). A systematic nonlinear controller design approach based on quasilinear system models. In *American Control Conference*.

Wahi, P. and Chatterjee, A. (2004). Averaging Oscillations with Small Fractional Damping and delayed terms. *Nonlinear dynamics*, 38:3–22.

Wolf, P., Staffelbach, G., Balakrishnan, R., Roux, A., and Poinsot, T. (2010). Azimuthal instabilities in annular combustion chambers. In *Center for Turbulence research, Proceedings of the Summer program*, pages 259–269.

Wolf, P., Staffelbach, G., Gicquel, L. Y., Müller, J.-D., and Poinsot, T. (2012). Acoustic and Large Eddy Simulation studies of azimuthal modes in annular combustion chambers. *Combustion and Flame*, 159(11):3398–3413.

Worth, N. A. and Dawson, J. R. (2013a). Modal dynamics of self-excited azimuthal instabilities in an annular combustion chamber. *Combustion and Flame*, 160:2476–2489.

Worth, N. A. and Dawson, J. R. (2013b). Self-excited circumferential instabilities in a model annular gas turbine combustor: Global flame dynamics. *Proceedings of the Combustion Institute*, 34:3127–3134.

Zinn, B. (1970). A theoretical study of non-linear damping by helmholtz resonators. *Journal of Sound and Vibration*, 13(3):347–356.